This is to certify that the

dissertation entitled

MORPHOLOGIES OF

METAL SURFACES, FILMS AND CLUSTERS

presented by

Xinhua Yu

has been accepted towards fulfillment
of the requirements for

Ph.D. degree in Physics

Major professor

Date 11/10/94

MORPHOLOGIES OF METAL SURFACES, FILMS AND CLUSTERS

BY

Xinhua Yu

A DISSERTATION

Submitted to
Michigan State University
in partial fulfillment of the requirements
for the degree of

DOCTOR OF PHILOSOPHY

DEPARTMENT OF PHYSICS AND ASTRONOMY

1994

ABSTRACT

MORPHOLOGIES OF METAL FILMS, SURFACES AND CLUSTERS

by

Xinhua Yu

The topics concerning the healing process of metal surfaces; morphological changes of metal films on insulator substrates; and small metal clusters, have been investigated using computer simulation techniques.

Surface diffusion is usually the dominant dynamic process by which a solid surface reaches equilibrium, particularly for metals at temperatures below melting. Above the roughening temperature, the surface profile and surface tension are continuous functions of surface geometry. At equilibrium, the chemical potential which is related to the surface curvature, must be equal everywhere on the surface. Below the roughening temperature, the surface tension has cusp points that have to be propertly treated in order to derive the dynamic equations. Two different approaches are utilized and the corresponding dynamic equations result in the formation of facets on an initially sinusoidal surface profile.

During the formation of thin metal films on an insulator substrate, a sequence of morphologies occur as deposition continues. An interrupted coalescence model(ICM) provides a good explanation of the high percolation coverage observed in experiments. The interruption of coalescence is explained as the combined consequence of inhomogeneous substrate pinning and thermal fluctuations.

Gold clusters of size N>10, undergo a fairly sharp solid-liquid phase transition. The transition temperature decreases as the cluster size decreases. When N is sufficiently large(>200), the surface atoms have diffusive behavior in the solid phase. We use the radius of gyration as a shape parameter to study the shape change of clusters. The radius of gyration behaves distinctly in various size and temperature regions.

DEDICATION

For those long working days and even longer weekends while working on the dissertation, with love, I dedicate this work to Zhixia and Albert.

ACKNOWLEDGMENTS

First of all, I would like to express my gratitude to my advisor, Professor Philip M. Duxbury whose insightful guidance and broad knowledge in condensed matter physics help this work move forward smoothly. Without his steady support and encouragement, this work would never have been initiated. I am also benefited from numerous valuable lectures and seminars given by Professors M.Thorpe, S.D.Mahanti, David Tomanek, and T.Kaplan. I sincerely thank Professors M.A.Dubson, B.Sherrill, D.Stump who serve on my committee.

Here are a few of many families and friends I like to thank: My parents whose love and support inspire me to do more things; My host family, Wally and Marilyn Baird who generously accept me as part of their family; Caihua Gao, my mother-in-law who came from China to help baby-sit Albert; Tie Lan and Ying Liang, Jiahwa Yeh, Yiliang Liu and Vincent Ma with whom my family did many memorable wonderful activities together; Qing Yang and Fei Deng whose friendship also enriches my life at MSU.

The financial supports of the Department of Energy and the Center for Fundamental Material Research are gratefully acknowledged.

Tables of Content page

LIST OF TABLES.....page

LIST OF FIGURES.....page

CHAPTER ONE

INTRODUCTION

1.1 Complexity of Surfaces:

During the past decade, surface research has clearly shifted its interest from the macroscopic to the microscopic scale, mainly thanks to the innovation and widening applications of electron microscopes; a wealth of novel experimental techniques and theoretical methods have been applied and developed successfully. Many subjects such as catalysis; microelectronic devices and contacts; lubrication; resistance to erosion; creep and intragranular fracture etc.; are brought alive again after years of inefficiency and frustrations. To understand those complex problems, one must address several fundamental problems: atomic and electronic structure; diffusion along surfaces or across interfaces; the energy and chemistry of surface regions and the response to external forces. Existing techniques for investigating surfaces have reached maturity and are increasingly being applied to systems of practical relevance. On the experimental side, a variety of microscopes are providing structural and electronic information about surfaces at a number of complementary length scales. On the theoretical side, phenomenological

theories for total energy calculations have had much success in solving very complex structural problems on the atomic scale. More sophisticated theories have been introduced to direct calculations of motions of surface particles by comparison with experimental data.

To gain comprehension of surface phenomena, it is critical to understand the complexity aroused from the termination of a crystal by a surface. The manifestation of the complexity can be studied from two different aspects: One is to study the atomic arrangement in the surface region. Two particularly interesting effects may take place due to the presence of a surface. (1)the distance between the surface plane and those parallel to the surface deviate from their bulk values; (2) some lateral structural change may also occur to the atoms on certain surfaces(for instance, Au:110 surface) and this phenomena is called surface reconstruction which has caught much attention lately. Another aspect is dynamic properties, for instance, vibrations and diffusions, which are of considerable importance to the elucidation of surface phenomena and rich experimental results. The dynamic problems of surfaces are usually very complicated and not analytically solvable because of nonlinearity in dynamic equations and thus a certain approximation like the harmonic approximation is usually made. The surface atoms are less bonded than their

bulk counterparts and therefore their mean square amplitudes are significantly greater than in the bulk. Even at very low temperature the surfaces appear to be disordered while atoms in the bulk are very much in order. Often, one needs to study the migration of particles on a surface; for example in wetting phenomena, surface flattening and roughening and thin film formation. Other approaches have to be used to tackle these difficult problems. Because many of those problems are associated with phase transitions and critical phenomena, scaling and renormalization are powerful tools in the investigation. Computer simulation is adding a new dimension to scientific investigation, establishing a role of equal importance with the traditional approaches of theory and experiment. As the speed and accuracy of arithmetic computers improve tremendously, it is feasible and advantageous to carry out quantitative investigation through detailed computer simulation. It is thus no surprise that many portions of this work are numerical analyses or computer simulations.

In the next section, I will give a brief introduction to the contents of each chapter of the thesis and some key concepts are outlined.

1.2 Overviews:

The first part of the thesis studies the morphology of thin metal films, surfaces and clusters. The equilibrium geometry of a finite crystal is determined by many factors among which the crystal structure, temperature and crystal size are considered the most important. At any temperature, the shape of a finite crystal can be found theoretically by the Wulff construction(Wulff, 1901) provided that the surface tension γ as a function of crystalline orientation θ is known. At finite temperature, the total free energy of the system reaches a minimum at its equilibrium shape. If the temperature is sufficiently low, it is expected that the geometry does not change much from its ground state except at those positions like corners and edges where atoms are easily activated. As temperature increases, the surface atoms start to diffuse prior to the bulk ones because of their reduced binding. One fundamental question is how those diffusing surface atoms alter the non-equilibrium shape of crystals. This question is to be discussed in chapter two. One approach is to view the surface to be a continuous function $f(x,y,z)=0$. The diffusion of surface particles is caused by the gradient of chemical potential μ which is proportional to the curvature K of the surface if the surface tension γ is isotropic. As a result, a differential equation describing the process can be derived. The surface diffusion equation has many successful applications in

studying systems at temperature $T \approx 0.75T_m$, the bulk melting temperature. Nevertheless, as a matter of fact, γ is strongly dependent on surface orientation at low temperatures and particularly has a cusp singularity along crystalline planes of high symmetry: $\gamma(\theta) = \gamma_0 + \gamma_1|\theta|$. To overcome this difficulty, two methods are introduced and alternative equations are derived. One method originally developed by Bonzel etc.(Bonzel, 1984,1986) is to de-singularize the cusp point by replacing the small angle θ with $\sqrt{\theta^2 + \theta_0^2} - \theta_0$ where θ_0 is a small constant. As a result, the second derivative of γ exists. The other method assumes that the surface profile has a miscut angle with the high symmetry lattice plane. The alteration of surface shape is due to the motion of steps. Lancon and Villain(Lancon and Villain, 1990) studied the chemical potential of steps and obtained a different version of surface dynamics. Because of the nonlinearity of the equations governing those dynamic processes, their solutions are attained via finite difference methods.

The work on the formation of thin metal films(Chapter Three) on an insulating substrate was motivated by the experiments by Dubson and Jeffers(Dubson etc. 1994). When metal vapor condenses on a clean non-wetting insulating substrate to form a thin film, a sequence of morphological changes occurs as the thickness of the film increases, going

from isolated compact islands, then a "wormy" structure, to a percolating structure and finally a continuous thin film. It is observed that an abnormally high percolating coverage often occurs. Based upon the complete coalescence model by Meakin and Family(MFM) (Family and Meakin, 1988,1989), we proposed the interrupted coalescence model(Yu etc.,1991), in which two droplets on the substrate do not coalesce as long as the sizes of both touched droplets reach a critical dimension R_c. R_c depends on deposition rate, substrate temperature, as well as the substrate structure. Because of the presence of R_c, this "interrupted coalescence" model goes through stages of early complete coalescence, crossover to wormy structure, percolation and hole filling as in experiments. Our computer simulation mimicking the experiment showed that the coverage at the percolation point increases with increasing R_c. We also calculated the cluster size distribution and the critical indices near percolation and found that this model is in the same universality class as the conventional percolation model(Satuffer,1985). Furthermore, it is shown that the inhomogeneity of the substrate may be the mechanism leading to the interruption of coalescence. This is illustrated by a calculation of the total energy of two droplets with a grain boundary in their interior.

In Chapter Four, I deal with smaller physical systems, metal clusters, using the molecular dynamics simulation method that is becoming an increasingly powerful tool in scientific investigation. The simple idea of molecular dynamics is that the detailed information such as position, velocity etc. of each atom in a system is calculated as a function of time assuming that each atom complies with Newtonian dynamics. From this information, thermal dynamics quantities can be calculated straightforwardly. In a metal, many experiments reveal that atoms have many-body interactions, therefore it is critical to have a good potential to describe the metal. We have chosen an embedded-atom potential(Gupta, 1981) which gives good predictions for many bulk properties of transition and noble metals. Because of the outstanding surface properties of gold and the availability of experimental data, we selected gold clusters for study. The calculations of temperature and total energy show that the liquid-solid phase transition is clearly identified in clusters with size greater than about 10 atoms. The melting temperature T_m decreases as system size decreases and obeys the following semi-empirical relationship(Buffat,1976;Borel,1981):

$$T_m(R) = T_m(\infty)(1 - \frac{R_c}{R}) \qquad (1.1)$$

where R_c is constant and determined by the bulk properties of gold. By calculating the mean square deviation of both surface and bulk atoms, we found that the surface atoms have diffusive behavior at temperature below melting for large clusters(N>200) in comparison with the absence of surface diffusion for small size clusters(N<150). The dynamics is studied by looking into the shape of non-equilibrium gold clusters and the radius of gyration r_g represents the shape parameter. We observe how r_g decays from its initial value. Above the melting temperature, the correlation between atoms is weak and r_g decays roughly exponentially with large fluctuations. Below T_m, the decay of r_g depends on the cluster size N. When N is small (less than 150), r_g reaches a meta-stable value quickly with typical time t_e and remains almost unchanged for a long time t_c and suddenly decreases to a smaller value within a very short time t_q. The three time scales have the following relations: $t_e \approx t_q << t_c$. When N is large (greater than 250), and the temperature is close to T_m, r_g decays like smaller clusters. But when T is considerably away from the T_m, r_g decays algebraically because of the dominance of surface diffusion in large clusters.

Chapter Five of the thesis describes work on quantum transport of two-dimensional percolating lattices. Electrons are permitted to hop between two bonded sites on a

percolating two dimensional lattice. Therefore the Hamiltonian describing the system is simply written as:(Anderson,P.W., 1958)

$$H = \sum_{i,j} t_{ij}(a_i a_j^{+} + a_i^{+} a_j) + \sum_i \varepsilon_i a_i^{+} a_i \qquad (1.2)$$

where i,j are nearest neighbor lattice sites and $t_{ij} = 1$ for a present bond and zero for an absent one and ε_i is the site energy. From percolation theory, when the bond probability p is less than a critical value p_c(for a 2d square lattice p_c=0.5) there exists no infinitely large clusters. For a system of large but finite dimension, the largest cluster size has a size of the same order as the system. If all present bonds are good conductors and a voltage is applied to two sides of the system, a current will flow when $p>p_c$, and no current flows for $p<p_c$. Because of quantum effects, an electron is more likely to scatter backward and more transmitting bonds are required for an electron to transmit across the sample. In other word, the quantum threshold p_Q below which no current flows through the system ought to be larger than p_c. To find p_Q and investigate the scaling of conductance, we employed two methods in the calculation of conductance: i) the linear response theory and ii) transfer matrix and Landauer formula. In the linear response theory, we introduce the Green's function $G^{\pm}=(E-H\pm i\eta)^{-1}$ where E is the Fermi energy and η is a small positive number. The

conductance can be expressed as the product of two Green's functions which are expressed in matrix form and are easily calculated. The conductance G_c is related to electron scattering by disorder via Landauer's formula: $G_c=(e^2/h)tr(tt^+)$ where t is the transfer matrix of the disordered region. Our calculations show that p_Q is one for 2d percolation lattices. This result supports the prediction of weak localization that any finite disorder will cause localization of the electron wavefunction in two dimensional systems.

Finally I summarize the work in the thesis and discuss several interesting future projects stimulated by the analyses described here.

CHAPTER TWO

THE ALTERATION OF A SURFACE PROFILE DUE TO SURFACE DIFFUSION

2.1 Introduction

An isolated system, say a heated metal crystal, tends to alter its shape in order to minimize its total surface free energy. The common processes by which the shape change is realized are evaporation-condensation, volume diffusion, and surface diffusion. The process of evaporation-condensation (Mullins, 1957, 1959) occurs when the chemical potential of the system μ differs from that of its co-existing vapor μ_0. Evaporation- condensation does not conserve the total number of atoms in the system which gains atoms when its chemical potential is lower and loses atoms when its chemical potential is higher than the vapor's. At finite temperature, there exist bulk vacancies and defects which allow the bulk atoms to move, in which case volume diffusion is important. The ratio of vacancy number to total atoms is approximated to be $\exp(-E_b/kT)$ where E_b denotes the approximate energy needed to create a vacancy. For most metals, E_b is of order several electron volts, i.e. 10^4-$10^5 K$ and thus the ratio is extremely small at room temperature. Surface diffusion involves surface particles which move along the surface of the material. Due to the reduced bonding at the surfaces,

diffusion processes are much more probable at surfaces than in the bulk. For a small metal particle with size 0.1 to 10 μm at temperature of about $0.75T_m$ (T_m is the bulk melting temperature) the surface diffusion is considered to be a dominant factor governing the morphological evolution.

The equilibrium properties of a surface can be described by a few thermodynamic quantities like surface tension γ defined as the surface free energy per unit area. Generally γ is anisotropic and depends on the orientation of the surface. The lowest energy profile of a surface is then non-trivial and the total surface free energy of a finite system

$$F_s = \oiint_A \gamma \cdot dA \qquad (2.1)$$

has to be minimized under the constraint that the volume is constant. The equilibrium shape of a crystal of fixed volume can be determined from the Wulff construction (Wulff,1901; Herring,1951) which utilizes the result that the surface tension γ of any face is proportional to the distance of that face from the center of the equilibrium shape. Therefore, the process is described as follows: give a polar plot of surface tension $\gamma(\theta)$; draw a ray from the center at any direction θ and the line intersects with the $\gamma(\theta)$ surface at a point; construct a plane perpendicular to the ray(Wulff plane); the crystal shape is the envelope of all those planes. One particularly

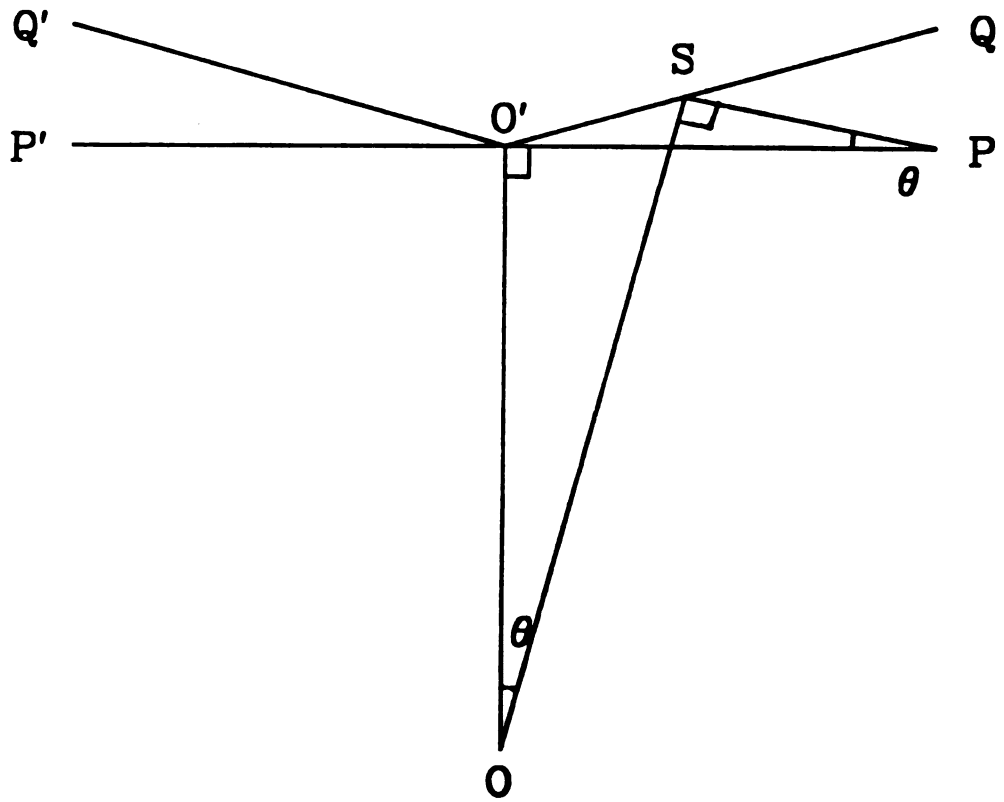

Figure 2.1: The presence of a cusp point in $\gamma(\theta)$ will lead to the facets on the equilibrium shape through Wulff construction whose procedure was briefly described in the text. The polar plot near $\theta = 0$ is for the function $\gamma(\theta)=\gamma_0+\gamma_1|\theta|$.

interesting consequence of the Wulff construction is that if $\gamma(\theta)$ has cusp point, a finite flat area (facet) will be produced in that direction. Figure 2.1 shows why this is the case. From this figure, it can been seen that the envelope formed by plane SP is the plane P'P as we move S along O'Q. The surface atoms are highly correlated at very low temperature. As the temperature increases, a two dimensional surface undergoes a roughening phase transition(Week,1980). Let $h(x,y)$ denote the height of a surface with respect to a proper reference plane (e.g. the perfect surface at T=0), where (x,y) labels the position on the plane. The roughness of a surface is defined as the spatial correlation function:

$$(\Delta h)^2 = \left\langle h^2(r) - \langle h \rangle^2 \right\rangle \qquad (2.2)$$

Where <> stands for thermal average. Without loosing generality, it is assumed that above the roughening temperature T_R, the leading terms in a Hamiltonian describing the surface are(Fisher,M.E., 1988)

$$H = 1/2 \int dxdy \left[J(\nabla h)^2 + gh^2 \right] \qquad (2.3)$$

when both ∇h and h are small. Here J and g are constants relating to surface tension and external force respectively. Then $(\Delta h)^2$ is calculated according to a Boltzmann distribution, giving $(\Delta h)^2 \propto \ln L$, where L is the surface dimension. Below T_R, the Hamiltonian ought to include terms which favor h being integers. Using either solid-on-solid(S.O.S) or the sine-Gordon model, it is theoretically

proved that the roughness of a surface is only a function of temperature and independent of system size at low temperatures. The surface free energy at $T=T_R$ has a cusp singularity point along directions of high symmetry.

The experimental methods(Schommers etc.,1987) used in studying surface diffusion are roughly divided into three groups: a) direct observation of diffusing atoms using field ion microscopy (FIM) which records the motion of individual atoms or clusters on a small metal surface area and electron microscopy which observes the migration of surface atoms and simultaneously the detailed surface structure. The diffusion constant D can be directly obtained from FIM data using $\langle r^2(t) = 4Dt \rangle$ and the temperature dependence of D gives the magnitude of barriers over which the diffusion process is thermally activated, i.e.

$$D = D_0 \exp(-E_s / kT) \qquad (2.4)$$

where E_s is a surface activation energy. b) Concentration gradient methods such as scanning AES(Auger electron spectroscopy) analysis that studies hetero-diffusion and laser light diffraction which attains information on self-diffusion on metal surfaces. The laser light diffraction experiments measure the amplitude of a surface profile at constant temperature as a function of annealing time by recording the intensity distribution of laser-light diffraction generated by the periodic profile. c)

Equilibrium methods which include the field emission fluctuation method, neutron scattering and He-atom scattering, chiefly studying the diffusion of adsorbates. These experiments employ inelastic scattering to measure space and the time dependent self-correlation function $C(r,t)$ or its Fourier transform $S(q,\omega)$.

Theoretical study of surface diffusion relies on the continuum model which assumes a system surface is described as a continuous function $z(r,t)$. The model proposed that the surface particles diffuse because the chemical potential μ varies along the surface. The mechanism is very similar to the concept of electric charges moving along a conducting surface when a conductor is not in equilibrium (equi-potential condition). It will be seen that the continuum model describes self-diffusion above T_R quite successfully, but has serious problems when the temperature is below T_R. More detailed study is possible with either molecular dynamics(MD) or Monte Carlo(MC) simulation techniques, which requires a suitable atom-atom interaction.

In this chapter, I will introduce previous work on surface diffusion relating to our later discussions and present some numerical calculation results. In the following section, a diffusion-like equation describing the dynamics of surface profile will be derived using a continuum model and some simple applications will be presented. In section

2.3 I will discuss surface diffusion below the roughening temperature T_R. We discuss the anisotropic model first and then the miscut model. The conclusions are summarized also in this section.

2.2 Surface Diffusion Equation:

Let us start with the expression for the free energy of a bulk-surface system with surface profile z(x,y). The expression is written in the form:

$$F = \mu_0 \iint dxdyz(x,y) + \iint dxdy\,\sigma(z'_x, z'_y) \qquad (2.5)$$

Here the first term is the bulk free energy and the second one is the surface free energy and σ relates to surface tension through

$$\sigma = \gamma(z'_x, z'_y)\sqrt{1 + z'^2_x + z'^2_y} \qquad (2.6)$$

The chemical potential is obtained from $\mu = \Omega\delta F / \delta z$, yielding:

$$\mu - \mu_0 = -\frac{\partial}{\partial x}\left(\frac{\partial \sigma}{\partial z_x'}\right) - \frac{\partial}{\partial y}\left(\frac{\partial \sigma}{\partial z_y'}\right) \qquad (2.7)$$

If γ is constant, one has

$$\mu - \mu_0 = -\Omega\gamma\left(\frac{\partial}{\partial x}\frac{z'_x}{\sqrt{1 + z'^2_x + z'^2_y}} + \frac{\partial}{\partial y}\frac{z'_y}{\sqrt{1 + z'^2_x + z'^2_y}}\right) \qquad (2.8)$$

It has been shown that the term in the parentheses on the right hand side is exactly equal to $-(K_1+K_2)=-K$, here K_1 and K_2 are the two principal curvatures of the surface. Therefore we have the Gibbs-Thompson relationship:

$$\mu - \mu_0 = \Omega\gamma K \tag{2.9}$$

For better illustration, we consider one-dimensional isotropic surfaces of height z(x,t) and derive the dynamic equation first, then extend to anisotropic and higher dimensional systems. Suppose z(x,t) coexists with its vapor of chemical potential μ_0 and that the bulk chemical potential is also μ_0 to suppress the evaporation-condensation process and surface diffusion is the dominant dynamic process to alter the surface profile. From equation (2.9), if the curvature varies on the surface, the surface particles undergo a "field", the gradient of chemical potential which drives them to drift. The drift velocity ought to be proportional to the magnitude of the field, reading

$$v_s = -M_s \nabla_s \mu = -\frac{D_s \gamma \Omega}{k_B T} \frac{\partial K}{\partial s} \tag{2.10}$$

Here the Einstein relation $M_s = D_s / k_B T$ has been used and M_s and D_s denote the mobility and surface diffusion constant respectively. The corresponding surface current is the product of drift velocity and area density ν, reading:

$$J = -\frac{D_s \gamma \Omega \nu}{k_B T} \frac{\partial K}{\partial s} \tag{2.11}$$

Applying the continuity equation to the surface,

$$\frac{\partial J}{\partial s} + \frac{\partial \rho}{\partial t} = 0 \tag{2.12}$$

where ρ denotes the particle number variation per unit surface area, one easily obtains the distance change along its normal by multiplying atomic volume Ω

$$\dot{n} = \frac{\partial n}{\partial t} = \frac{D_s \gamma \Omega^2 \nu}{k_B T} \frac{\partial^2 \mathrm{K}}{\partial s^2} \tag{2.13}$$

It is easily generalized to higher dimensions by replacing $\partial^2 \mathrm{K} / \partial s^2$ with $\nabla_s^2 \mathrm{K}$, which gives

$$\frac{\partial n}{\partial t} = B \nabla_s^2 \mathrm{K} \tag{2.14}$$

where $B = D_s \gamma \Omega^2 \nu / k_B T$ and K is sum of two principal curvatures at a surface point. When γ is not isotropic and dependent on surface orientation θ, the modified Gibbs-Thompson relation (Herring,1952)is:

$$\mu - \mu_0 = \Omega \left(\gamma + \frac{\partial^2 \gamma}{\partial \theta_1^2} \right) \mathrm{K}_1 + \Omega \left(\gamma + \frac{\partial^2 \gamma}{\partial \theta_2^2} \right) \mathrm{K}_2 \tag{2.15}$$

on the condition that the second derivative of γ exists. Here θ_1 and θ_2 are angles between the normal at a surface point and two principal planes. Correspondingly the surface diffusion equation becomes:

$$\frac{\partial n}{\partial t} = \frac{B}{\gamma} \nabla_s^2 \left[\left(\gamma + \frac{\partial^2 \gamma}{\partial \theta_1^2} \right) \mathrm{K}_1 + \left(\gamma + \frac{\partial^2 \gamma}{\partial \theta_2^2} \right) \mathrm{K}_2 \right] \tag{2.16}$$

The equilibrium shape when γ is isotropic is trivial as seen by setting $\dot{n}$ to zero, and it is simple to show that the equilibrium shape is a circle in two dimensions and a sphere in three dimensions for a closed surface. Now we add a perturbative term to a two dimensional equilibrium surface and calculate how the shape relaxes under the perturbation.

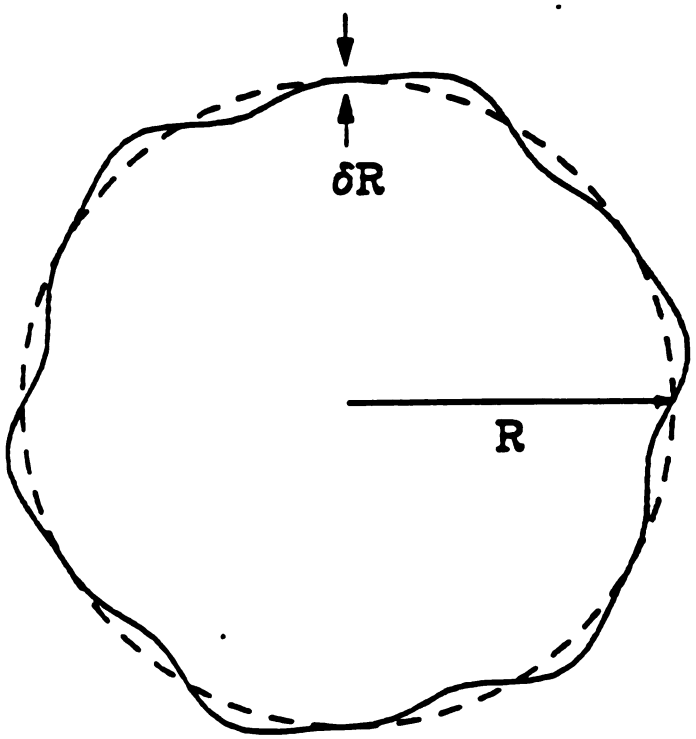

Figure 2.2: A perturbed spherical surface. The perturbation magnitude is much smaller than the radius of the sphere so that one can treat the problem as small perturbation.

Adding a small circumferential perturbation $R_0\Delta(\theta,\varphi)$ to the equilibrium shape $r=R_0$ with $\Delta(\theta,\varphi)<<1$(see Figure 2.2). The surface Laplacian is written in terms of spherical coordinates (r,θ,φ) to be(Brailsford and Gjostein, 1975):

$$\nabla_s^2 = \frac{1}{R_0}\sin\theta\left(\frac{\partial}{\partial\theta}\sin\theta\frac{\partial}{\partial\theta}+\frac{1}{\sin^2\theta}\frac{\partial^2}{\partial\varphi^2}\right) \qquad (2.17)$$

$\Delta(\theta,\varphi)$ can be expanded:

$$\Delta = \sum_{l,m}\Delta_{lm}Y_{lm}(\theta,\varphi) \qquad (2.18)$$

where Y_{lm} is the standard spherical harmonic function. To the first order of Δ, the curvature is also written as:

$$K = K_0 + \frac{1}{R_0}\sum_{l,m}(l+2)(l-1)\Delta_{lm}Y_{lm} \qquad (2.19)$$

It is immediate to obtain the differential equation for each Δ_{lm} component

$$\dot{\Delta}_{lm} = -\frac{B}{R_0^4}l(l+2)(l^2-1)\Delta_{lm} \qquad (2.20)$$

whose solution is

$$\Delta_{lm}(t) = \Delta_{lm}(0)\exp(-t/\tau_{lm}) \qquad (2.21)$$

where $\frac{1}{\tau_{lm}} = \frac{B}{R_0^4}l(l+2)(l^2-1)$. We have assumed that at equilibrium $\Delta_{lm}(\infty)=0$. The result shows that the relaxation time τ_{lm} for mode {l,m} in proportional with R_0^4. When l>0, $\tau_{lm} \sim (R_0/l)^4$, which is approximately the fourth power of the wavelength. Therefore, short wave perturbations decay much faster than long wave ones.

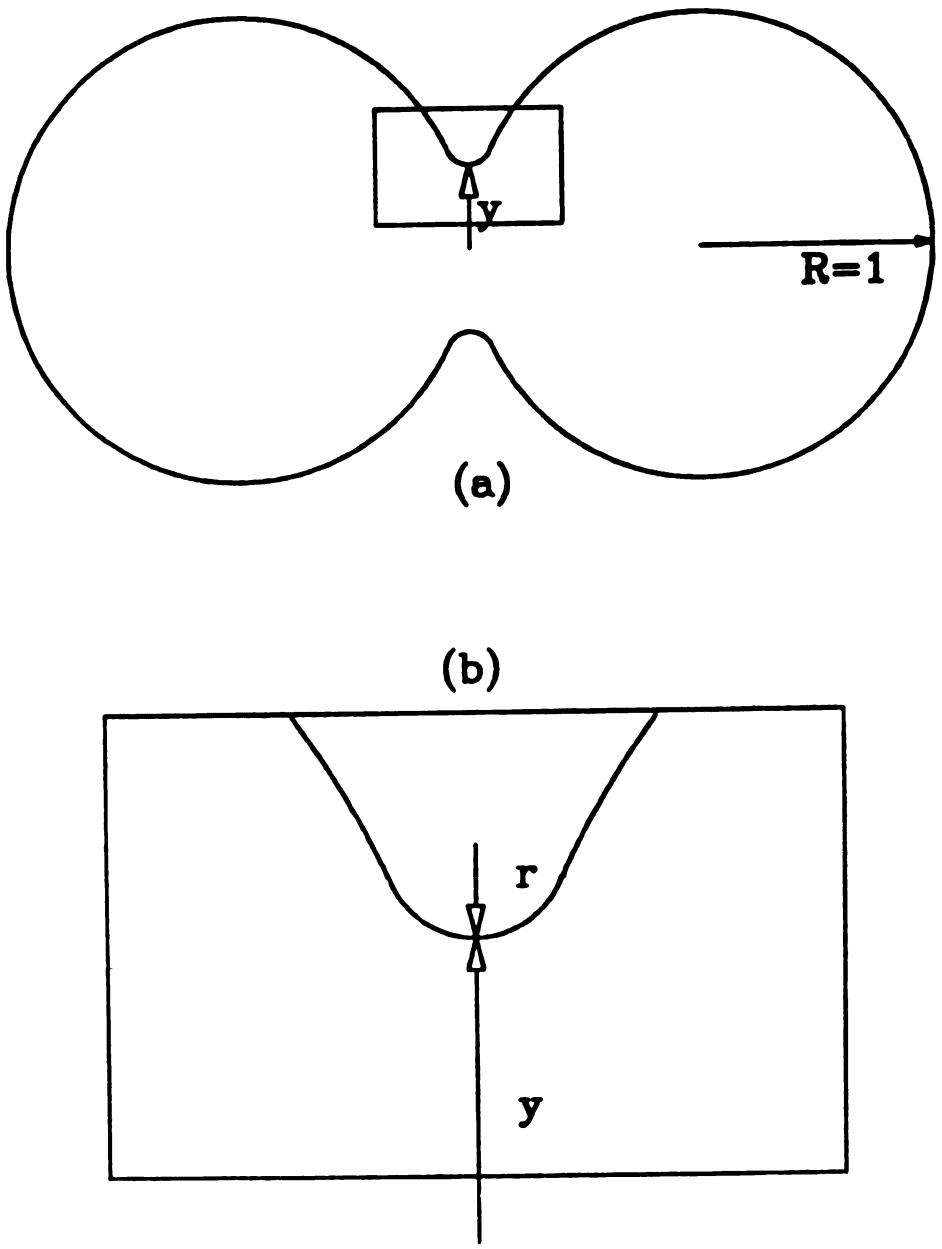

Figure 2.3: Two touched droplets as an initial profile for numerical simulations. The neck area has been smoothened using a small circle of radius r. (a): overall profile (b): magnification of neck area.

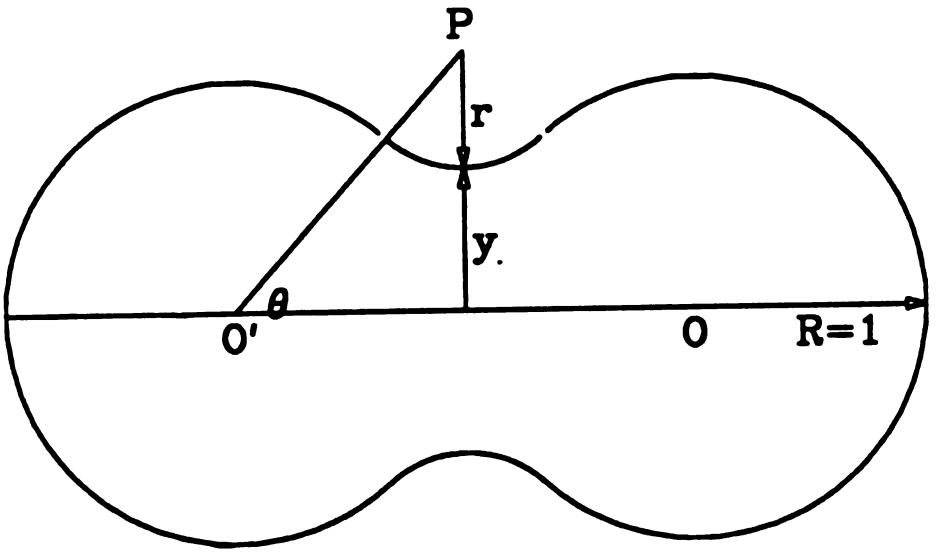

Figure 2.4: Geometrical illustration of two droplets with a connecting neck, showing the relationship between r and y: $r = y^2 / 2(1-y) \approx y^2 / 2$

One of the very interesting applications of equation (2.14) is the estimation of the complete coalescence time of two droplets of size R with a very small neck connecting them (Figure 2.3). The neck area is approximately the shape of a circle of radius r. The geometrical relationship between y, the neck size and r is better illustrated in Figure 2.4. Actually, the growth in the neck area is extremely rapid when y is small because of the large curvature. Here we roughly estimate how fast y grows when r is small. Using R=1, we can write down an approximate dynamic equation for y: $\dot{y} = B\partial \mathrm{K}/\partial s^2$. Notice that $r \cong y^2/2$ and $\partial \mathrm{K}/\partial s^2 \approx (2/r)/(\pi^2 r^2)$, for very small y, therefore, $\dot{y} = B(16/\pi^2)y^{-6}$ or $t \approx 0.1y^7/B$. Suppose y=0.2, t≈1.2×10^{-5}/B. In order to perform numerical calculations, one needs to convert the equation (2.13) into dimensionless form, which is given by:

$$\frac{\partial N}{\partial \tau} = \nabla_s^2 \kappa \qquad (2.22)$$

where $N = n/R_0, R = r/R_0, S = s/R_0, \kappa = \mathrm{K}R_0, \tau = Bt/R_0^4$. It is convenient to express K and the Laplacian in terms of polar coordinates (R,θ).

$$\frac{\partial^2 \kappa}{\partial s^2} \Rightarrow \frac{1}{\sqrt{R^2 + R'^2}} \frac{\partial}{\partial \theta} \frac{d\theta}{ds} \frac{\partial \kappa}{\partial \theta} \qquad (2.23)$$

From the illustration diagram Figure 2.5, the curvature is defined as $\partial\psi/\partial s$. The relationship between θ and ψ is

$$\psi = \theta + \pi/2 - \tan^{-1}(R'/R) \qquad (2.24)$$

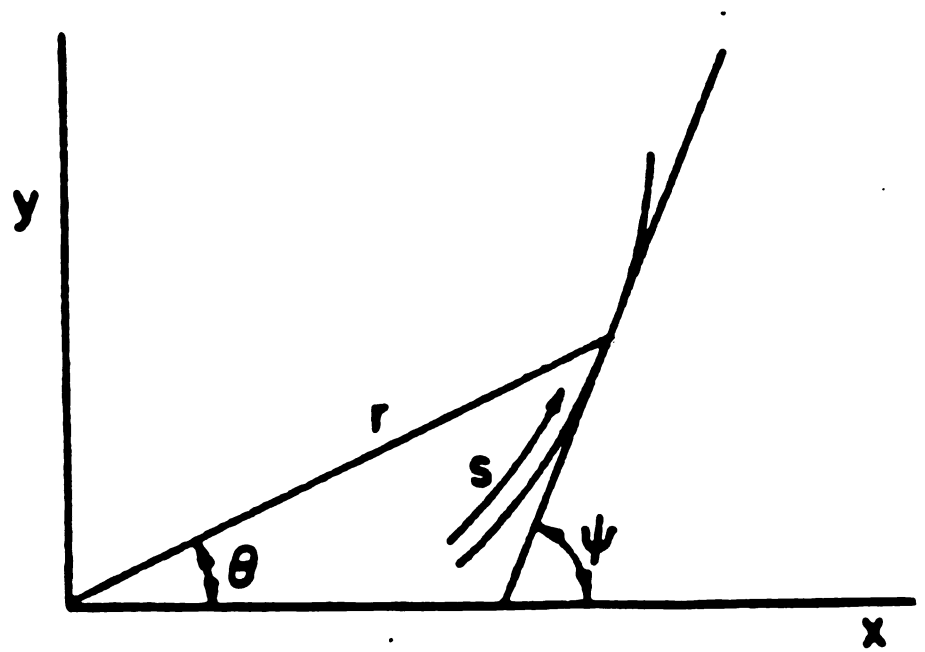

Figure 2.5: Illustration of a surface segment, showing the definition of ψ and θ and their relationship, from which the curvature can be expressed in polar coordinates (r,θ).

Therefore, the equation upon which numerical calculation is performed can be written as:

$$\frac{\partial R}{\partial \tau} = \frac{1}{R}\frac{\partial}{\partial \theta}\frac{1}{\sqrt{R^2 + R'^2}}\frac{\partial \kappa}{\partial \theta} \qquad (2.25)$$

where $R' = \partial R / \partial \theta$. In same notation, κ is expressed as

$$\kappa = \frac{R^2 + 2R'^2 - RR''}{(R^2 + R'^2)^{3/2}} \qquad (2.26)$$

The surface shape is described by the function $R(\theta)$. I employed the standard finite difference method to evaluate the derivatives. Convergence requires that the von Neuman stability criteria is

$$\delta\tau < \delta\theta^4 \qquad (2.27)$$

Figure 2.6 shows how the surface shape evolves with time. Because of the extremely large curvature near the neck area in the early stage, the neck increments very rapidly. The plot shows three stages of shape change: early neck growth, neck elimination(at time t=0.17) and complete coalescence(at time scale 1.0). As a matter of fact, the neck increments from an initial y=0.05 to 0.6 within time scale 10^{-2}. The process slows down significantly when $y \geq 0.7$. Figure 2.7 explicitly demonstrates the temporal growth of neck, showing that the growth speed is very large at the beginning and slows down, eventually turning into an equilibrium shape. Our calculation results are consistent with experimental observations(Nichols and Mullins,1965). During the process of coalscence of two droplets, the surface energy decreases

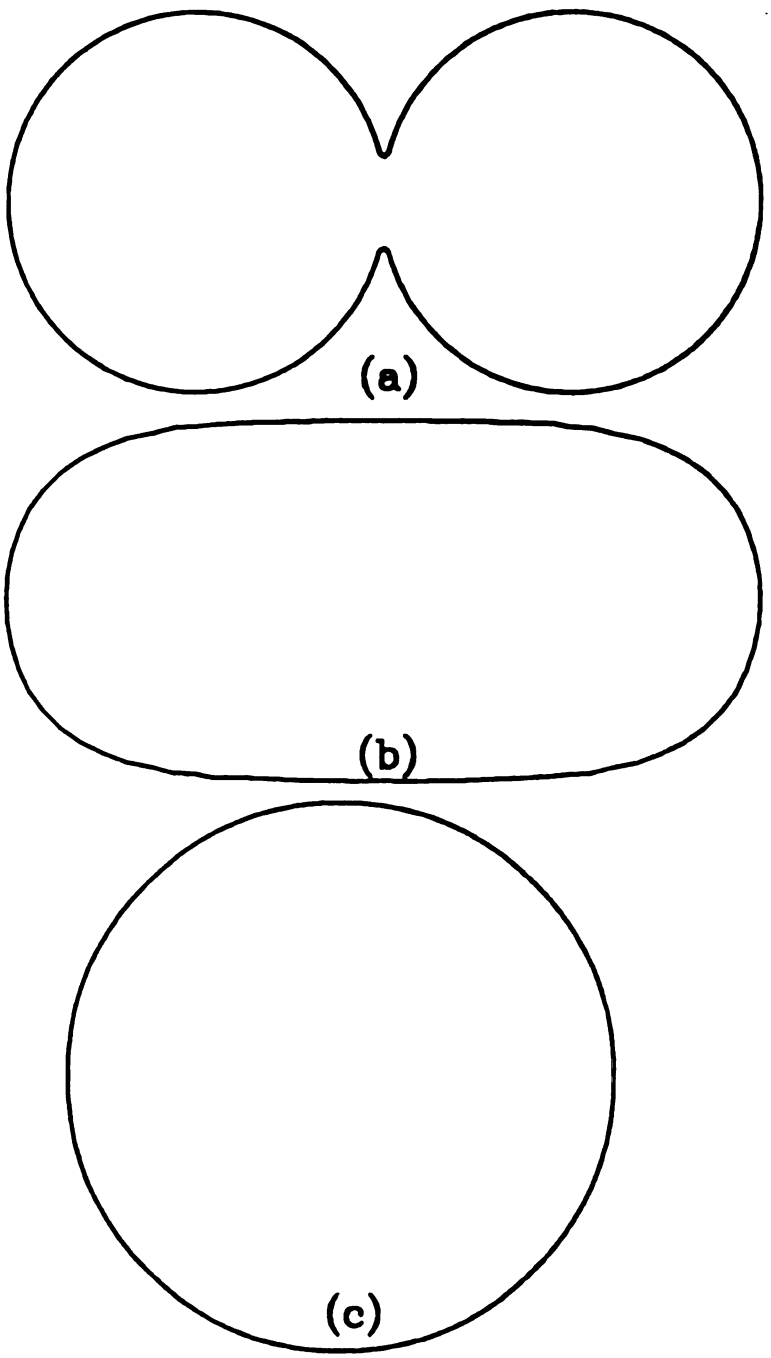

Figure 2.6. The droplets shape as a function of simulation time. The figure shows three different coalescence stages: (a): early stage: y=0.55, t=0.008; (b): neck elimination: y=0.90, t=0.17 and (c): full coalscence: y=1.42, t=0.90.

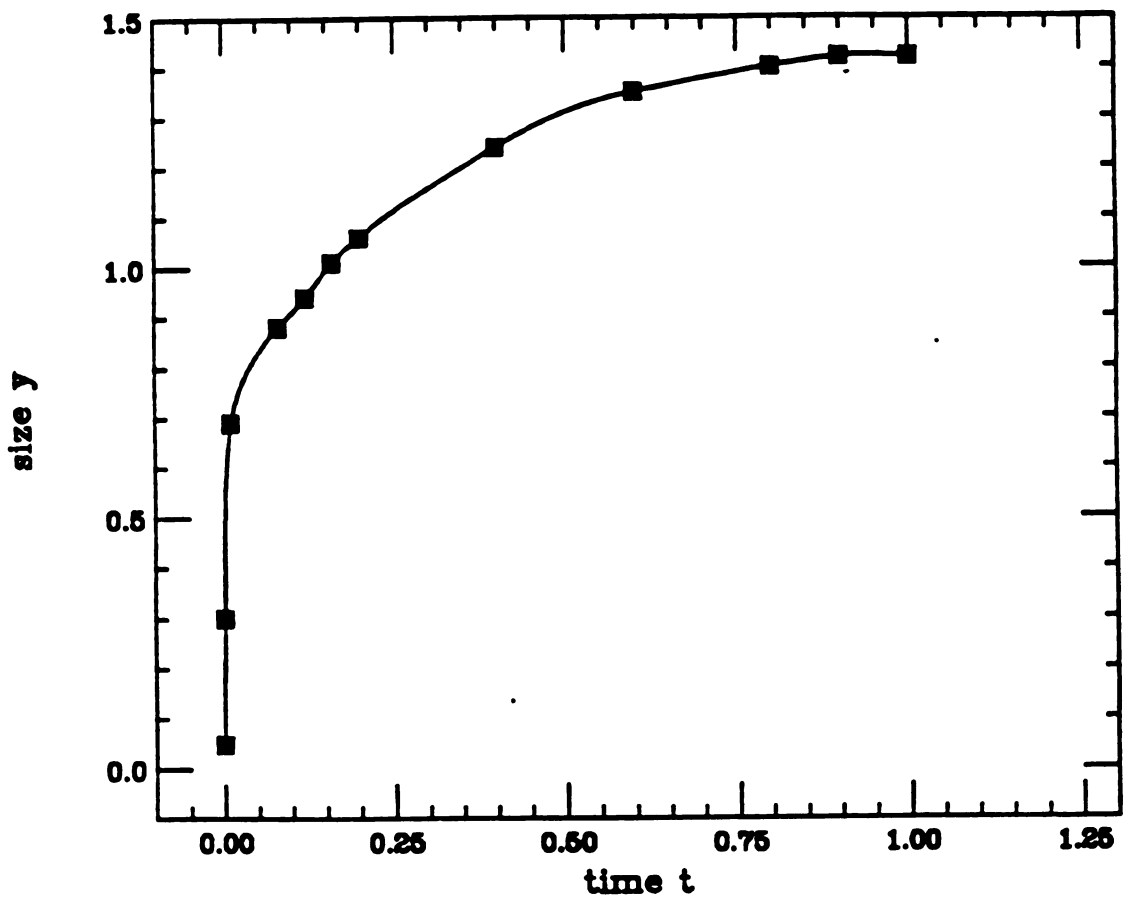

Figure 2.7: The temporal growth of the neck size y. The growth is extremely rapid in the early stage, and it slows down after reaching a certain size, particularly after neck elimination.

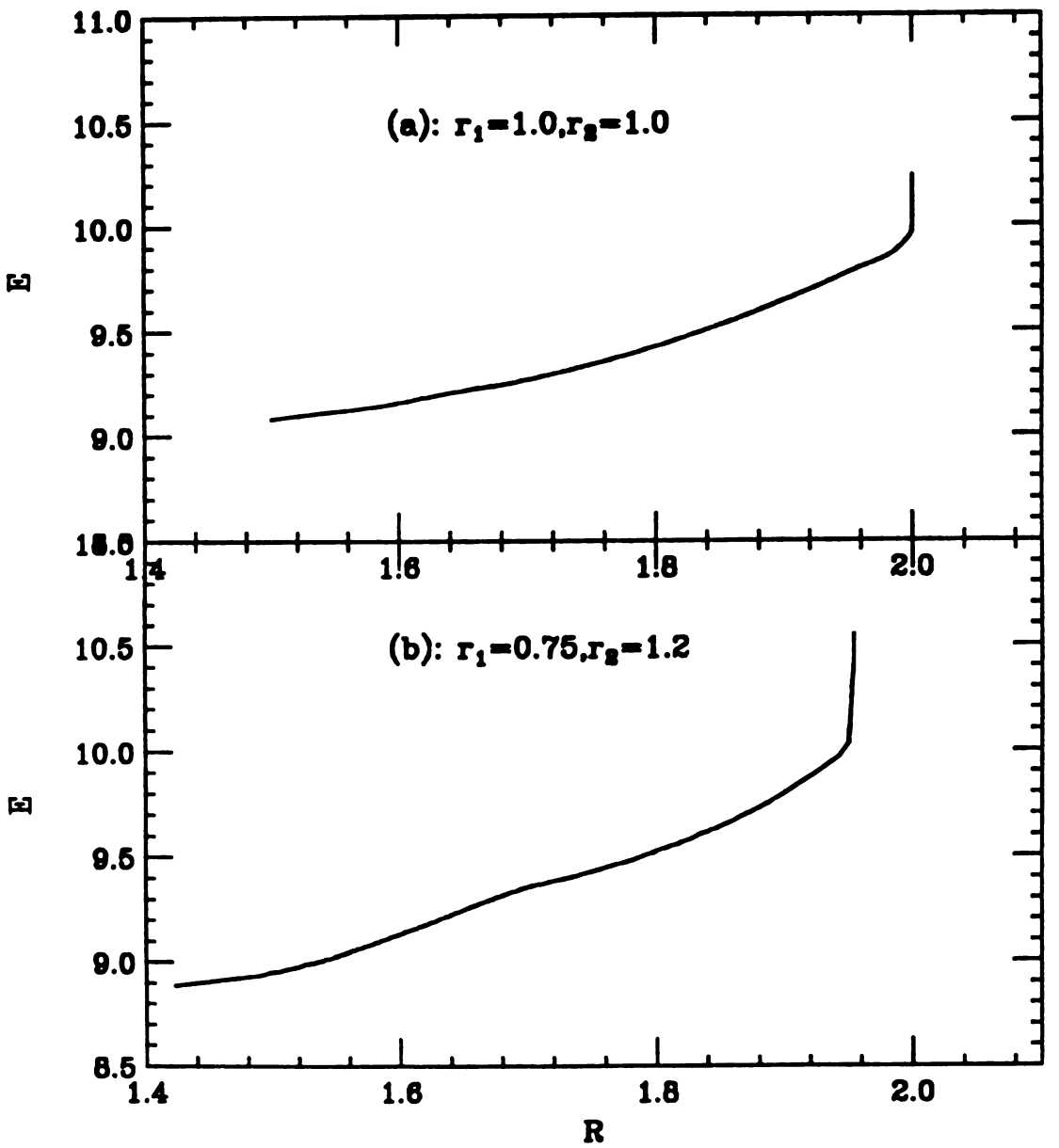

Figure 2.8: Surface energy as a function of droplet sizes. The surface energy is directly related to total area or length of the droplet surfaces. The droplet size is represented by the distance between two farthest point on the surface. (a): two equal size droplets (b): two droplets having different sizes.

as the system approaches equilibrium. We studied how the surface energy is altered as the system size and the distance distance between two droplets various. This is shown in Figure 2.8. At the early stage, the relaxation process in the neck area is so rapid that the system size does not change at all while surface energy decreases rapidly.

2.3 Crystal Shape Below the Roughening Temperature

2.3.1. Anisotropic effect of surface tension

The continuum surface diffusion theory has had much success especially in the temperature region $T>0.75T_m$ close to the melting temperature. As T is decreased to below T_R, the crystal tends to develop facets on its surface which has been intensively studied by experimental physicists during the last decade(Jayaprakash etc.,1983). Most experiments were done on metals at room temperature, much lower than their melting temperature. The samples are prepared with periodic surface profiles and exposed directly to an electron microscope which records the shape as a function of time. It is observed that facets start to take shape at tops and bottoms of the initial curve. At the beginning the process is quite fast but slows down as the size of facets becomes large. From the isotropic continuum model, this phenomena is not expected to happen because a sine curve is

a eigenfunction of the equation so that the sinusoidal shape is preserved and only its amplitude decays exponentially.

As pointed out by *Landau* (Landau, 1986), the surface tension γ of a planar solid surface depends on the crystallographic orientation θ of the sample. Thus as we calculate chemical potential, the modified Gibbs-Thompson relationship is utilized. When $T < T_R$, the surface tension γ has a cusp point at θ=0. Near this point:

$$\gamma(\theta) = \gamma_0 + \gamma_1|\theta| \tag{2.28}$$

When substituting equation (2.28) into equation (2.15), immediately we have the difficulty that the second derivative of γ(θ) is singular(a δ-function) at θ=0. The dilemma was first circumvented by *Bonzel* and coworkers (Bonzel etc.1984; Preuss,1986) mathematically by regularizing the δ-function.

For better illustration, again we consider a one-dimensional surface z(x). The equation of motion for the surface is written as:

$$\frac{\partial n}{\partial t} = \frac{B}{\gamma_0}\frac{\partial^2}{\partial s^2}\left[\gamma(\theta) + \frac{\partial^2 \gamma}{\partial \theta^2}\right]\mathrm{K}(x) \tag{2.29}$$

The above equation is greatly simplified using small slope approximation z'<<1 and reads

$$\dot{z} = -\frac{B}{\gamma_0}\eta''(x) \tag{2.30}$$

where prime represents differentiation with respect to x and

$$\eta(x)=\left[\gamma(\theta)+\frac{\partial^2\gamma}{\partial\theta^2}\right]z'' \qquad (2.31)$$

Here θ is also a function of x and θ≅z' for small slope. To regularize the singularity of the second derivative of γ, the key substitution is to replace θ with $\sqrt{\theta^2+\theta_0^2}-\theta_0$, with parameter θ_0 being very small. This substitution does not change the γ(θ) much when θ>>θ_0 but provides finite second derivative of γ(θ) near θ=0. Equation (2.31) turns into:

$$\eta(x)=\left[\gamma_0+\gamma_1(\sqrt{z'^2+\theta_0^2}-\theta_0)+\frac{\gamma_1\theta_0^2}{(z'^2+\theta_0^2)^{3/2}}\right]z'' \qquad (2.32)$$

by replacing γ with $\gamma_0+\gamma_1(\sqrt{\theta_0^2+z'^2}-\theta_0)$. To analyze the overall behavior of this equation, we regard z', z", z'" and z"" as small so that the second term on the right hand side is always small compared with the first term. Combining equation (2.30) with equation (2.32), we have the simplified differential equation:

$$\dot{z}\approx -Bz''''-\frac{B\gamma_1}{\gamma_0}\frac{\partial^2}{\partial x^2}\frac{z''\theta_0^2}{\left(\theta_0^2+z'^2\right)^{3/2}} \qquad (2.33)$$

The first term is the classical surface healing term obtained by Mullins(Mullins,1957) and the second term embodies the effect of anisotropic surface tension and vanishes if $\theta_0=0$ and z'≠0. This equation can be discussed in two specific regions. First in the region where z'≤θ_0, equation (2.33) becomes

$$\dot{z}\approx -Bz''''-\frac{B\gamma_1}{\theta_0\gamma_0}z'''' \qquad (2.34)$$

Typically $\gamma_1/\gamma_0 \approx 0.1$, while θ_0 is taken to be less than 10^{-3}, therefore, the second term on the right hand side dominates. In the region that $z' >> \theta_0$, the second term is negligible compared to the first term. The speed of decaying in the regions of $z' \leq \theta_0$(flat region) is much faster than in the other region, therefore an appreciable shape change of the surface profile occurs at the tops and bottoms where facets are initially developed.

The direct solution of equation(2.29) through numerical methods is obtained by imposing periodic boundary conditions and a sinusoidal form as an initial condition. Figure 2.9 presents a sequence of surface shapes versus time. It is clear that facets show up at the bottoms and tops of the curve almost immediately after the simulation is started. The size of those facets increases with time while the height decreases and Figure 2.10 exhibits that time evolution. Our calculation data shows that the facet width increases with time t very rapidly at early stages and slows down after reaching size of order one. Just prior to the disappearance of facets(due to completion of flattening), the widening speed increases again. The result is very similar to the calculation by Lancon and Villain (Lancon and Villain,1990) who utilized the evaporation-condensation dynamics and miscut model that is the topic of next subsection.

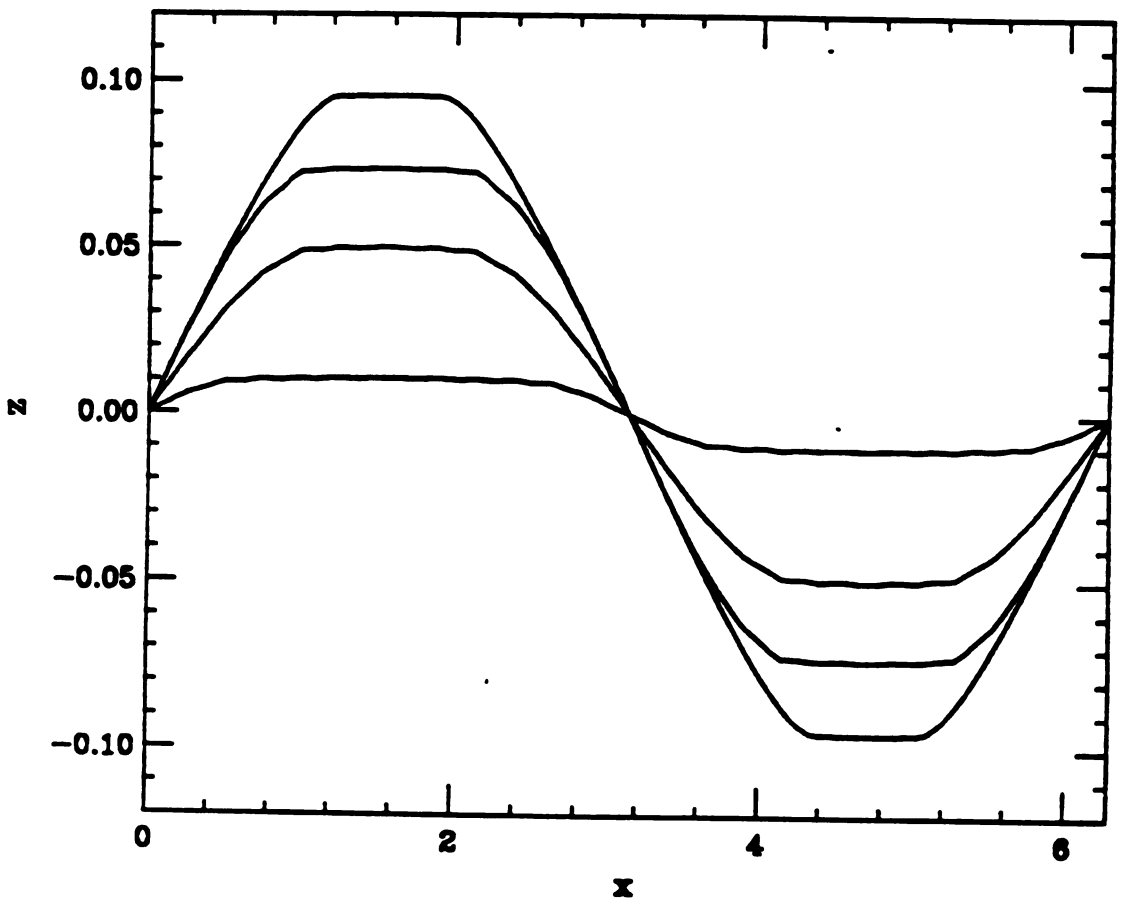

Figure 2.9: Numerical solution to equation (2.29), showing the surface profile decaying. The initial shape is sinusoidal. The formation of facets occurs at the tops and bottoms while the shape between facets approximately maintains a sinusoidal solution.

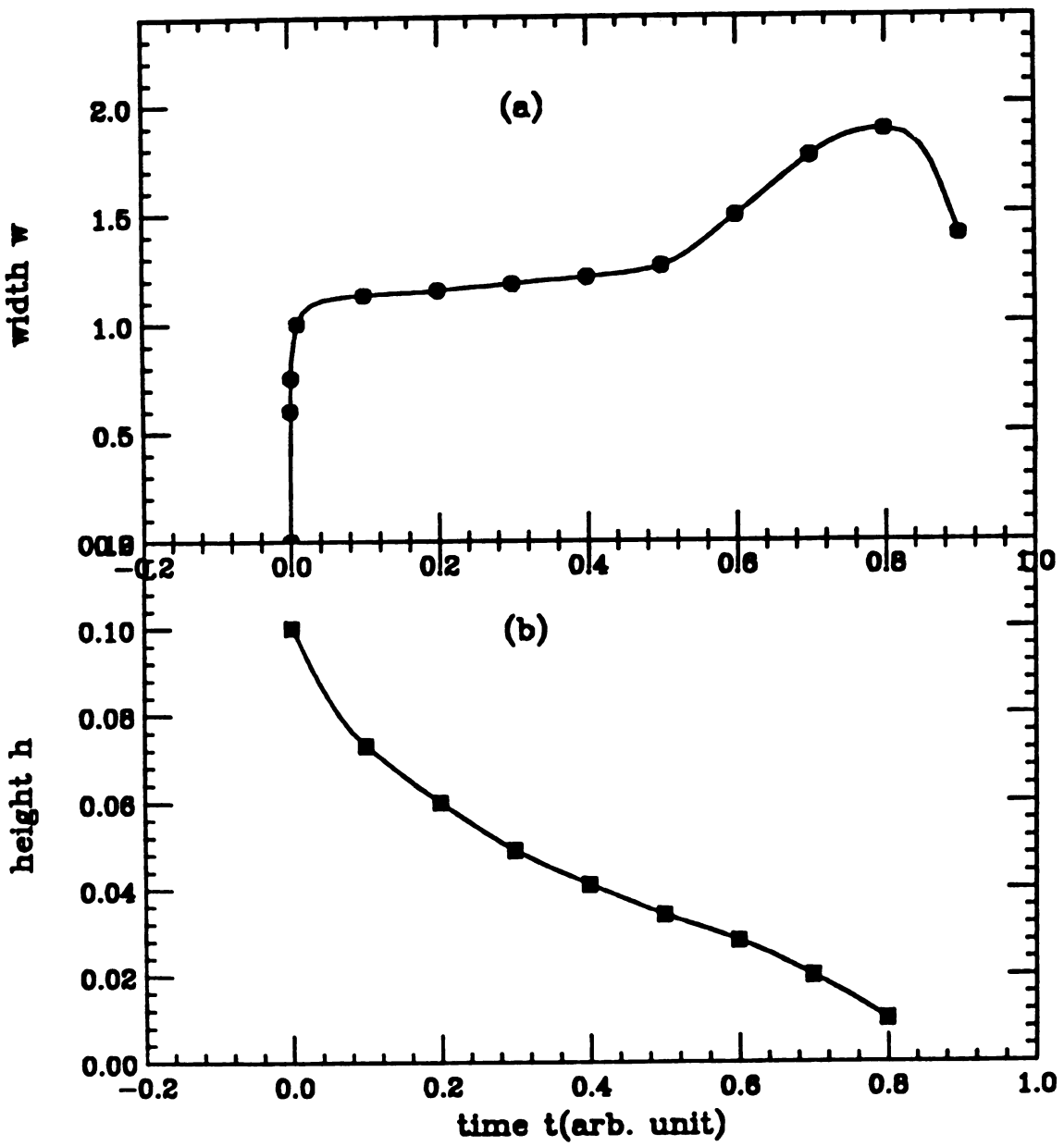

Figure 2.10: The size and height of those facets indicated in Figure 2.8 as functions of time. (a): the facet size grows with time rapidly at early stage, slows down after the size reaches the order of 1 and vanishes as approaching equilibrium. (b): the vertical position of facets decreases monotonically.

2.3.2 Miscut model:

We start with equation (2.7) to calculate the chemical potential. When $T<T_R$, the surface consists of well developed steps and terraces and the surface shape change is due to the motion of steps. In general, σ can be viewed as the sum of two contributions: σ_0, the free energy of terraces and σ_s, the energy of steps. Further σ_s can be written as $\sigma_s = \sigma_1 + \sigma_3$, where σ_1 is the free energy of non-interacting steps, which is proportional to the step density; σ_3 is the interaction between steps. The existence of σ_3 is due to the fact that two adjacent steps tend to be away from each other such that they could have more space to wander around. A detailed investigation(Gruber and Mullins, 1967) shows that σ_3 is proportional to the third power of step density. Summarizing the above argument, σ has the following approximate expression:

$$\sigma = \sigma_0 + \gamma_1|u| + \tfrac{1}{3}\gamma_3|u|^3 \qquad (2.35)$$

where $|u| = (z'^2_x + z'^2_y)^{1/2}$, representing the step density. If we substitute equation (2.35) into equation (2.7), the chemical potential is still singular at u=0. However Lancon and Villain found that if the lattice planes of high symmetry are not perfectly aligned with the surface, but instead have a small "miscut" angle, evaporation-condensation dynamics leads to the formation of facets on the tops and bottoms of

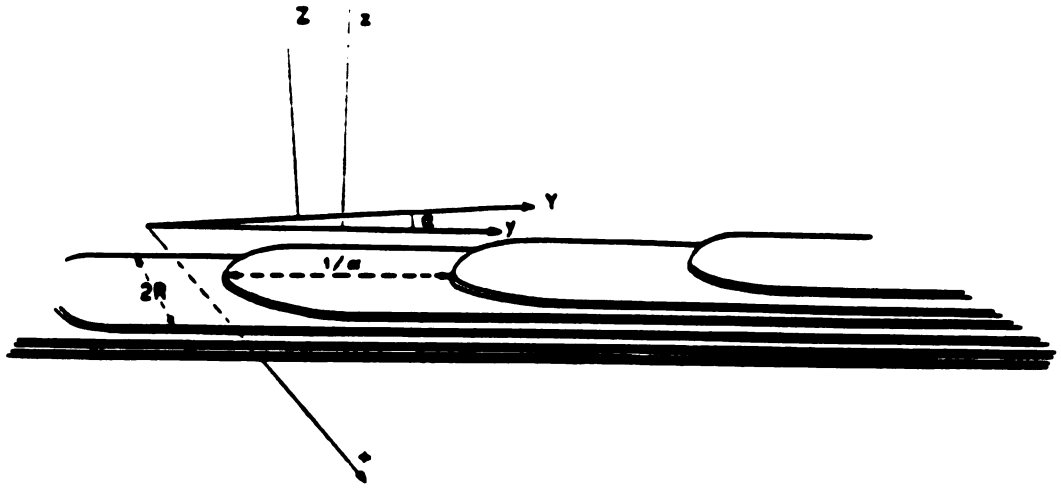

Figure 2.11: A geometrical picture of the miscut model, showing that the lattice planes(x-y plane) and surface(X-Y plane) has a small angle α. It also shows the steps and terraces.

an initial sinusoidal surface. Here we apply the model to the case of surface diffusion dynamics.

In the miscut model, the lattice planes of high symmetry (e.g. Au 111) are not perfectly parallel to the surface, and they makes a small angle α with the y-axis of a surface whose geometric setting is shown in Figure 2.11. Consequently, each lattice plane will have an intersection y_n at the y-axis. Let y_n and z be functions of x only, then z and y_n have the relationship:

$$z(x,t) = y_n(x,t)\sin\alpha + n\cos\alpha \qquad (2.36)$$

where n stands for the numbering of lattice planes. The chemical potential μ is calculated by inserting equation (2.35) into (2.7) and setting $z'_y = \alpha$.

$$\mu - \mu_0 = -\frac{\partial}{\partial x}\left[\frac{\partial}{\partial z'}[\sigma_1(z',\alpha)+\sigma_3(z',\alpha)]\right] \qquad (2.37)$$

where $\sigma_1 = (z'^2+\alpha^2)^{1/2}$ and $\sigma_3 = \frac{1}{3}\gamma_3(\alpha^2+z'^2)^{3/2}$. The equation of motion for z(x,t) is then written according to surface diffusion dynamics:

$$\frac{\partial z}{\partial t} = -B\frac{\partial^2}{\partial x^2}w \qquad (2.38)$$

and here

$$w = \left[\frac{\alpha^2}{(\alpha^2+z'^2)^{3/2}} + \frac{\gamma_3}{\gamma_1}\frac{2z'^2+\alpha^2}{(z'^2+\alpha^2)^{1/2}}\right]z'' \qquad (2.38a)$$

Again we can analyze equation (2.38) in two distinct regions. First consider the region where $z' \le \alpha << 1$, the second term of equation (2.38a) is small compared with the first term, and hence equation(2.38) is reduced to

$$\dot{z} = (-B/\alpha)z'''' \qquad (2.39)$$

This is a linear differential equation whose solution is simply $z(t) = z(x,0)\exp(-Bk^4 t/\alpha)$ for the initial curve $z(x,0) \sim \sin(kx)$, and thus the decay is very rapid. When z'>>α, equation(2.38) turns into:

$$\dot{z} = -B_3 \frac{\partial^2}{\partial x^2}(|z'|z'') \qquad (2.40)$$

The solution to equation (2.40) has been studied by Ozdemir and Zangwill (Ozdemir and Zangwill, 1990) and it was found that:

$$z(x,t) = z(x,0)/(1+\lambda t) \qquad (2.41)$$

where λ is constant. The shape preserving solution can be fitted very closely to a sinusoidal function. Because of the extremely large decay speed in the region where $z' = \theta_0$, the overall surface profile is broken into two kinds of regions: one is totally relaxed and located at tops and bottoms of the surface(facets); the other regions are those between facets whose decaying behavior is governed by equation (2.40).

We studied the numerical solution of equation (2.38) using finite difference methods. The initial condition has been set to be sinusoidal again. Because a sine-curve is not the eigenfunction of equation (2.40), it is anticipated that the surface profile between two facets will slightly deviate from its initial shape as seen from Figure 2.12. This plot

shows that right after the simulation started, small facets have been created at the tops and bottoms of the initial sine curve. The size of facets grows with time while the vertical position(height) of facets decreases(Figure 2.13). It is noticeable that the behavior described by equation (2.38) is very similar to that discussed in the previous subsection. Actually, if we regard the miscut angle α as the parameter θ_0, the surface tension in the anisotropic model has the form: $\gamma = \gamma_0 + \gamma_1(\alpha^2 + z'^2)^{1/2}$ which will certainly give the same result as using the substitution $\theta \to \sqrt{\theta^2 + \theta_0^2} - \theta_0$. The miscut angle α thus provides a physical explanation of θ_0 introduced in the anisotropic model.

To conclude, a non-equilibrium crystal surface alters its profile mainly through surface diffusion when the bulk chemical potential is close to that of the environment the crystal resides in. Above the roughening temperature, the diffusion process is governed by a continuum model in which the chemical potential on the surface is proportional to the curvature and consequently a diffusion-like equation that relates the alteration rate and its surface geometry can be derived to closely describe the diffusion process. When below the roughening temperature, the diffusion process is complicated owing to the fact that the surface tension has cusp singularity points in the direction of the crystal planes of high symmetry. To circumvent this difficulty, two

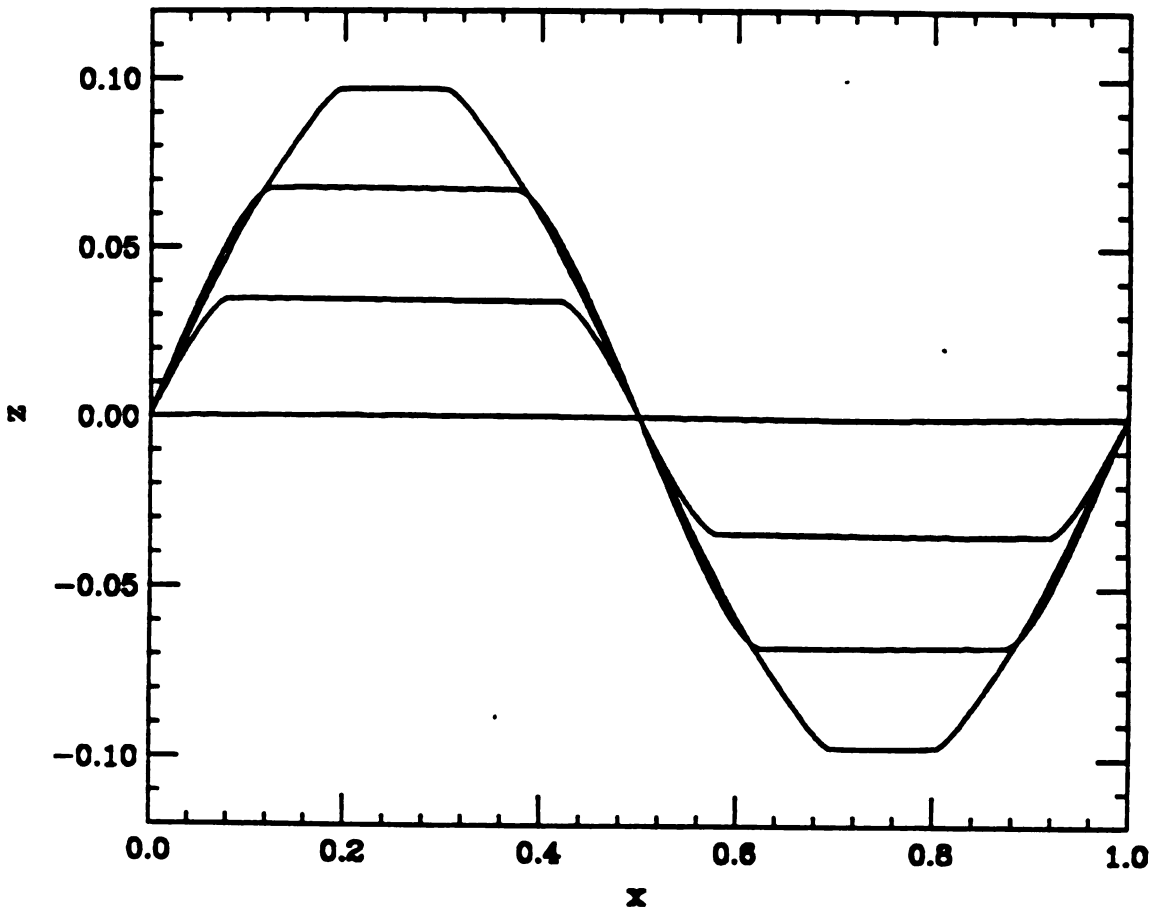

Figure 2.12: Numerical solution to equation (2.38), showing the formation of facets. We have set α=0.01, $\gamma_3 / \gamma_1 = 1.0$ and the initial sinusoidal amplitude is 0.1, wavelength=1.0

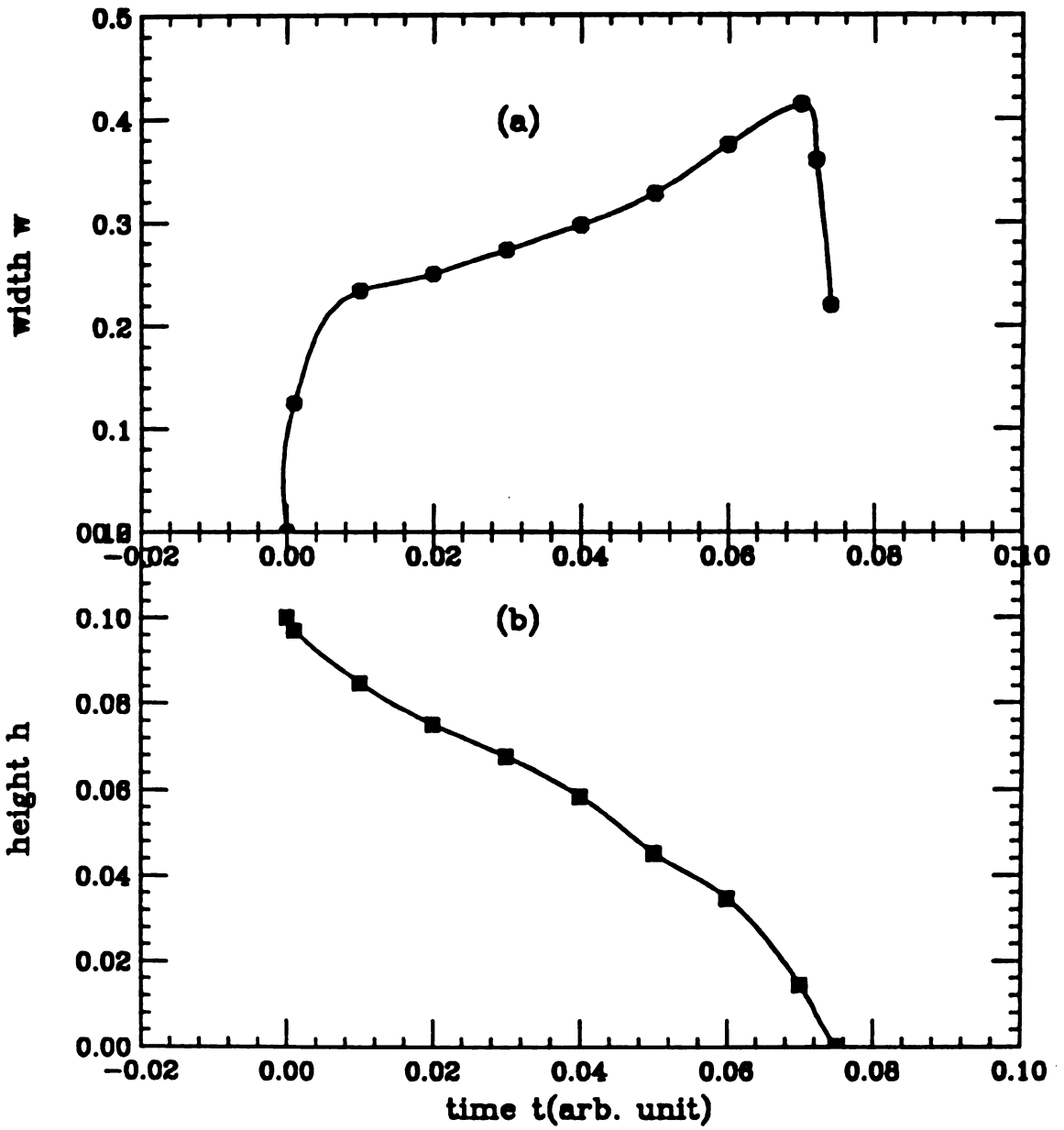

Figure 2.13: (a): Temporal growth of facet width, showing similar behavior to Figure 2.10. (b): facet height as a function of time, the decay is monotonic.

different models have been presented. The first is to desingularize the cusp point by making the second derivative of the surface tension finite through introducing a small constant. Consequently, the corresponding differential equation governing the diffusion process yields solutions that can explain the experiments that facets are observed at certain locations. The second model studied the chemical potential in more detail and proposed that the formation of facets is possible when the surface is not perfectly parallel to the lattice plane, but with a small miscut angle α. If one regards the small parameter θ_0 as α, the two models are mathematically very similar.

CHAPTER THREE

MORPHOLOGY OF THIN METAL FILMS

3.1 Introduction

From an experimental point of view, thin metal films can be prepared by a wide variety of techniques. The most common method of preparing thin films is the so-called evaporation method(Pashley,1965). This involves condensing the metal onto a substrate with the vapor source being provided by evaporation. The first important factor influencing film growth is the quality of the vacuum in which the evaporation is carried out. It is quite clear that the various types of chemically reactive or condensable contaminants which are present in such a system could have a major influence on the growth and structure of the films. Modern vacuum technology has enabled the production of high quality vacuums with pressures of 10^{-11} torr(Umbach etc.,1991), which provides a very clean condition for deposition studies. Many different techniques are utilized for providing vapor sources, the simplest being a tungsten or molybdenum spiral which is heated by passing an electric current through it. The rate of deposition, and the final film thickness , often needs careful control, since the structure of a deposited film can depend considerably upon both parameters. It is common to

heat the substrate during deposition. The heating can have important effects in relation to the cleaning of the substrate, as well as enhancing recrystallization effects and general structural changes during growth, which can be important for increasing grain size. The invention and improvement of electron microscopy have changed the method of surface investigation significantly. The electron microscope has a number of advantages for studies on thin film growth: (1) the very high magnifications possible, associated with a resolution below 1nm, allow very detailed study of localized regions of specimens; (2) selected area electron diffraction allows detailed correlation between the image and the electron diffraction pattern; (3) internal crystallographic structure can be detected and analyzed in detail; (4) direct observation of the growth of thin films can be made by carrying out the deposition inside the microscope. Figure 3.1 gives snapshots of the morphology of an indium film on a silicon oxide substrate. In the next section, I will discuss some interesting features of those diagrams and present a theoretical model to simulate the formation of these features.

3.2 Coalescence and Percolation in thin metal films:

As shown from many experiments(Paudit etc.,1982), most metals do not wet insulating surfaces such as glass,

graphite or silicon. In such case a thin film grown by thermal evaporation passes through a sequence of morphological changes as the film thickens. When sufficiently thin, the film consists of isolated, compact islands which, as more material is deposited, grow and coalesce into larger, but still compact islands. At some critical island size, islands that touch no longer fully coalesce into near-equilibrium compact shapes but instead form elongated wormlike structures. As growth proceeds, these "worms" grow longer and connect to form a percolating structure, and finally, the channels between worms fill in to form a continuous, hole free, film. This morphological sequence is illustrated in Figure. 3.1 which shows an indium film evaporated onto a room temperature SiO_2 substrate. For this film, the critical area coverage for percolation is quite high (p_c=0.82), a result of the fact that the channels between worms are very long and narrow compared to the width of the worms. High p_c is a puzzling feature of the morphology of many metal films grown on warm substrates.

As can be seen in Figure 3.1, in the early stage of growth, the film has a distinctive morphology, consisting of compact islands, all of about the same size, separated by gaps which are comparable to or smaller than the island radius. Actually, the gaps are filled with a population of smaller islands which do not show well in these SEM

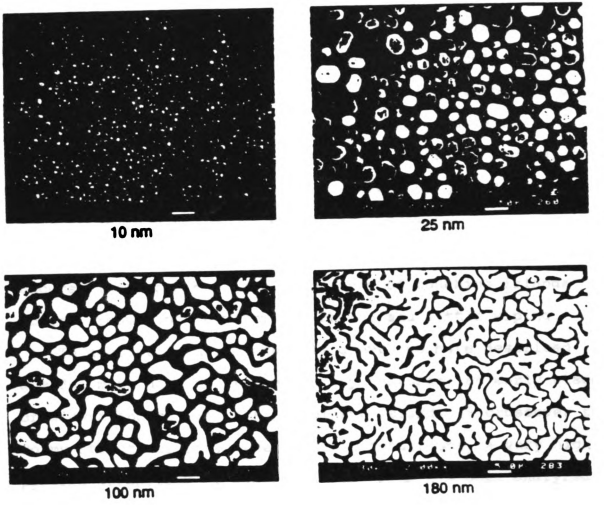

Figure 3.1: SEM images of indium on an SiO_2 substrate, showing different stages: the early complete coalescence; partial coalescence; wormy structure; percolation and hole filling.

photographs. During film growth, islands are always growing because of deposition of new material and accretion of smaller droplets at the island perimeter. In this early growth stage, when two islands touch, they quickly coalesce in to a larger island, and in doing so, wipe clean part of the substrate which was covered. This wiping action constantly creates gaps comparable to the island radius, and results in ever-larger islands separated by gaps filled with smaller islands nucleated since the last wipe.

At a later stage of growth, full coalescence no longer occurs. Instead a partial coalescence of touching islands occurs, resulting in wormy structures and little wiping.

To accurately mimic the film growth we have described , a model must have the following key features: an early stage of growth and coalescence of compact islands, a crossover to wormy structures and, under certain conditions, a very high p_c. The morphology of discontinuous films has been analyzed in terms of percolation models. Various geometrical exponents (fractal dimensionality, correlation length etc.) have been measured in real films and are found to coincide with values found in 2D pure percolation patterns. It may therefore be natural to assume that simple lattice model with short range attractive interactions will accurately reproduce the morphology of real discontinuous films. However, we have found that a large class of lattice models

fail to reproduce the essential phenomena of island coalescence, worm growth, and high p_c that occurs in the growth of many thin metal films on room temperature substrates.

The long and intertwined worms seen in Figure 3.1 (lower right) appear to be repelling each other. We will show that a simple continuum model which incorporates the essential feature of interrupted coalescence of large islands and which contains only short-ranged attractive interactions accurately reproduces this apparent repulsion and high p_c which results from it.

Direct observation of growing metal films on warm substrates has verified that full coalescence occurs when the metal islands are small enough and partial coalescence occurs when the islands reach a radius greater than a critical value R_c. In the regime that we are considering, the substrate temperature is well below the droplet melting temperature and the mechanism of coalescence is surface diffusion (not bulk diffusion). The mechanism for the interruption of full coalescence beyond a critical island size is discussed in section 3.3. Here we consider R_c to be determined by experiment.

The full coalescence stage has been previously studied by Meakin and Family(Family and Meakin, 1988), and here we

extend their model to include the island-to-worm cross-over and eventual percolation.

The MFM is defined as follows. All islands are assumed to be circles (D=2 model) or spherical caps (D=3 model). Droplets of radius R_0 rain down ballistically on a substrate. If they land on a pre-existing droplet, a new droplet of size

$$R^D = R_1^D + R_2^D \qquad (3.1)$$

is generated. Here R_1 is the radius of the pre-existing droplet on the surface, while $R_2=R_0$ is the radius of the droplet that is ballistically deposited onto the substrate. D is the dimension of the depositing droplets (D=3 for spherical caps, D=2 for depositing circles). The center of the new droplet is located at the center of mass of the old droplet and the added droplet. If the new droplet now overlaps an adjacent droplet on the surface, these two droplets also coalesce according the rule (3.1). Complete relaxation of the pre-existing droplets on the surface occurs before the next new droplet is ballistically added to the surface. According to this rule of coalescence, computer simulation is easily carried out. Let the 2d coordinate (x,y) stand for the position of a droplet which has the shape of a circle. The original droplets have radius R_0 and are deposited randomly over system. The non-trivial physical quantities are the coverage of film on the substrate and the

droplet size distribution. In the case D=2, the total area covered by droplets is independent of the size distribution, therefore the coverage will be proportional to the number of deposited droplets. For D=3, the situation is different, the coalescence rule conserves volume, the height of a spherical cap is proportional to its radius. Figure 3.2 shows the droplet configurations of 3D spherical caps(Figure 3.2a) and 2D circles(Figure 3.2b) on square substrates. Indeed, they have distinct size distributions which are statistically shown in Figure 3.3. Figure 3.3a shows the droplet size distribution for the case D=3. The distribution has two maxima located near $R=R_0$ and $R=R_m$, where R_m is a length scale that grows with total deposited droplet number. The asymptotically bi-modal feature is not shared by D=2 droplets which have only one maximum near $R=R_0$(Figure 3.3b).

The interrupted coalescence model (ICM) we introduce is a natural generalization of the Meakin/Family Model(MFM) to include a cutoff radius R_c above which overlapping islands no longer coalesce. The ICM rule are thus:

a) If $R_1<R_c$ or $R_2<R_c$ droplets coalesce according to equation (3.1). The new droplet is at center of mass of the old droplets.

b) If $R_1>R_c$ and $R_2>R_c$ the droplets do not coalesce.

R_c sets the length scale at which the cross-over from the droplet to wormy stage occurs. In the ICM we must also

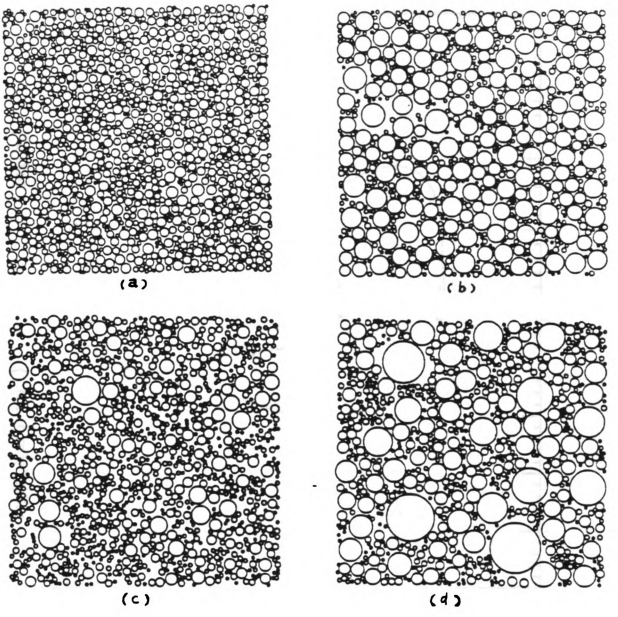

Figure 3.2: Droplet configurations on a square substrate using MFM(Meakin & Family Model): a,b: D=3. c,d: D=2.

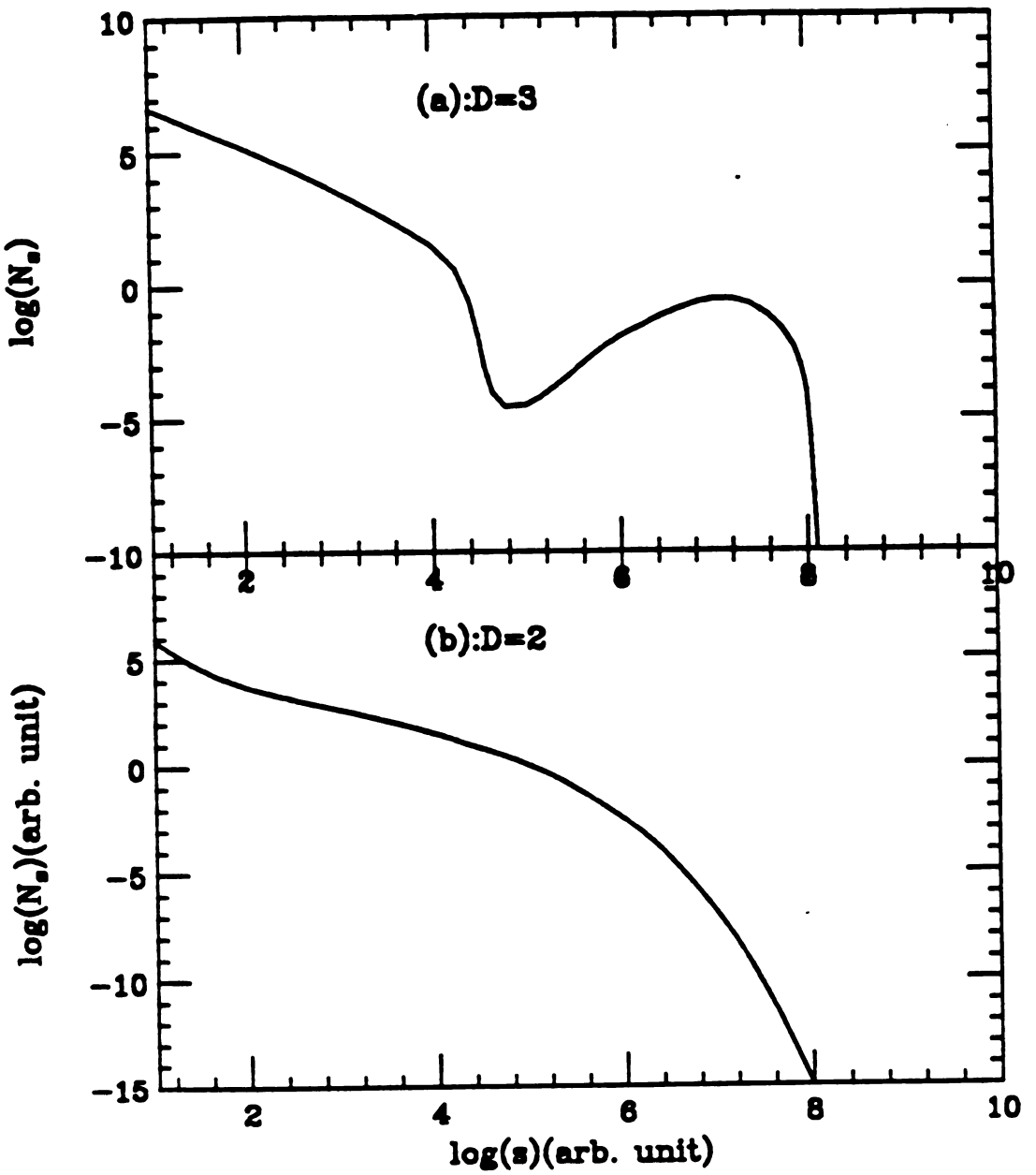

Figure 3.3: Droplets size distribution (a): D=3, showing two peaks, one is located near $R=R_0$; the other increases with the total number of deposited primary droplets. (b): D=2: the distribution is monotonic, small size droplets have a large population.

define the radius R_0 of the small droplets being ballistically deposited onto the surface, and the edge length L of the system. The important independent variables in our simulations are thus the ratios R_c/R_0 and L/R_0. We consider the D=2 and D=3 cases, but restrict our attention to 2-dimensional substrates (d=2), as the d=1 case has a trivial P_c. Finally, note that when $R_c/R_0<1.0$, no coalescence occurs, and both the D=2 and D=3 models return to the D=2 inverse Swiss cheese model ($P_c=0.676\pm0.002$).

Figure 3.4 presents the growth morphology generated by the ICM for the case $R_c/R_0=8$, $L/R_0=200$ and D=3. It is seen that in the early stages of growth, the model is very similar to the MFM. As deposition continues, the large droplets begin to overlap, until finally a percolation path of the large droplets occurs. The configuration at percolation (Figure 3.4b) shows the high percolation coverage generated by the ICM (in this configuration about 0.82).

The reason for the occurrence of high P_c is that the initial droplet state is correlated, and that percolation from this correlated state requires a higher coverage than would random percolation of discs (inverse Swiss cheese). The small droplets ($R<R_c$) do not lie on the final percolation path, so the large droplets play the dominant role. Given this, we can think of the final percolation path

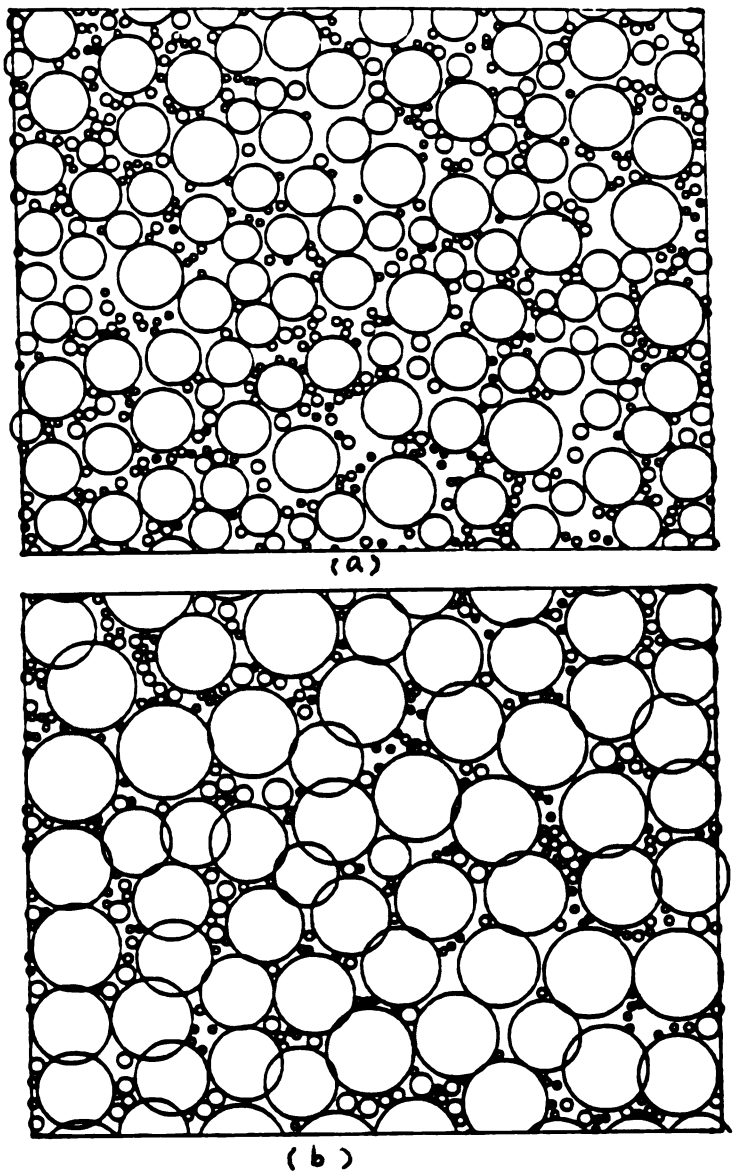

Figure 3.4: ICM simulation with L/R_0=200 and R_c/R_0=8.0. (a): The early stage. When the largest droplet size is smaller than the critical radius R_c, the ICM simuation result is identical to the MFM (b): Percolation stage: as more primary droplets deposit, those droplets whose radii are larger than R_c form a percolation structure.

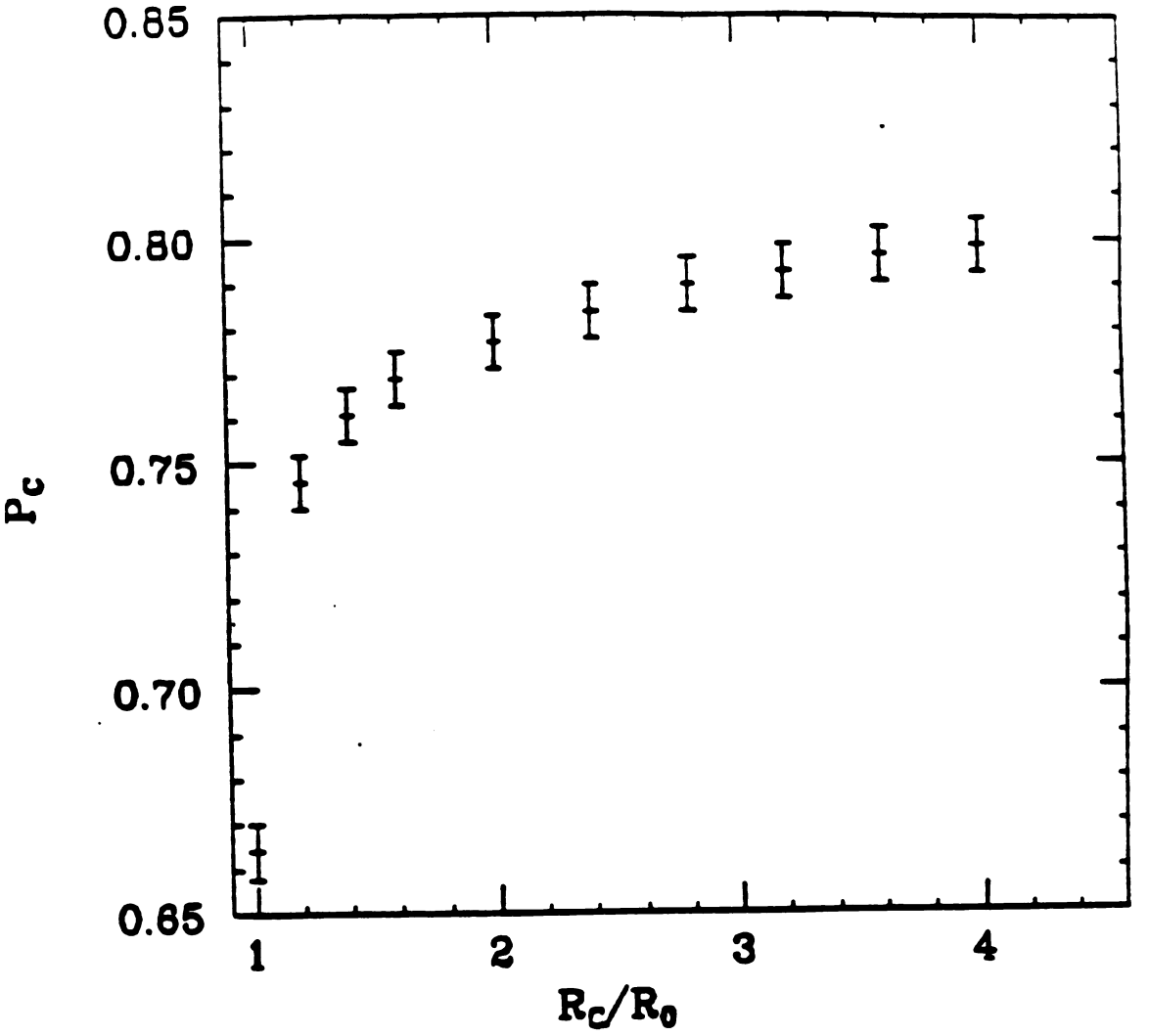

Figure 3.5: Percolation coverage as a function of R_c/R_0 for D=3: The percolation coverage is calculated from averaging 100 configurations for each point. The error bars stand for the standard deviation. As R_c/R_0 increases from 1, P_c has a big jump, which contributes to the high coverage.

as evolving from a set of repelling discs (the large droplets) with packing fraction about 0.57 (as measured on configurations such as Figure 3.4a). If we now increase the radius of these random discs (at a rate proportional to their original radius - to model the cross-section available to the ballistically depositing droplets), we naturally find a high P_c. If the original droplets lie on a triangular lattice P_c=0.907, while if the initial state is like random packing, we expect $0.82<P_c<0.89$. The point is that starting from a distribution of repelling droplets always leads to high P_c, and given an initial droplet configuration such as Figure 3.4a, it is not surprising that the ICM model does too.

It takes the MFM many iterations to settle into a self similar evolution. Prior to this equilibration time, the droplets are not as strongly correlated. We would thus expect that small R_c/R_0 implies lower P_c. This expectation is supported by the data of Figure 3.5, which shows results for P_c as a function of R_c/R_0 for D=3.

We have also studied the D=2 ICM model. Although the MFM in D=2 leads to a very different distribution of droplet sizes (bi-model in 3-D, monotonically decreasing in 2-D), the final percolation coverage in D=2 is still enhanced in the ICM. This is illustrated in Figure 3.6 which shows two

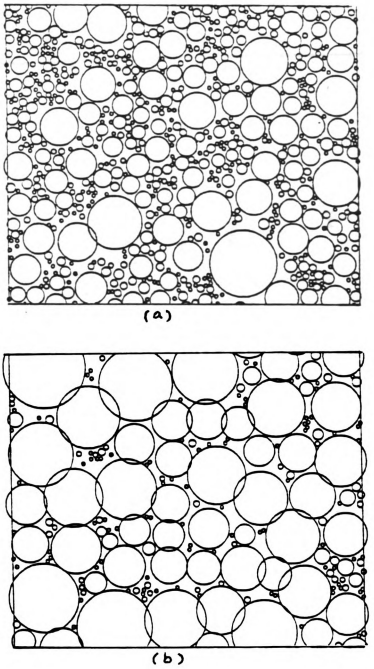

Figure 3.6: ICM simulation for D=2 with L/R_0=200 and R_c/R_0=8.0. (a) early stage: similarly the early stage is identical to the MFM case. Droplets are isolated. (b) percolation stage: the introduction of the critical radius naturally leads to the percolation structure.

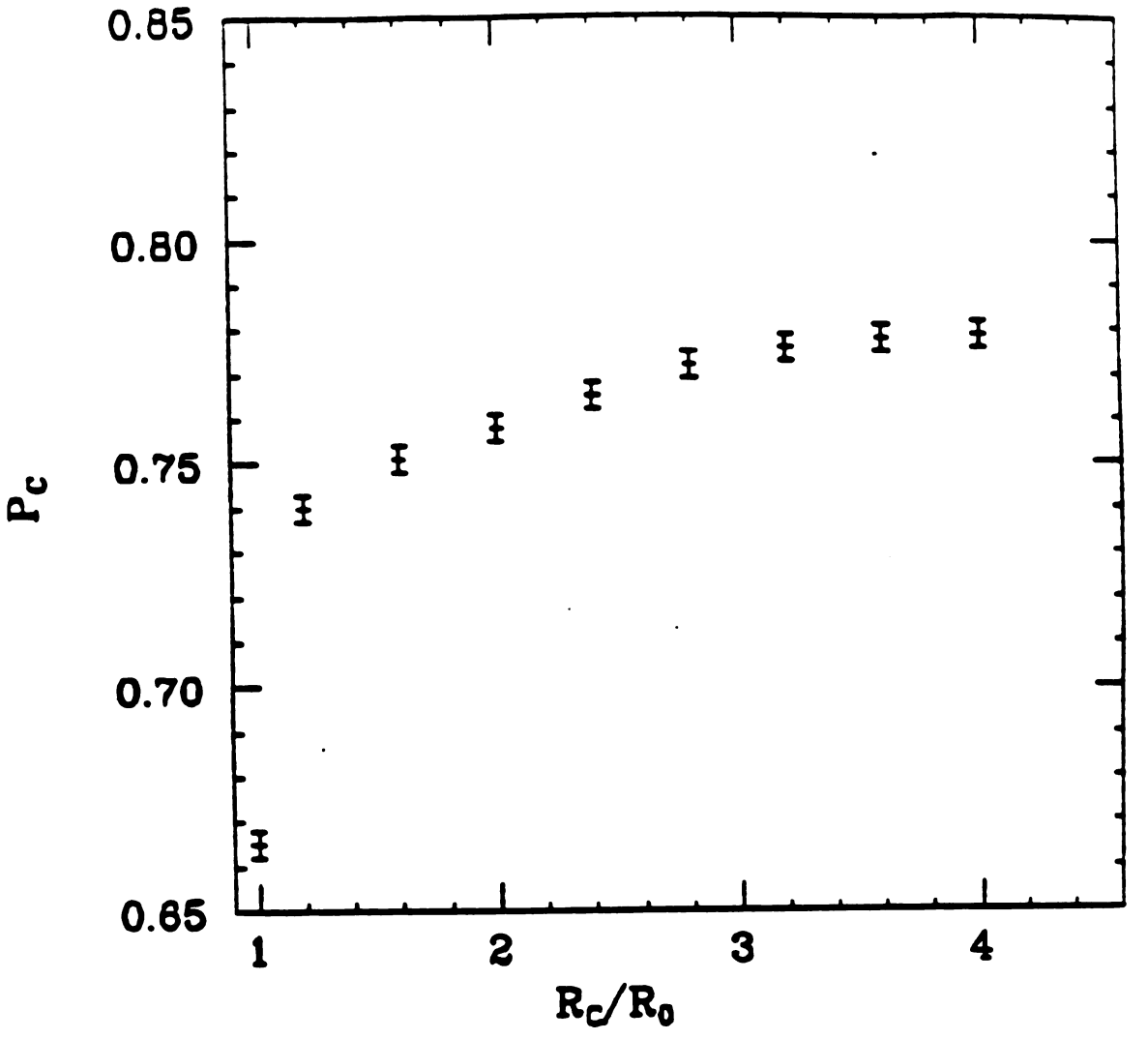

Figure 3.7: Percolation coverage as a function of R_c/R_0 for D=2 : Here the percolation coverage is calculated from averaging 200 samples at percolation for each point. It is also seen that as R_c/R_0 increases from 1, P_c has a big jump, but smaller than that in D=3.

examples of the D=2 morphology and in Figure 3.7 which presents $P_c(R_c/R_0)$

An important feature of the dependence of P_c on R_c/R_0, in both D=3 and D=2 (see Figures 3.5 and 3.7) is that there is a first order jump in P_c as $R_c/R_0 \rightarrow 1$. At $R_c/R_0=1.0-$, $P_c=0.676\pm0.002$ in both D=2 and D=3, while we find that $P_c(1.0+)=0.745\pm0.005$ (D=3) and $P_c(1.0+)=0.740\pm0.005$ (D=2). These non-analytic changes in P_c at $R_c/R_0=1.0$ are physically reasonable, because, as soon as $R_c/R_0>1$, all the droplets that are being ballistically deposited onto the surface will coalesce with any pre-existing droplet with which they overlap i.e. an infinite sequence of coalescence events occur in an infinite system. When $R_c/R_0=1.0-$ however, no coalescence at all occurs.

Since there is a jump singularity in P_c at $R_c/R_0=1.0$, we must consider whether the universality class of the percolation geometry is altered for all $R_c/R_0>1$. We have tested the universality class of the percolation problem at P_c in the ICM through calculating the cluster size distribution, and find that, in the medium size range, the distribution complies with the scaling law very well. Figure 3.8 shows the cluster size distribution at the percolation point. According to the scaling theory of percolation, the size distribution n_s near the percolation point has the scaling form:

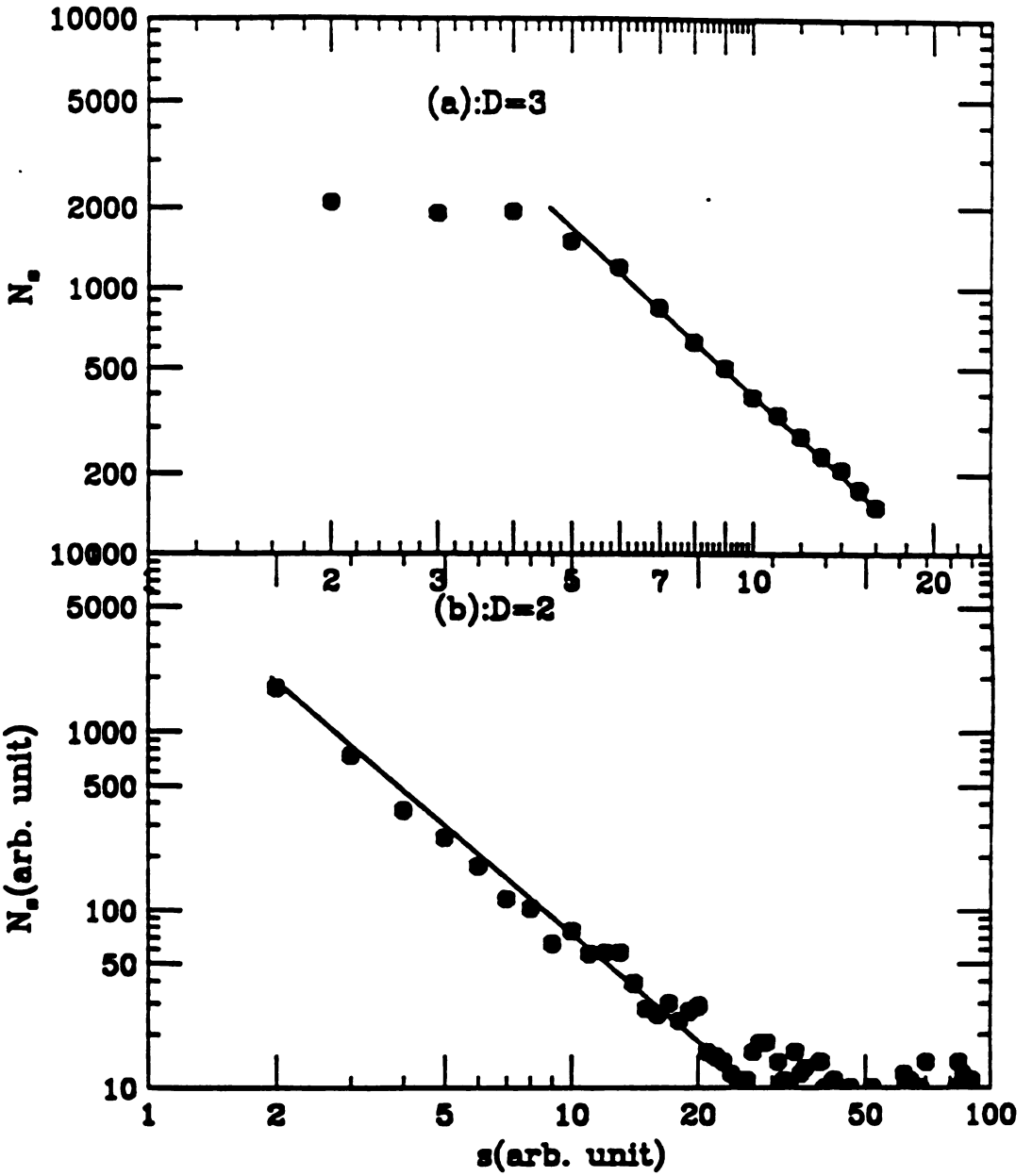

Figure 3.8: Cluster size distribution from ICM (a) D=3, In the medium size range, the log-log plot is nearly a straight line; both the small and large cluster size fall off the line significantly. When s is small, the scaling behavior fails; when s is too large the size effect has major influence on the scaling behavior.

$$n_s(p) = s^{-\tau} f[(p - p_c)s^{\sigma}] \qquad (3.2)$$

where τ and σ are critical exponents. The precise form of the scaling function f(x) has be to determined by computer experiments and other numerical methods. Other critical exponents are to be expressed using τ and σ. Here we omit the derivation and give the results only(Stauffer,1985):

$$\alpha = 2 - (\tau - 1)/\sigma \qquad (3.3a)$$

$$\beta = (\tau - 2)/\sigma \qquad (3.3b)$$

$$\gamma = (3 - \tau)/\sigma \qquad (3.3c)$$

τ is measured from the slope of a log-log plot of n_s, γ can be determined from the measurement of average cluster size. The values are listed in Table 3.1 which shows the comparison with conventional percolation results(Stauffer, 1985).

Table 3.1

	2d	2D on 2d	3D on 2d
α	-2/3	-0.71±0.08	-0.70±0.08
β	5/36	0.18±0.08	0.15±0.08
γ	43/18	2.35±0.04	2.40±0.04
τ	187/91	2.07±0.04	2.06±0.04
σ	36/91	0.39±0.04	0.39±0.04

It is seen that within a comfortable tolerance(less than 10%), the critical exponents in the ICM model are matched with the results from percolation theory. Therefore, the ICM

percolation process appears to remain in the same universality class as the uncorrelated case.

We note that the wormy structures of Figure 3.1 do not at first sight resemble the percolation structure of Figure 3.4b. The main reason for this is that sharp grooves occur at the intersection of the circles in Figure 3.4b, but do not occur in Figure 3.1. In a real film these grooves would round out to a radius of curvature R_c, producing the wormy appearance so characteristic of these films. Unfortunately, we have found no efficient method for simulating this rounding process in random continua shown in Figure 3.4b.

In summary, we have introduced a simple continuum model of film growth. Our model is an extension of one by Meakin and Family and includes a cross-over from an early island stage to a later wormlike stage. This model provides a natural explanation for the high P_c observed in many thin metal films grown on insulating substrates.

3.3 Substrate Inhomogeneity and Thin Film Morphology:

As stated in last section, in many film/substrate systems, the depositing material does not wet the substrate, so that in the initial stages of growth, distinct islands of the deposited material form (Volmer-Weber growth)(Pashley etc., 1964). As deposition continues, these distinct islands reach a critical size R_c(R_c-dependent on substrate

temperature T, deposition rate and anneal time amongst other things) at which they connect together to form a percolating structure, and further deposition soon leads to a continuous thin film. The case of layer by layer growth is the exception rather than the rule, as films may be rough either due to non-wetting, strain mismatch, due to kinetic roughening, or due to a combination of these processes. The early stages of film growth, and in particular the value of R_c are important in controlling the final morphology of polycrystalline films.

A detailed experimental study of the R_c dependence on deposition rate t and substrate temperature T for Pb has been performed on very smooth and clean amorphous SiO_2 substrates(Dubson and Jeffers 1994). To explain this data, a kinetic freezing model has been developed and provides a semi-quantitative explanation of the deposition rate and substrate temperature dependence of R_c. In the kinetic freezing model, it is considered that the complete coalescence time for two spherical droplets is proportional to the fourth power of radius, and thus the process of complete coalescence is overtaken by deposition. However, we also noted that the kinetic freezing model predicts a stronger than observed dependence of R_c on deposition rate (Jeffers etc., 1994), and suggested that this reduction in coalescence may be due to substrate inhomogeneity pinning

the islands in meta-stable states. Suppose that the surface energy is isotropic, the gain in surface energy in forming a compact shape from an elongated single crystal island scales as R^2, while it will be seen that the pinning energy scales as $R^{2/3}$. It would thus seem unlikely that pinning can produce metastability of elongated single crystal metal islands. In contrast, an elongated metal island containing one or more grain boundaries in its interior is easily pinned in a meta-stable state. The combination of grain boundaries and substrate inhomogeneity thus provides an important mechanism for strong substrate pinning effects on the growth morphology of polycrystalline films on non-wetting substrates.

Figure 3.9, gives experimental results for $T_c(R)$, the critical temperature below which no complete coalescence takes place at fixed deposition rate. It is obvious that $T_c(R)$ increases with R. The experimental data for the Pb/SiO_2 system is shown as the solid dots in Figure 3.9. Islands of size $R>R_c(T)$, touch and form a contact, but do not coalesce, and this region has been labeled sintering as it is similar to neck formation during the initial stage of sintering of granular aggregates. The dotted line is a schematic of experimental results on the bulk melting of lead, which has a size dependence $T_m(R) = T_m(\infty)(1 - c/R)$, where c is related to the densities and surface energies of the

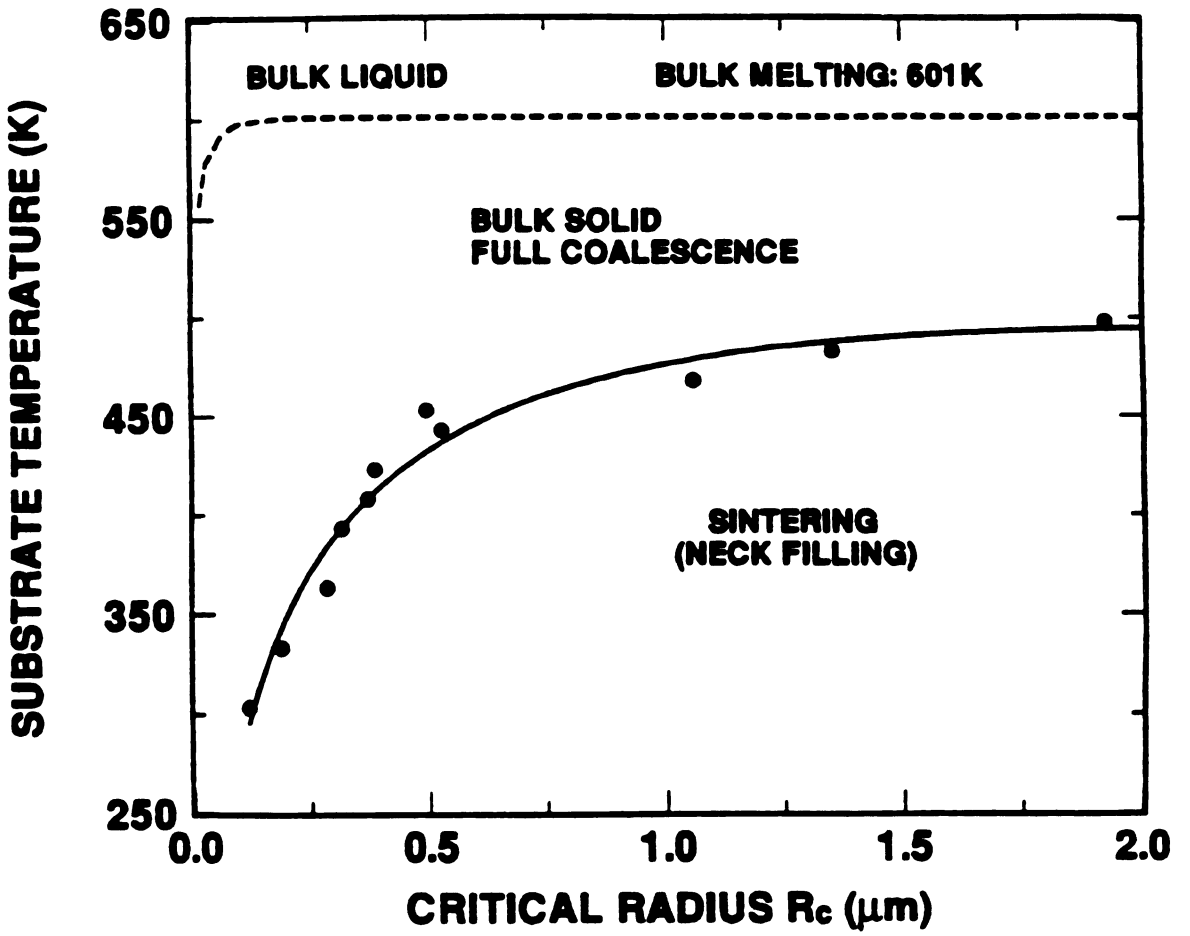

Figure 3.9: Experimental measurements for $T_c(R)$: The upper solid line is the size dependence of melting temperatures; the dotted line is the curve from experimental data; the area between them is the coalescence region, in which surface diffusion is the dominant factor for coalescence.

liquid and solid phases, and to the latent heat of the liquid-solid transition. Typically metal clusters have to be of radius of order 5nm before a significant (of order 10%) depression of bulk melting occurs(Buffat,1976). Between the bulk melting curve and the curve $T_c(R)$, there is a broad regime in which solid metal islands coalesce, predominantly by surface diffusion. In this regime, the island size distribution can be described by breath figure models. As the island size increases during growth, the film crosses the curve $R_c(T)$. At this point the metal islands do not fully coalesce into compact shapes, elongated metal islands are produced, and the film reaches the percolation point shortly afterwards.

Since the substrates we are considering are amorphous, separated metal islands grow with different crystallographic orientations. Thus when they first overlap, there is a grain boundary at their intersection. This grain boundary is eliminated during the coalescence process, as evidenced by the fact that for droplets $R<<R_c(T)$, each grain is a single crystal. However, when elongated metal islands first form, they usually contain a grain boundary in their interior, suggesting that grain boundaries play an important role in the energetics of coalescence.

When a grain boundary intersects the free surface of a solid, it forms a grain boundary groove. The equilibrium

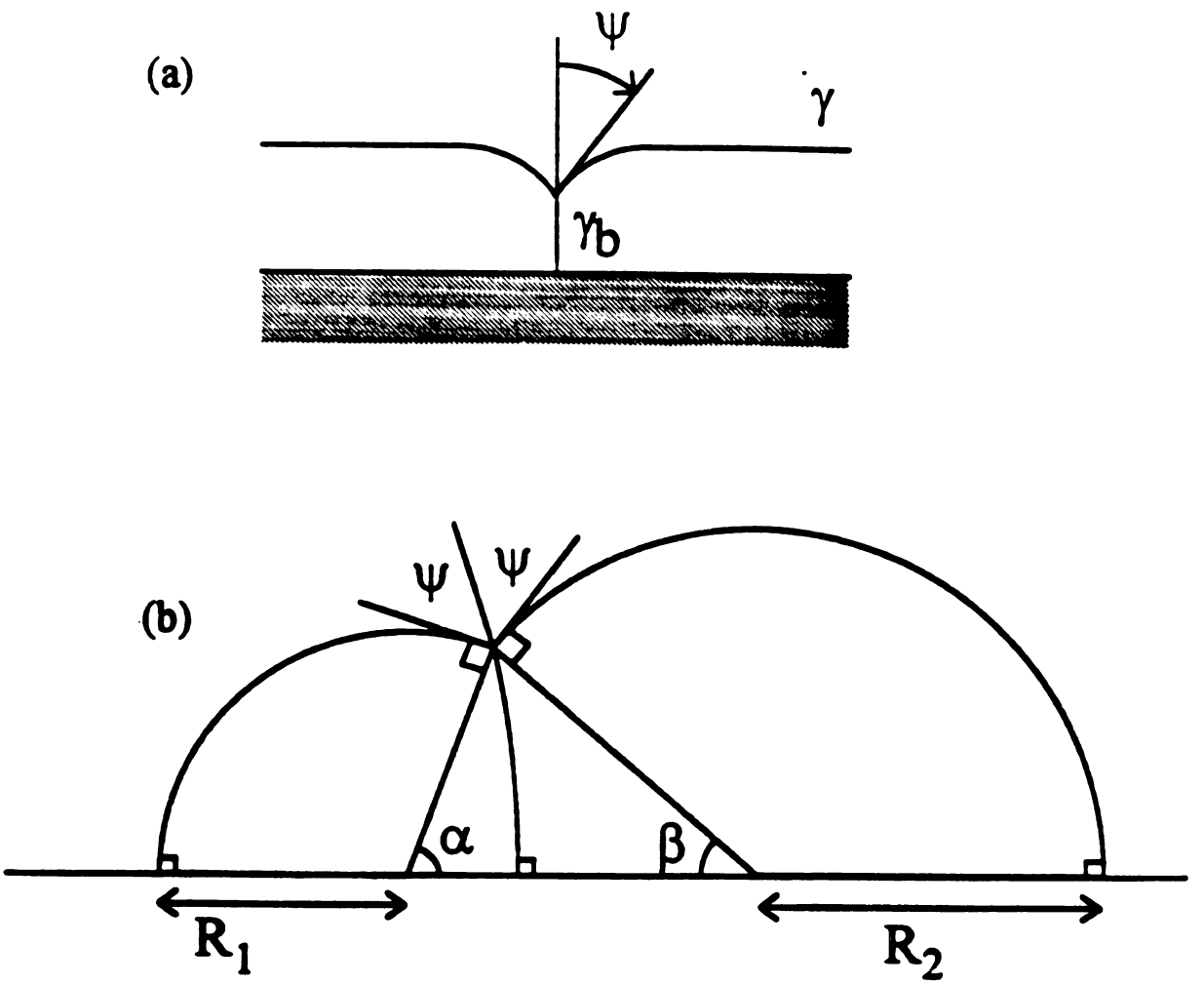

Figure 3.10: Two touched droplets with an interior grain bnoundary. The larger droplet has radius R_2 and the smaller has radius R_1. (a) showing the definiton of ψ (b) showing the definition of α and β.

grain boundary groove angle, ψ, is related to the surface energy of the metal, γ, and the grain boundary energy, γ_b. In the case of isotropic surface energies, the geometry is as depicted in Figure 3.10a, which leads to the expression,

$$\gamma_b = 2\gamma\cos\varphi \qquad (3.4)$$

For the purposes of illustration, we specialize to the case of the wetting angle $\theta=90^\circ$, and with the variables as defined in Figure 3.10, the sum of the surface and grain boundary energies is given by:

$$E = \pi\gamma[R_1^2(1+\cos\alpha)+R_2^2(1+\cos\beta)]+\pi\gamma_b R_b^2[1-\cos(\alpha-\psi)] \qquad (3.5)$$

where

$$R_b = R_1\sin\alpha/\sin(\alpha-\psi) \qquad (3.5a)$$

The angles α and β are as defined in Figure 3.10b. Here, we have used the fact that the grain boundary is a segment of the surface of a sphere, which bisects the groove at the triple point. It is assumed that the grain boundary energy is isotropic. Although the surface energy is certainly anisotropic, as evidenced by the anisotropic shape and significant flattening of parts of equilibrium crystals, this should not change our prediction for the scaling behavior of $T_c(R)$. In fact the only thing that is important for our argument to hold is that the presence of the grain boundary lead to unstable equilibrium of an elongated metal island. This feature should also be true for appropriately

chosen anisotropic equilibrium and non-equilibrium crystals shapes.

To ensure that the volume, V, of metal is conserved during coalescence, we impose the condition,

$$V = (\pi/6)[R_1^3(2+3\cos\alpha-\cos^3\alpha)+R_2^3(2+3\cos\beta-\cos^3\beta)] = const. \quad (3.6)$$

For $\theta<(90-\psi)$, the grain boundary groove tends to grow all the way down to the substrate(Millins,1957), and hence separate the elongated island into two single crystal grains. If $\theta>(90-\psi)$, there is a finite groove depth, and the energy by equation(3.2) is a monotonically decreasing function of the size of the larger metal island R_2(see Figure 3.11). In particular, when the two metal islands are nearly the same size $R_1/R_2 \approx 1$, there is a very small slope in the surface energy curve and hence the driving force toward coalescence is also very small. It ought to be pointed out that the small slope is due to the presence of the grain boundary. In the absence of a grain boundary, there is a steep slope in the analogous surface energy plot of elongated metal islands. Since the energy curve(Figure 3.11) is flat for nearly equi-sized islands, relatively weak contact line pinning, by for example surface irregularities or impurities, is able to prevent the metal islands from coalescing. Once a pair of islands is pinned in a meta-stable state, islands which are of similar or larger size, which attach to the pinned pair further stabilize the

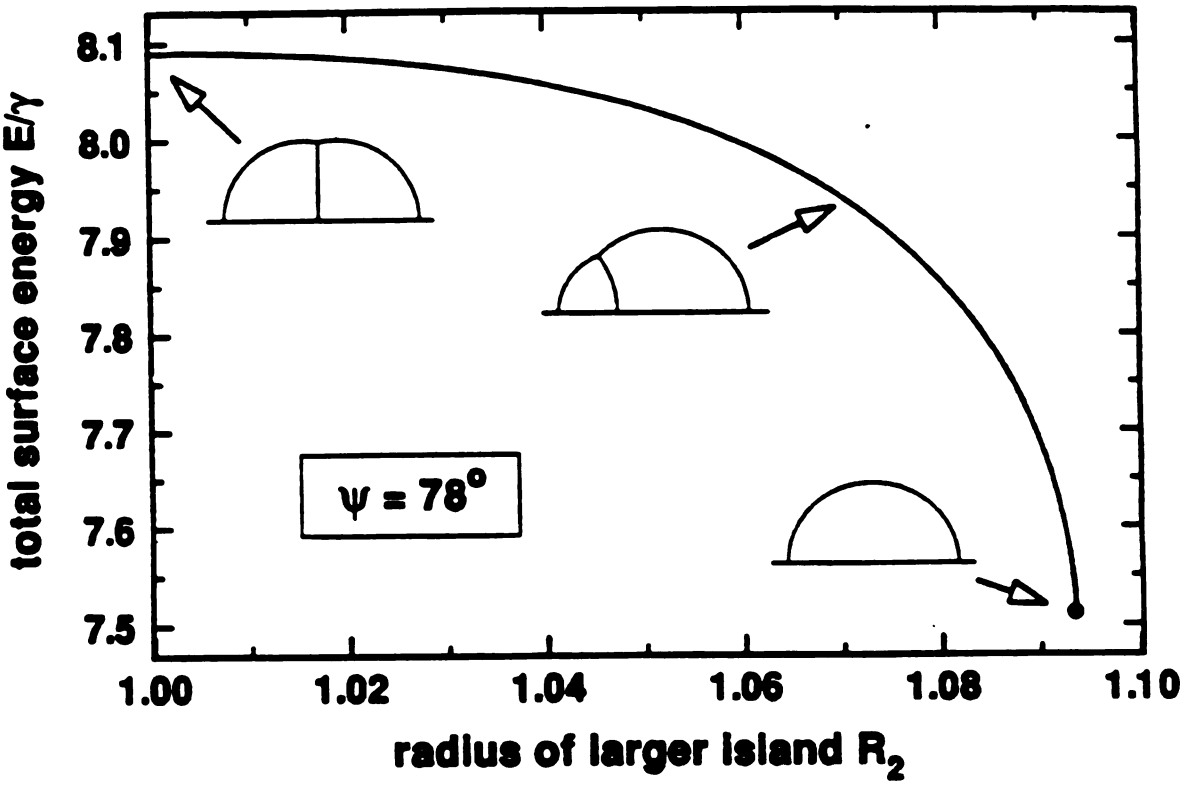

Figure 3.11: Surface energy as a function of the radius of the larger droplet R_2. We have taken R_1=1. When R_2 is close to 1, the surface energy is very flat, which means a small pinning force can stop the coalescence process.

structure. In this way, grains aggregate to form the percolation structure characteristic of the morphology of films grown on non-wetting substrates. Although the early coalescence stage does have a strong effect on film morphology, the large scale geometry at percolation is insensitive to this short range correlation, as expected from universality arguments.

We now concentrate on the case $\theta>(90-\psi)$ which is applicable to many metal/insulating substrate systems, where the wetting angle is typically quite large, but $90-\psi\sim10^0$ for high angle grain boundaries (where $\gamma_b\sim\gamma/3$). We develop a scaling argument to estimate the temperature at which thermal fluctuations can activate a pinned elongated metal island from a meta-stable state. We build on the analysis of contact angle hysteresis in fluid flow through capillaries (Joanny and de Gennes,1984). Here we calculate the energy due to the slight deformation $\eta(x)$ of a contact line. The surface profile of the liquid in the absence of bulk external field satisfies Laplace equation:

$$\frac{\partial^2 z}{\partial x^2}+\frac{\partial^2 z}{\partial y^2}=0 \qquad (3.7)$$

with the boundary condition that z vanishes on the contact line: $z(x,\eta(x))=0$. For $\eta(x)=0, z(x,y)=y\sin\theta$, which corresponds to the ideal case. The solution of equation (3.7) can be expressed as:

$$z(x,y) = y\sin\theta - \frac{\sin\theta}{\pi}\int_{-\infty}^{+\infty}\eta(x')\frac{y}{y^2+(x-x')^2}dx' \qquad (3.8)$$

The incremental energy due to the presence of η is expressed as

$$E_c = \frac{1}{2}\int dxdy\,\gamma[(\nabla z)^2 - (\sin\theta)^2] \qquad (3.9)$$

where γ is the surface tension of liquid. Inserting equation (3.8) into (3.9), and integrating over y, one has

$$E_c = \frac{\gamma\sin\theta}{d}\int_0^d dx\,\eta^2(x) \qquad (3.10)$$

Here 1/d is a low cutoff wavenumber. Defining

$$\eta^2 = \frac{1}{d}\int_0^d \eta^2(x)dx \qquad (3.11)$$

as the deformation magnitude, the energy increment becomes:

$$E_d = \frac{1}{2}k\eta^2 \qquad (3.12)$$

Where $k = \gamma\sin^2\theta$, independent of system size. Any deformation of the contact line will cost energy. In reality, the substrate is far away from perfect smoothness and homogeneity, therefore a deformation may be energetically favorable. Suppose the correlation length of random potential is smaller than the deformation size η, the energy gain is proportional to square root of deformed area $\sqrt{\eta L}$ (note that it is $\sqrt{\eta L}$ not ηL due to randomness)(Robbins and Joanny,1987) where L is the contact line length

$$E_h = -h\sqrt{\eta L} \qquad (3.13)$$

where h is constant depending on pinning strength and liquid surface tension. Thus the total energy change due to the slight deformation of contact line is:

$$E(\eta, L) = \frac{1}{2} k \eta^2 - h\sqrt{\eta L} \qquad (3.14)$$

The minimization of equation (3.14) gives the deformation magnitude

$$\eta_d \approx \left(\frac{Lh^2}{4k^2} \right)^{1/3} \qquad (3.15)$$

and the corresponding energy gain:

$$E_0(L) = -0.75h \left(\frac{h}{2k} \right)^{1/3} L^{2/3} \qquad (3.16)$$

while $L=2\pi R$, it thus follows that the pinning energy scales as $R^{2/3}$, as mentioned previously.

Although this argument was developed for liquids, it applies for solids provided a significant fraction of the exposed faces of the crystal are above their roughening temperature. If the temperature is sufficiently high, thermal fluctuations depin the contact line. We estimate the depinning transition by comparing the thermally induced contact line wandering with the disorder induced wall wandering of equation (3.15). To calculate the typical amplitude of thermal wall wandering, we consider the height-height correlation expression

$$G(r) = \langle [z(r)z(0)] \rangle \qquad (3.17)$$

The Hamiltonian related to the surface profile is roughly expressed as(Week,1980):

$$\delta H = \iint dxdy\left[\frac{1}{2}\gamma(\nabla z)^2\right] \qquad (3.18)$$

where γ is surface tension. From the Boltzmann distribution, the correlation function becomes:

$$G(r) = \langle [z(r)z(0)] \rangle = \frac{k_B T}{\gamma}\sum_q \frac{e^{iqr}}{q^2} \qquad (3.19)$$

Turning the sum over q into an integral and introducing a unit lower cutoff scale(lattice spacing), the thermal fluctuations leads to the wandering amplitude

$$\eta_T \approx (k_B T / 2\pi\gamma \ln R)^{1/2} / \sin\theta \qquad (3.20)$$

Equating η_T and η_d,

$$k_B T_c(R) \approx cR^{2/3} / \ln R \qquad (3.21)$$

with c given by,

$$c \approx 2\pi\gamma \sin\theta (\pi h^2 / 2k^2)^{2/3} \qquad (3.22)$$

Notice that k in equation (3.21) relates to γ and θ through $k = 2\gamma\sin\theta$, thus the coefficient c is inversely proportional to $(\sin\theta)^{-2/3}$. The smaller θ is, the more effective is the pinning, and hence the larger $T_c(R)$ is (of course this breaks down if $\theta > (90-\psi)$ is violated). As expected, larger h implies larger c, which leads to larger $T_c(R)$. These general conclusions hold even when more complex forms of thermal Hamiltonian are used, although the R dependence in equation (3.7) is clearly altered. Although based on several oversimplified assumptions, equations (3.20)-(3.22) provide a useful guide to the expected effect of substrate inhomogeneity on growth morphology.

So far, the experimental results are for Pb on very smooth and clean amorphous SiO_2, and even there, there are clear indications that both pinning and kinetic freezing effects are important in determining film morphology. It would be useful, although difficult, to develop a theory addressing the combined effect of kinetic freezing and substrate pinning. Another useful approach is to try to experimentally isolate these two effects by varying substrate roughness, substrate temperature and deposition rate. For sufficiently strong substrate disorder, it is probable that a strong pinning theory would be needed instead of the weak pinning result used here.

CHAPTER FOUR

MOLECULAR DYNAMICS STUDY OF METAL CLUSTERS

4.1 Methodology of Computer Simulations:

In this section, I will review some fundamentals of statistical mechanics and thermodynamics that are relevant to our analysis of computer simulations. We assume all particles are identical, have three spatial degrees of freedom, and obey classical mechanics defined by a total Hamiltonian $\mathcal{H}$. In the canonical ensemble, the number of particles N, the volume V and the temperature are held fixed. The motion state of the system is represented with generalized coordinates $\mathbf{r}=(\mathbf{r}_1,\ldots\mathbf{r}_N)$ and conjugate momenta $\mathbf{p}=(\mathbf{p}_1,\ldots\mathbf{p}_N)$. Generally, $\mathcal{H}$ is a function of $\mathbf{r}$ and $\mathbf{p}$. The probability density at $(\mathbf{r},\mathbf{p})$ in phase space is of the form

$$\mathcal{P}(N,V,T)=\frac{1}{N!h^{3N}Z(N,V,T)}\exp[-\beta\mathcal{H}(\mathbf{r},\mathbf{p})] \qquad (4.1a)$$

with

$$Z(N,V,T)=\frac{1}{N!h^{3N}}\iint d\mathbf{r}d\mathbf{p}\exp[-\beta\mathcal{H}(\mathbf{r},\mathbf{p})] \qquad (4.1b)$$

The fundamental relationship between statistical mechanics and thermodynamics is given by

$$\mathcal{F}(N,V,T)=-kT\ln Z(N,V,T) \qquad (4.2)$$

where $\mathcal{F}$ is Helmoltz free energy and is minimized at equilibrium. The Hamiltonian $\mathcal{H}$ is a sum of kinetic energy $\mathcal{T}(\mathbf{p})$ and potential energy $\mathcal{V}(\mathbf{r})$ for most systems we are

discussing: $\mathcal{H}=\mathcal{T}+\mathcal{V}$. Therefore, the momentum part of the partition function Z can be integrated out:

$$Z(N,V,T)=\frac{Q(N,V,T)}{N!\Lambda^{3N}} \tag{4.3}$$

where Q and Λ are given by:

$$Q=\int \exp[-\beta\mathcal{V}(\mathbf{r})]d\mathbf{r}$$

$$\Lambda=\left(\frac{2\pi mkT}{h^2}\right)^{1/2} \tag{4.3a}$$

The canonical average of a variable is given by:

$$\langle A\rangle=\int A\exp(-\beta\mathcal{H})/Z(N,V,T) \tag{4.4}$$

The average of $\mathcal{T}$ thus is easily obtained: $\langle\mathcal{T}\rangle=3NkT/2$. Molecular Dynamics simulation calculates the positions and velocities of particles in the systems from the Hamiltonian described above. The equations of motion of each particle comply with Newtonian Dynamics:

$$\frac{d\mathbf{r}_i}{dt}=\frac{\partial\mathcal{H}}{\partial\mathbf{p}_i}=\mathbf{p}_i/m \tag{4.5a}$$

$$\frac{d\mathbf{p}_i}{dt}=-\frac{\partial\mathcal{H}}{\partial\mathbf{r}_i}=-\frac{\partial\mathcal{V}}{\partial\mathbf{r}_i} \tag{4.5b}$$

In traditional molecular dynamics, the total energy E for a fixed number of atoms in a fixed volume V is conserved as the dynamics of system evolves in time, and the time average of any property is an approximate measurement of the microcanonical ensemble average of that property for a thermodynamic state of N,V,E. However, for certain applications, it may be desirable to perform dynamic simulations at constant temperature. Several artificial

inventions are used to achieve this goal and we will focus on the Extended System Molecular Dynamics(ESMD) approach (Nose,1984; Jellinek and Berry,1989; Anderson, H.C.,1980) which allows the system to thermally contact with a heat reservoir represented by an additional degree of freedom s. To realize the objective that the average kinetic energy is fixed at equilibrium, the Hamiltonian is postulated to be:

$$\mathcal{H} = \sum_i \mathbf{p}_i^2 / 2ms^2 + \mathcal{V}(\mathbf{r}_i) + p_s^2 / 2Q + gkT \ln s \qquad (4.6)$$

$\mathbf{p_s}$ is the conjugate momentum of s; Q is a parameter of the heat reservoir and behaves as a mass for the motion of s; kT has its regular meaning; it will be shown that g is essentially equal to the degree of freedom of the physical system. It is also assumed that the Hamiltonian equations of motion of r and s are valid:

$$\frac{d\mathbf{p}_i}{dt} = -\frac{\partial \mathcal{H}}{\partial \mathbf{r}_i} = -\frac{\partial \mathcal{V}}{\partial \mathbf{r}}$$
$$\frac{d\mathbf{r}_i}{dt} = \frac{\partial \mathcal{H}}{\partial \mathbf{p}_i} = \frac{\mathbf{p}_i}{m_i s^2} \qquad (4.7a)$$

and

$$\frac{dp_s}{dt} = -\frac{\partial \mathcal{H}}{\partial s} = \frac{1}{s}\left(\sum_i p_i^2 / m_i s^2 - gkT\right)$$
$$\frac{ds}{dt} = -\frac{\partial \mathcal{H}}{\partial p_s} = \frac{p_s}{Q} \qquad (4.7b)$$

It is easy to prove that $\mathcal{H}$ is conserved through combining equations (4.6) and (4.7). Therefore, the micro-ensemble partition function can be expressed as:

$$Z = \int dp_s \int ds \int d\mathbf{p} \int d\mathbf{r} \times \delta[\mathcal{H} - E] \qquad (4.8)$$

where E is total energy. If we use p'=p/s, r'=r, and set g=3N+1, the degree of freedom of the system, Z yields the following expression after integration over p_s and s:

$$Z = C \iint dp' dr' \exp[-\beta(\mathcal{T} + \mathcal{V})] \qquad (4.9)$$

where C is a constant. This is exactly the canonical ensemble partition function. The MD simulation is to solve the equations of motion (4.7) for appropriate initial conditions.

4.2 Many-body Interaction in a Metal:

One very important aspect of molecular dynamics simulation is to have a good potential describing the interactions of atoms in the system. The Lennard-Jones potential is famous and successful when applied to rare gases, e.g. Ar and Xe. But it fails to predict and explain many experimental data of metals, especially the noble and transition metals. For instance, the Cauchy relation of the elastic constants $C_{12}/C_{44}=1$(Landau,1984) is valid for any pairwise central potential, of course including the Lennard-Jones(LJ) potential while the experimental data for this ratio is much higher: 3.7 for gold and 1.5-3.3 for transition metals(Ercolessi etc.,1988). Another failure of the LJ potential and other two-body interactions is that they predict the cohesive energy E_c, the energy needed to

remove an atom from the bulk lattice is essentially equal to the vacancy formation energy E_v; while the experimental data show that E_v/E_c=0.25 for gold and about 0.35 for transition metals. In a two-body system, the melting temperature is usually near $0.1E_c$; in gold, on the other hand $T_m \sim 0.03E_c / k_B$. Some of those problems may be cured by adding new terms which depend on the total volume of the system in the potential. Therefore, it is clear that, to describe metals, an adequate model must include many body contributions.

In metals, the conducting electrons are loose and their collective Coulomb interaction with ions is the force which maitains the lattice structure. For transition and noble metals, the conduction electrons are d-electrons and d-electrons. Generally the s-electrons form a very broad energy band which overlaps with the narrower s-electron band. The following calculation based upon the work by J.Friedel(Friedel, 1969) and Gupta(Gupta, 1981) is to sketch an interaction form starting from the tight binding model. First, one considers d-electrons which have 10 atomic states. For the sake of simplicity, the density of states is represented by a rectangular function of width W and height 10/W. The Fermi energy E_F for a metal with number Z of d-electrons is related to the bandwidth through:

$$E_F = W(Z-5)/10 \qquad (4.10)$$

The zero energy is at the center of the band. The cohesive energy E_d from the d electrons is given by:

$$E_d = \int_{-W/2}^{E_F} E\rho(E)dE \qquad (4.11)$$

where $\rho(E)$, the density of state has been assumed to be constant. The integral then gives:

$$E_d = \frac{W}{20} Z(10-Z) \qquad (4.12)$$

In the tight-binding model, the bandwidth W is determined by the overlap integrals. The second moment of $\rho(E)$:

$$\mu_2 = \frac{1}{10} \int_{-W/2}^{W/2} E^2 \rho(E)dE = \frac{1}{6} W^2 \qquad (4.13)$$

On the other hand, μ_2 can be expressed as:

$$\mu_2 = \sum_{\mathbf{k}} \langle \mathbf{k}|(H-E_0)^2|\mathbf{k}\rangle \qquad (4.14)$$

where H is Hamiltonian of the d-electrons and E_0, the atomic energy level at a selected site i can be taken to zero. **k** labels the Block wavevectors. μ_2 is expressed in real space, reading:

$$\mu_2 = \langle i|H^2|i\rangle = \sum_j |\langle i|H|j\rangle|^2 \qquad (4.15)$$

where |i> denotes an atomic wavefunction of a d-electron at site i. If only nearest neighbor overlap is taken into account,

$$\mu_2 = \sum_{j \neq i} \beta^2(r_{ij}) \qquad (4.16)$$

Here $\beta(r_{ij})$ is the hopping integral and r_{ij} is the distance

between sites i and j. Combining all these equations and eliminating W, one obtains:

$$E_d = C\left[\sum_{j\neq i}\beta^2(r_{ij})\right]^{1/2} \qquad (4.17)$$

with $C=\left(\sqrt{6}/20\right)Z(10-Z)$. The hopping integral can be taken to be of exponential form:

$$\beta(r)=\beta_0 e^{-q(r-a)} \qquad (4.18)$$

where *a* is the bulk interatomic separation at equilibrium. The equation above gives the d-band contribution to the cohesive energy. The stability of the lattice requires that there be a countervailing short range repulsive force, which is provided by the compression of the free electron gas, in the model, the s electrons. As the atoms are brought together to form a solid, the free electron contribution to the cohesive energy is at first attractive since the valence charge density is expelled into a region of more attractive potential. However as the interatomic separation is further decreased, the potential reaches its minimum and the repulsive force begins to dominate. According to this picture, the short range repulsive force can be written as:

$$E_s = B\sum_{j\neq i} e^{-p(r_{ij}-a)} \qquad (4.19)$$

and the parameter p characterizes the interaction range. The total energy $E_c=E_d+E_s$ ought to be minimized at r=a. Consequently, the following expression can be obtained:

$$E_c = \frac{1}{2}V_0\left[\left(\sum_{j\neq i}\exp[-2q(r_{ij}-a)]\right)^{1/2} - \frac{q}{p\sqrt{z}}\sum_{j\neq i}\exp[-p(r_{ij}-a)]\right] \quad (4.20)$$

where z is the number of nearest neighbors. For a specific metal, the parameters p, q, and V_0 can be determined by experiments. While doing computer simulations, one just needs the reduced expressions and any quantity in the final results can be converted into real units by dimensional analysis. To do that, we set a=1, V_0=1, thus the total energy of a metal system with N atoms can be written as:

$$V = -\frac{1}{2}\sum_{i}^{N}\left[\left(\sum_{j\neq i}e^{-2q(r_{ij}-1)}\right)^{1/2} - A\sum_{j\neq i}e^{-p(r_{ij}-1)}\right] \quad (4.21)$$

where $A = q/p\sqrt{z}$. This energy form cannot be modeled by pairwise forces because a two-body scheme implies a linear dependence of energy of an atom upon its coordination; Because of the presence of the square root term in the expression, the energy is nonlinearly dependent on its coordination. The potential has been used by many authors (Bulgac,1992; Garson and Jellinek,1992) and proved to be able to describe the bulk and surface properties of a variety of metals well. Next, I will apply the potential to gold clusters and study their equilibrium and dynamic properties.

4.3 The Solid-liquid Phase Transition

The notion that small clusters might exhibit distinguishable solid-like and liquid-like phases arose from classical isoenergetic molecular dynamics(MD) simulations of the 1970's(Briant and Burton,1975), largely of Argon represented by pairwise Lennard-Jones interaction. Results of simulations indicated clearly that solid-like behavior could be anticipated at sufficiently low energies and that liquid-like behavior would appear at high energies(Berry, 1987; Jellinek etc.,1986). The typical curve of the temperature versus energy is shown in Figure 4.1. This type of behavior appeared for clusters with N>6 and was interpreted as indicative of a first-order phase transition. More recently, different potentials describing various systems such as metal and carbon clusters have produced similar results. The striking evidences of those simulations inevitably raised the question of what the physical basis is for the existence of solid and liquid phases in finite systems, especially small clusters. The following argument based on the thermodynamic point of view shows that it is possible for small clusters to have a fairly sharp solid-liquid phase transition. A solid-like phase can be intuitively identified with a state of rigidity and liquid-like phase with a state of floppiness. Hypothetically, suppose an exact Hamiltonian describing a cluster could be

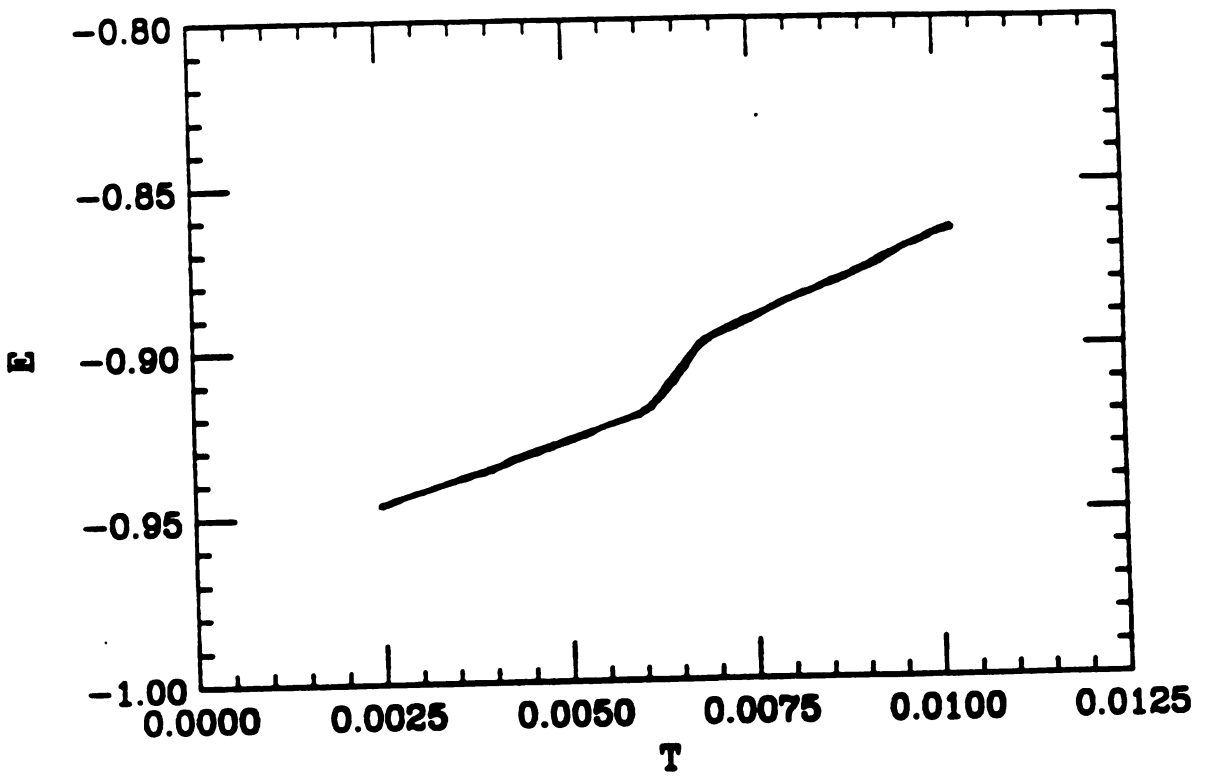

Figure 4.1: A solid-liquid phase transition schematic plot: total energy v.s. temperature: The calculation was done for cluster N=13 using both constant temperature and constant energy molecular dynamics. The two method yields the same result. The solid-liquid phase transition is signified by the presence of a twist region on the curve.

solved, one would have the exact statistical properties of the cluster and then one would know the cause of the phase transition. In a theoretical study, most clusters are customarily described by effective Hamiltonians that are approximate in two ways. They are based on the adiabatic or Born-Oppenheimer approximation which supposes separability of the slow nuclear from fast electronic motion, and on the assumption that the amplitudes of vibration are small compared with the interatomic distances, the frequencies are high compared with rotational frequencies and the moments of initia are therefore nearly constant. The energy levels of a cluster with the above approximation are described as the electronic excitations plus vibrational spectra which are surrounded by more detailed rotational energies. The density of states D(E) of a system in such a rigid phase is higher than in a floppy phase in the lowest range of energies. The densities of states of both the solid-like and liquid-like limits increase with energy, but D(E) of the liquid increases much faster so that at sufficiently high energies, the density of states of the liquid-like form becomes much larger than that of the solid-like form. Here we introduce an order parameter-like quantity ϕ to represent the floppiness of a cluster, when $\phi=1$ the cluster is in the completely floppy state while $\phi=0$ is the limit for the solid-like phase. Consequently, at low energies, the

partition function $Z(T,\phi)$ mainly has a contribution from low energy states and thus is a decreasing function of ϕ. On the other hand, at high energies, $Z(T,\phi)$ is an increasing function of ϕ. The free energy $F(T,\phi)$ has only one minimum at $\phi=0$ at low temperatures and one minimum $\phi=1$ at high temperatures. As the temperature is raised from the low energy where only the solid is stable, $D(E)$ near $\phi=1$ increases faster than that near $\phi=0$, so that $Z(T,0)$ increases slower with T than $Z(T,1)$, and then $F(T,0)$ decreases slower with T than $F(T,1)$. As T increases, it reaches a value T_f at which the free energy $F(T,\phi)$ develops a slope of zero at some value of ϕ at or near 1; that is $\partial F(T,\phi)/\partial\phi|_{T=T_f}=0$. At temperatures above T_f, $F(T,\phi)$ has two minima. As T increases still further, it reaches a value T_{eq} for which the free energies at the two minima are equal. Because $F(T,\phi)$ becomes monotonically decreasing at sufficiently high T, and is a smooth function of both T and ϕ, there must be a temperature T_h at which the minimum near $\phi=0$ turns into a point of zero slope; above T_h only the liquid-like form is thermodynamically stable. Figure 4.2 schematically shows how $F(T,\phi)$ changes with T and ϕ. So far, we have used the properties of the densities of states to argue about how the free energy of a system changes as temperature increases. It should be pointed out that, in general, the range $T_f<T<T_h$ is the transition region. In the

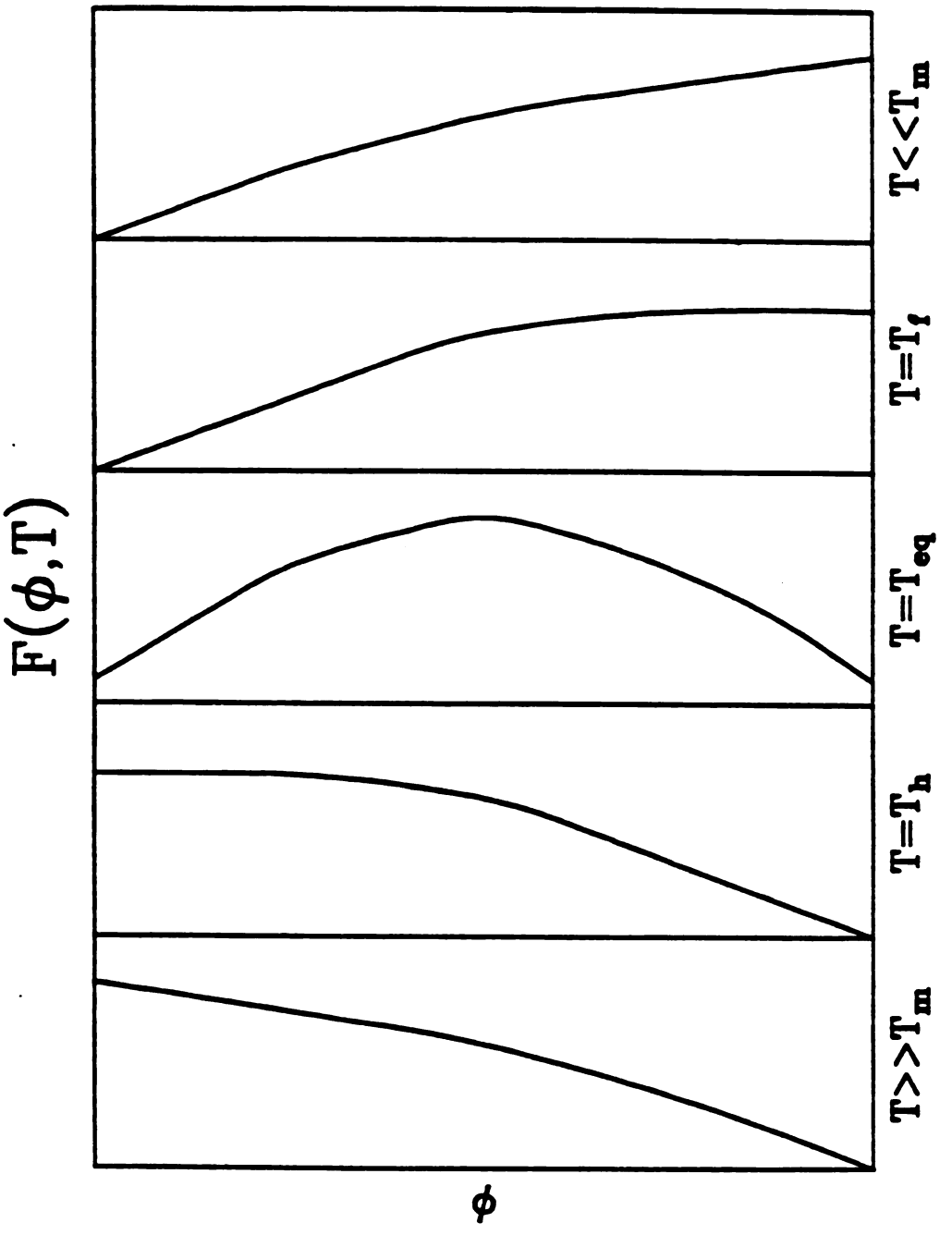

Figure 4.2: A schematic plot of free energy F as a function of floppiness ϕ at changing temperature. At low temperatures, F has only one minimum at ϕ=0, the solid state; at $T=T_f$, F is flat at ϕ =1; when further increasing T, F have two minima at ϕ=0 and ϕ =1; at T=Teq, the values at those two points are equal, which is coexisting phase; at $T=T_h$, F has only one minimum at ϕ=1, the liquid state, but F is flat near ϕ=0; At high temperatures, F has one minimum.

following discussion, the transition temperature(melting temperature) is defined from our MD calculation results.

Both experimental data and simulations show that the melting temperature T_m is dependent on cluster size N. The experimental data are summarized in Figure 4.3 for Gold (Buffat and Borel,1976; Borel,1981). The dots represent the experimental data and the solid curve is the fitting function which is of the following empirical expression:

$$T_m = T_m(\infty)\left(1-\frac{r_c}{r}\right) \qquad (4.22)$$

where the bulk melting temperature, $T_m(\infty)$=1338K for gold. The following argument presents a verification of the above relationship from the thermodynamic point of view .

Consider a solid gold spherical particle of radius r. Its total free energy includes the surface term and bulk term, reading: $F_s = M\mu + A\gamma$. M and A are total mass and surface area respectively. γ and μ are surface tension and chemical potential. Suppose the same amount of gold is in the liquid state, the free energy is rewritten as: $F_l = M\mu' + A'\gamma'$ Notice that the total mass remains unchanged while the surface area is altered because of the density difference of liquid and solid gold. At the melting temperature T_m, $F_s = F_l$, which leads to $M(\mu-\mu') = A\gamma - A'\gamma'$. Assume that T_m is not very far away from the bulk melting temperature $T_m(\infty)$, μ could be expanded and $\mu(T_m) - \mu'(T_m) = \mu_s - \mu_l - \Delta T(S_s - S_l)$ where $\mu_l = \mu_s$ at $T_m(\infty)$ and S is the

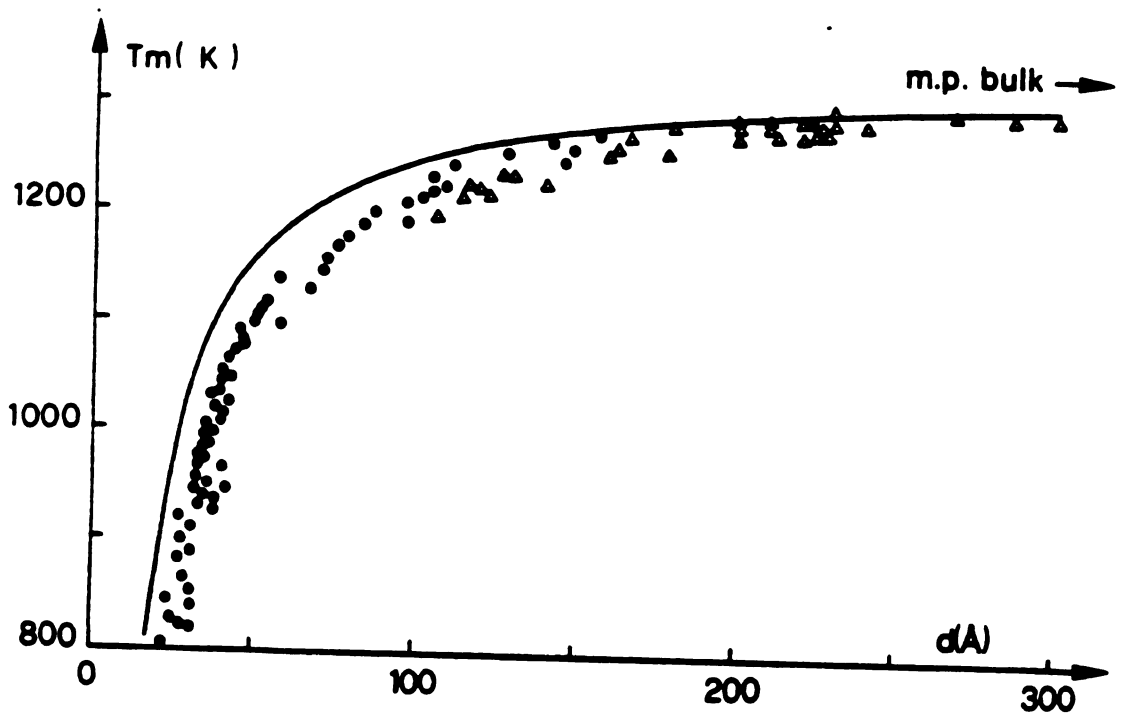

Figure 4.3: Experimental data of $T_m(r)$: the solid dots and triangles denotes experimental data while the solid curve is the semi-emperical fit to those data and has the analytical form expressed by equation (4.22).

entropy of unit mass. $S_s - S_l = -L/T_m(\infty)$ at the bulk melting, where L is latent heat of unit mass. $\Delta T = T_m(\infty) - T_m$. The geometry of liquid and solid sphere has the following relation:

$$\frac{A\gamma - A'\gamma'}{M} = \frac{4\pi(r_s^2\gamma - r_l^2\gamma')}{\rho_s 4\pi r_s^3/3} = \frac{3}{r_s\rho_s}\left[\gamma - \gamma'\left(\frac{\rho_s}{\rho_l}\right)^{2/3}\right] \qquad (4.23)$$

Combining all these equations, one has:

$$\frac{\Delta T}{T_m(\infty)} = \frac{3}{r\rho L}\left[\gamma - \gamma'\left(\frac{\rho}{\rho_l}\right)^{2/3}\right] \qquad (4.24)$$

Here we have dropped the subscript of solid. The equation is consistent with the empirical result equation (4.22) with r_c given by $r_c = (3/\rho L)[\gamma - \gamma'(\rho/\rho_l)^{2/3}]$.

To verify the occurrence of a phase transition utilizing MD simulation, we studied the caloric curve i.e. the relationship between the internal energy E and the temperature T which is proportional to the average of the kinetic energy. In the ESMD(extended system molecular dynamics) simulation T is an input parameter. Any computer simulation is a speed and accuracy trade-off. The minimum requirement for MD simulation is to satisfy the conservation laws(total momentum, total angular momentum and total energy) in the predefined tolerance ranges. The computer program is printed out in Appendix A in which we utilized the predictor-corrector algorithm to solve equation (4.7). The first step of the MD simulation is to choose the atom-atom interaction. The potential we have used in describing

gold clusters is equation (4.20) discussed in section 4.2. The parameters for gold are a=0.288nm, V_0=3.81eV, p=10.15 and q=4.13. In addition, the mass of the atom has been taken to be one so that the force on an atom is equal to the acceleration at that time. The conversion from a reduced unit to real time unit is summarized in Table 4.1:

Table 4.1

conversion	red. unit	real unit
time t	1.0	2.12×10^{-13}s
length a	1.0	0.288nm
energy E	1.0	3.81eV
temperature T	0.01	441K

The time step δt has been chosen from 0.002 to 0.02, depending on the temperature; high temperatures require small time steps and low temperatures could have relatively large δt for the same accuracy requirement. But in our calculations δt never exceeds 0.02 in reduced units, which secures the deviation of total Hamiltonian H in equation(4.6) within 10^{-4}. The caloric curves are obtained for four different cluster sizes: N=55, 177, 381, 725 which roughly corresponds to spheres of radii r=2,3,4,5 respectively. The initial conditions have been set to be of total zero momentum and angular momentum, preventing clusters from drifting or rotating. Clusters are set in a vacuum(free boundary) and low temperature environment at the

beginning. To observe the correct equilibrium quantities, the system must reach equilibrium before any quantity is measured. To achieve that, the system is run about 10,000 (0.1ns) time steps and a set of physical quantities(typically internal energy E and kinetic energy K) are attained. A subsequent 10,000 time steps are taken to compare statistical results of those quantities with previous ones. Typically 10,000-100,000(1ns) time steps are entailed for the system to reach equilibrium. The total internal energy E is calculated from averaging over another 100,000 time steps. The results are illustrated in Figure 4.4. Each curve has a sharp increment in E as temperature increases past a certain value as indicated in the figure. It is very noticeable that the increment in E and the temperature indicated in Figure 4.4 become greater as system size increases. A more obvious definition of the transition temperature is from the specific heat curves $C_v(T)$ that are easily found from the caloric curves(Figure 4.4a). Each curve of $C_v(T)$ has a maximum defined as the melting temperature T_m which moves to the right as N, the system size increases. Also the peak of C_v sharpens and approaches to the bulk limit where C_v diverges at melting. Figure 4.5 is plotted to compare the relationship of T_m and size in the simulation with experimental data in Figure 4.3, and gives good agreement.

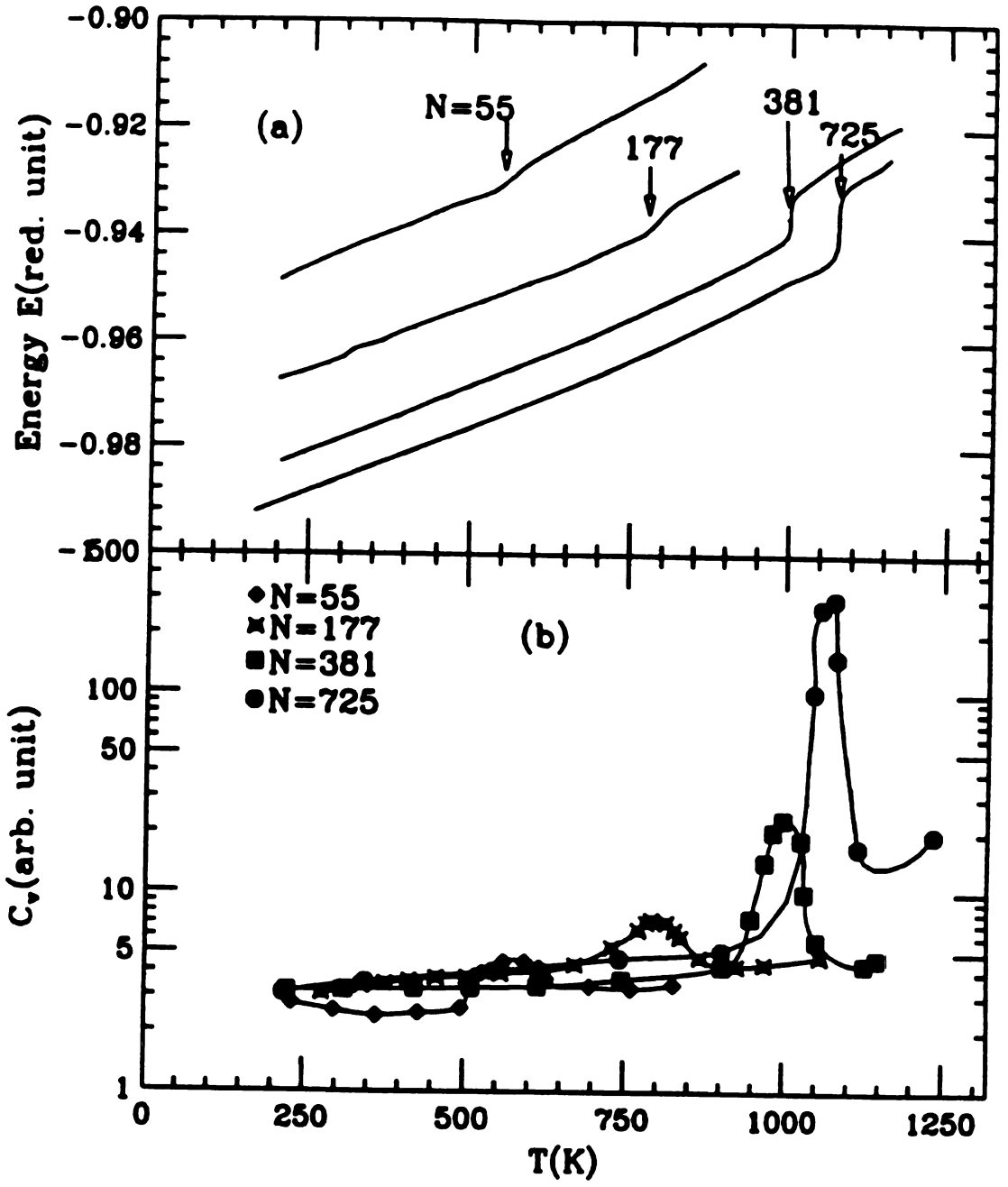

Figure 4.4: Caloric curves for clusters N=55, 177, 381 and 725. In each curve, the transition point is indicated (a) E v.s. T (b) C_v v.s. T: The melting temperature is defined as the temperature at which C_v reaches maximum.

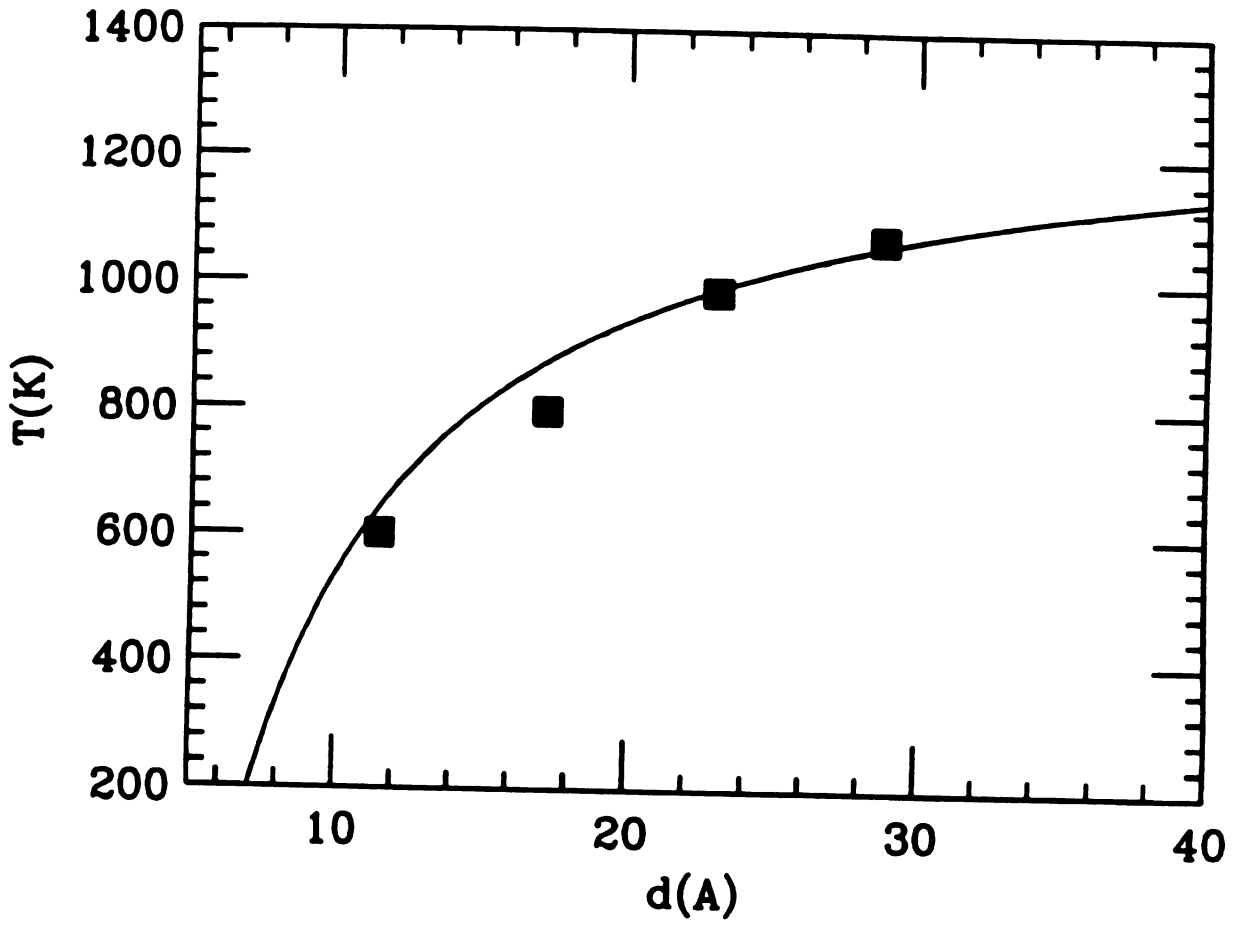

Figure 4.5: $T_m(r)$ from MD calculation: the four points are for the melting temperatures of clusters N=55, 177, 381, 725. The soilid line is a theoretical fit from equation (4.22).

An alternative criteria for the phase transition is to look at the mean square displacement(m.s.d.) as a function of simulation time t because atoms in the liquid show adiffusive behavior while atoms in the solid do not. The m.s.d. is defined as:

$$(\delta d)^2 = \frac{1}{N}\sum_{i}^{N}\left[\mathbf{r}_i(t+T_i) - \mathbf{r}_i(T_i)\right]^2 \qquad (4.25)$$

$\mathbf{r}_i(t)$ is position of atom i at time t. In calculating δd, the system reaches equilibrium first and the position of each atom at time T_i is recorded as the initial condition and results for an additional time t is used to calculate $(\delta d)^2(t)$. t is fixed while T_i is arbitrarily chosen from different values so that $(\delta d)^2$ is obtained from averaging over various configurations. In our calculations, typical data is averaged over 100 configurations and t is 10,000 time steps. The simulation is focused on the N=725 cluster first. Figure 4.6 gives $(\delta d)^2$ as a function of t at various temperatures. The picture shows that $(\delta d)^2$ versus t has different behavior at low temperatures from high temperatures. At low temperature, $(\delta d)^2$ is small and independent of simulation time t and increases monotonically with temperatures; at sufficiently high temperatures, $(\delta d)^2$ is of roughly linear dependence on t and δd has magnitude of order of distance between atoms. The small T behavior is due to the oscillation of an individual atom near its

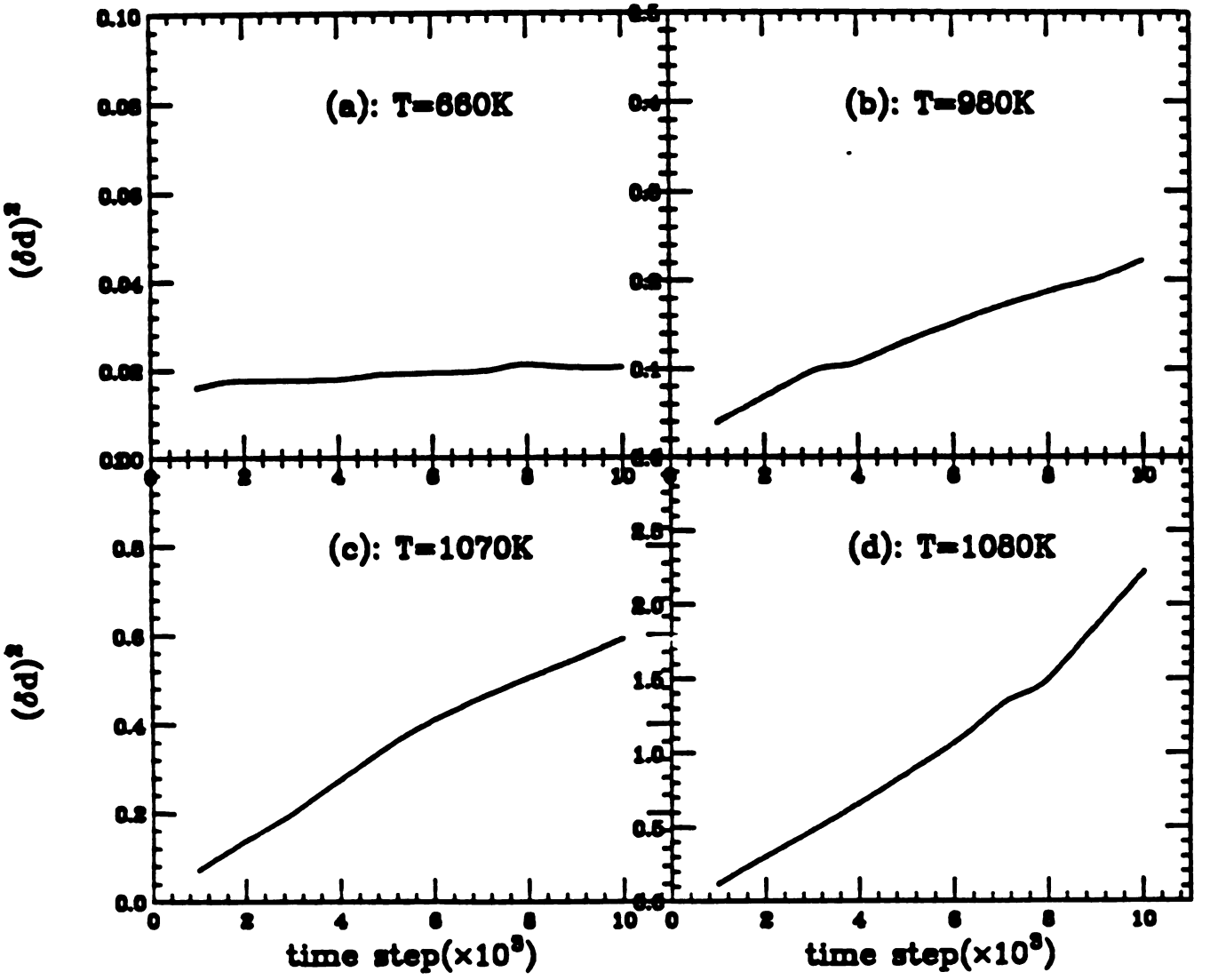

Figure 4.6: Mean square displacement $(\delta d)^2$ at various temperatures for the cluster N=725. At low temperatures, $(\delta d)^2$ is small and independent of time. As temperature increases, $(\delta d)^2$ increases in magnitiude and also has a linear dependence on simulation time t, showing diffusion behavior.

equilibrium position. The potential energy deviation δV from the ground state is approximately proportional to $(\delta d)^2$ from the harmonic approximation. The thermal average of kinetic energy is roughly equal to that of δV, therefore $(\delta d)^2$ is approximately proportional to temperature T. The high temperature properties of the cluster are a consequence of atomic diffusion. High T allows structural changes which create vacancies in the cluster and activates energetic atoms to move into those vacancies. To quantify, the diffusion constant is approximately measured from the slope of $(\delta d)^2(t)$. The temperature dependence of D is shown in Figure 4.7. In the figure, D is zero or immeasurable at very small T. There is a large change in D at the melting temperature T_m. But it is also very remarkable that D has non-zero values even at temperature well below T_m. This implies the presence of diffusion in the solid-like phase, a seeming contradiction with conventional wisdom. T_m for cluster N=725 is roughly 0.0243(1070K) while the temperature T_s at which observable diffusion phenomena occurs is about 800K. This phenomena was not observed for clusters with periodic boundaries and therefore, one has to look into the detail of surface atoms. Surface atoms are less bonded and easier to activate than bulk ones. We need to calculate mean square displacements of bulk and surface atoms separately. It is impossible to define a complete surface atom because

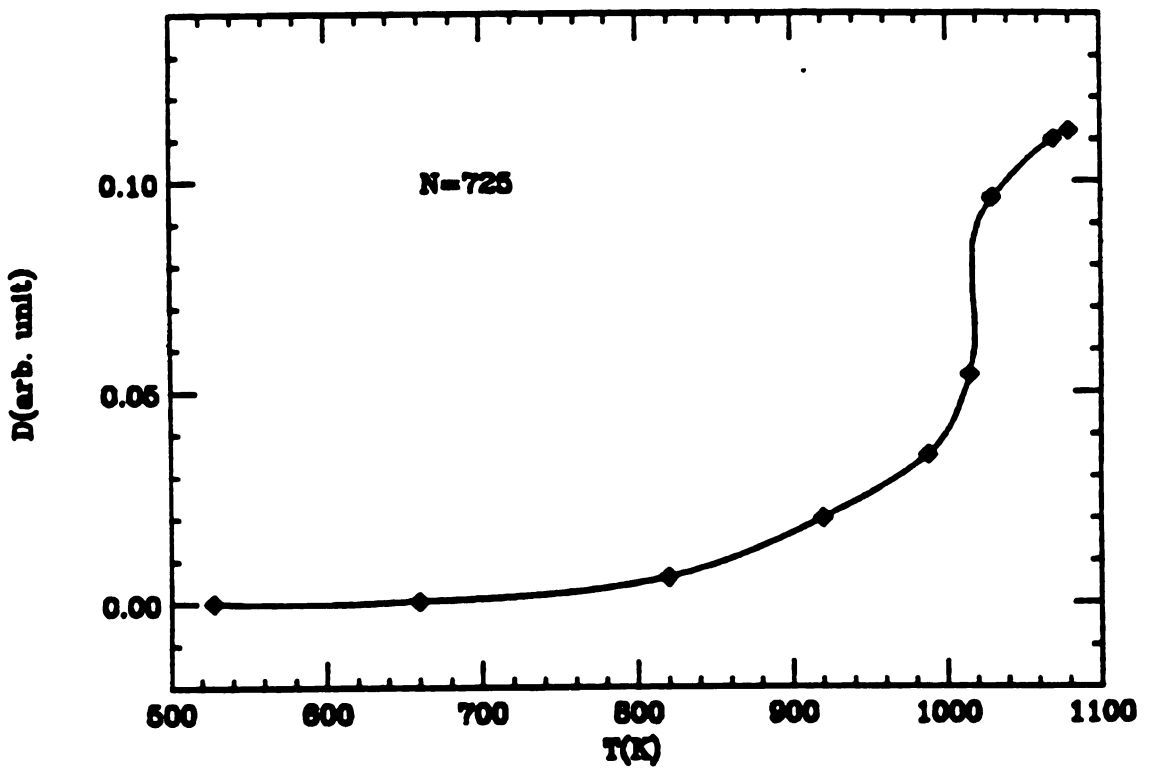

Figure 4.7: Diffusion constant D as a function of temperature T. At low T, the diffusion is absent D=0; there exists a big change in D at $T=T_m$; it is also remarkable that $D\neq 0$ for $T<T_m$.

it has a certain probability to be embedded in the bulk at certain time. But it is unambiguous to define a group of bulk atoms in the center of the cluster at low temperature since the time needed for those atoms to move to the surface is much longer than our simulation time. Therefore, in defining the bulk atoms, the position of center of mass of a cluster is calculated first and then the distance of each atom to the center. A threshold value of distance is set to identify the bulk and surface atoms. Atoms within the range are called bulk atoms and those outside of the range are surface atoms. Using the same technique, we repeated the calculation of δd but treated the bulk atoms and the surface separately. The comparison is made at different temperatures(Figure 4.8). At very low T(less than 700K), δd for the bulk atoms is similar to that of the rest and independent of time t but has a lower value. At a medium range of T (800K<T<1000K), $(\delta d)^2$ for bulk is still independent of t but $(\delta d)^2$ for the rest exhibits diffusive behavior, i.e. roughly proportional to t. It is clear now that in this temperature range, diffusion does not exist for bulk atoms but does appear to the rest of the atoms including surface atoms. At high temperatures(T>1100K), the bulk atoms and the rest do not act differently because then it is meaningless to define the bulk atoms and surface atoms as each atom diffuses around the cluster. Again from the

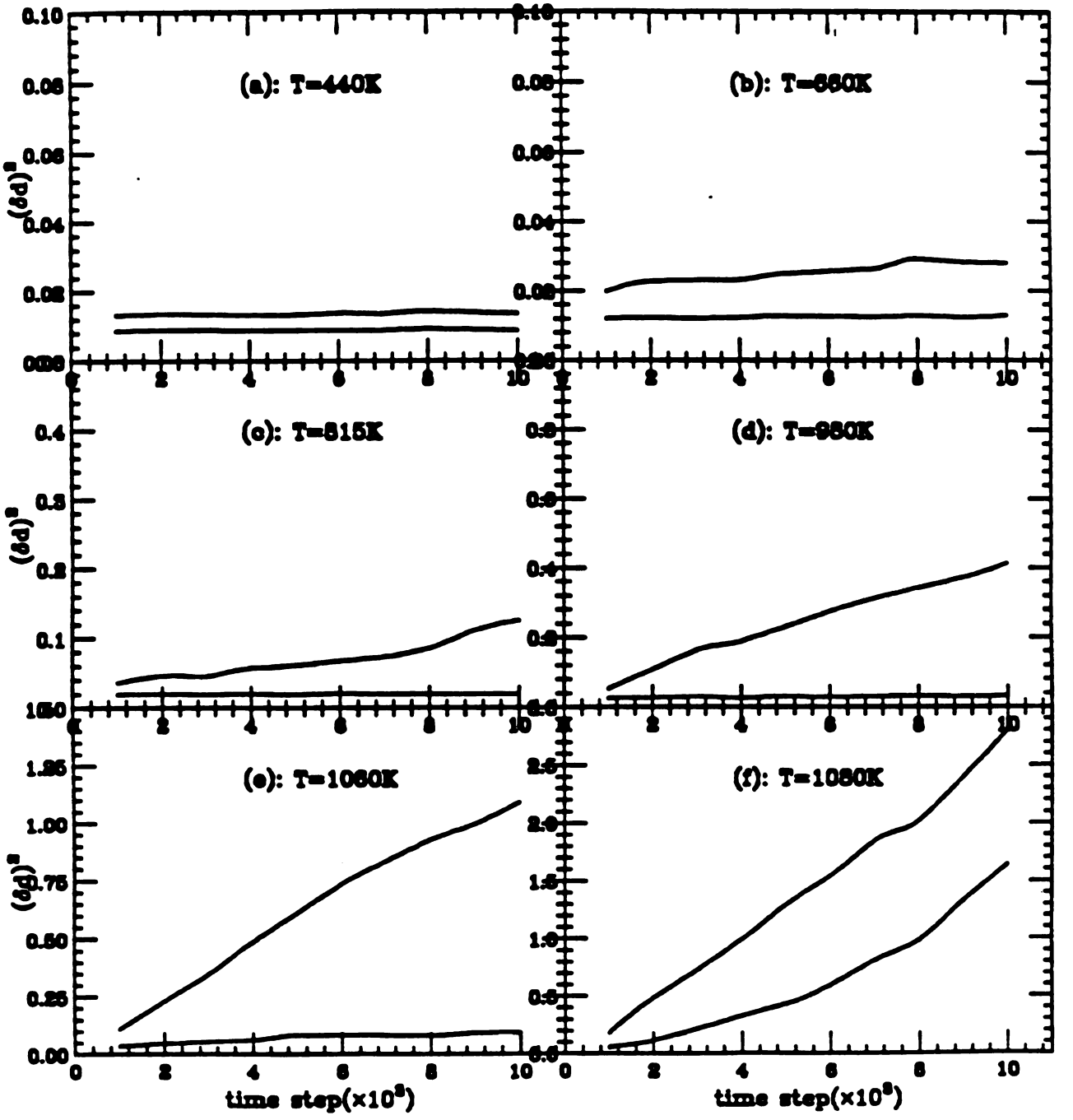

Figure 4.8: Comparison of mean square displacements of surface atoms(upper solid curves) and bulk atoms for the cluster N=725. $(\delta d)^2$ of the surface atoms has larger values than that of the bulk; The bulk atoms do not have diffusive behavior at $T<T_m$, and the surface atoms are diffusive even when the temperature is well below melting.

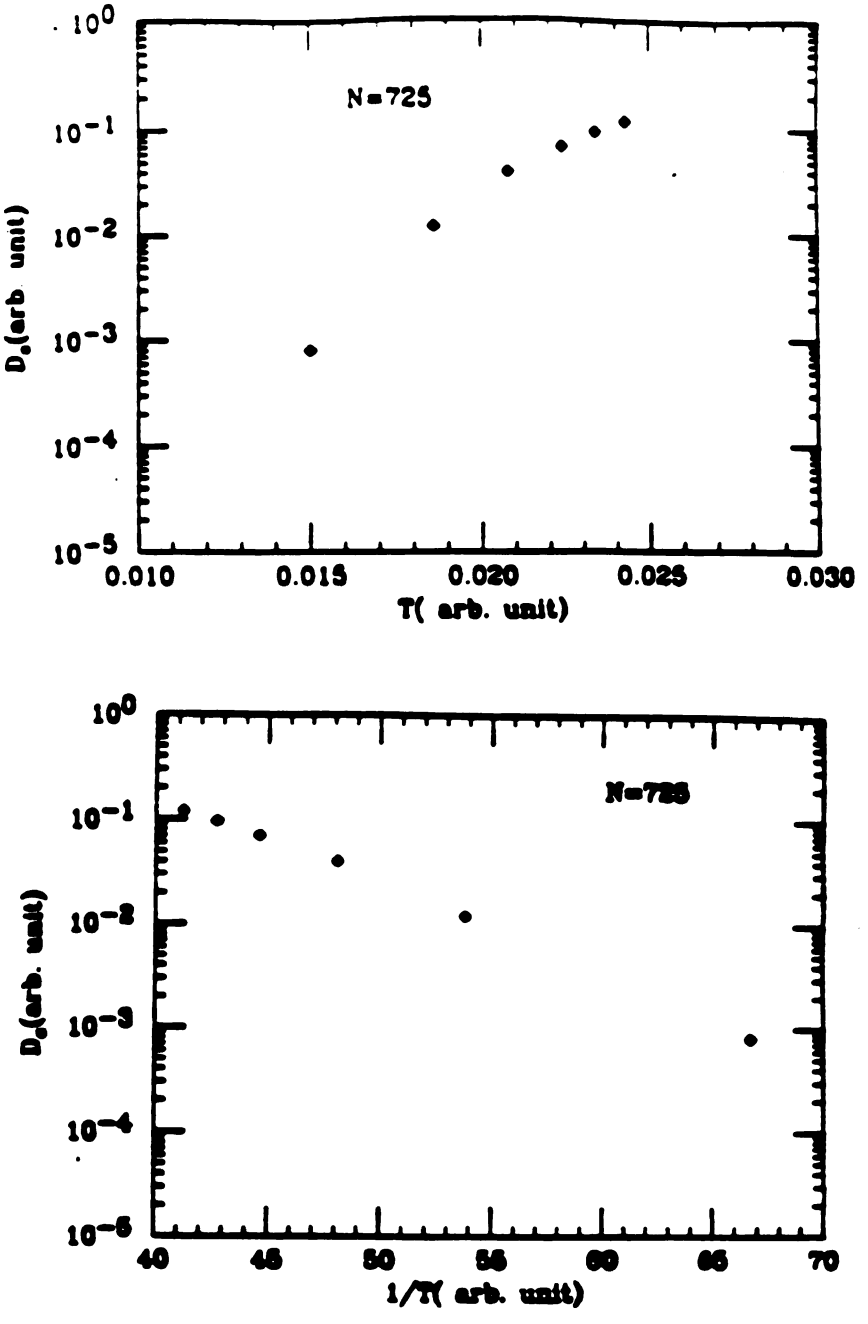

Figure 4.9: Surface diffusion constant D_s as a function of T: D_s monotonically increases with T, D_s is non-vanishing when T>800K; the lower plot is D_s v.s. 1/T, showing the rough linear dependence, the slope contains information on the activation energy.

relationship of $(\delta d)^2$ and t, one is able to estimate the diffusion constants D of the bulk atoms and D_s of the "surface" atoms. Figure 4.9 gives D_s as a function of temperature T. It is seen that the surface diffusion constant D_s decreases as temperature is decreased. Below 800K, surface diffusion is very small. The same calculations were done on a cluster N=381 and similar phenomena is observed. The simulation data are summarized in Figure 4.10. It is also found that the temperature below which no surface diffusion is observed is roughly equal to 800K, the same value estimated from the pervious cluster calculation. But when applying the calculation to N=55 cluster, the surface diffusion and the bulk diffusion seem to take place synchronously and no diffusion occurs prior to melting. For the intermediate size cluster N=177, we did observe surface diffusion at the temperature below but very close to the melting temperature. Because of the difficulty in separating surface and bulk atoms at temperatures near T_m, our calculation results are not conclusive. In summary, surface diffusion exists in large clusters(N>200) at temperatures below melting. But if the temperature is too low(T<800K), it is very hard to observe. T_s(about 800K) does not change much for various size clusters but the melting temperature T_m decreases rapidly as N decreases. As a result, there exists a critical cluster size N_c and when $N < N_c$ the melting

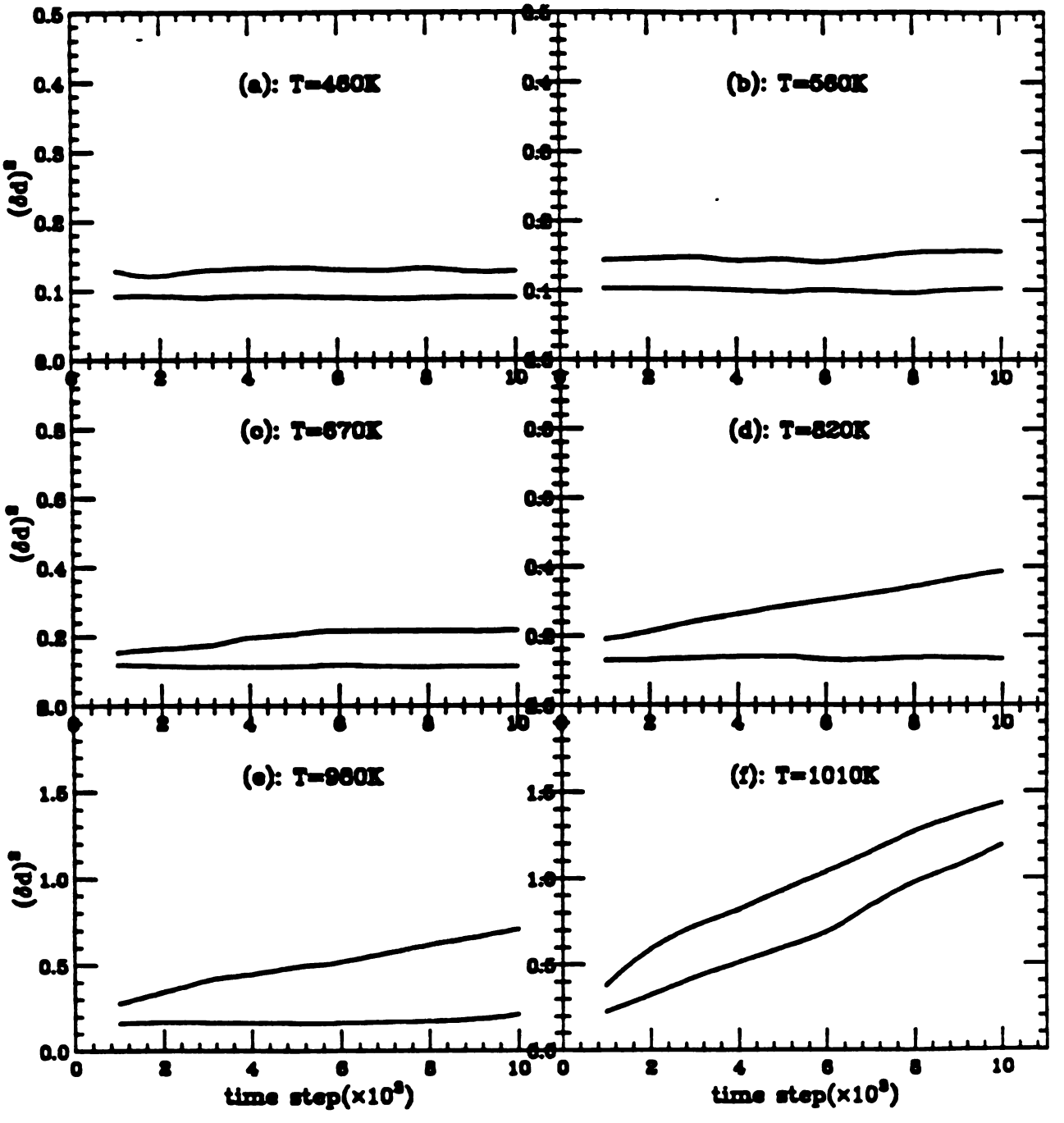

Figure 4.10: Mean square displacement calculation for the cluster N=381: In the calculation, the bulk and surface atoms are treated separately. This cluster has similar diffusion properties to the cluster N=725.

temperature of the cluster is too small (T<800K) to have surface diffusion below melting. A very rough estimate of the critical cluster size gives N_c=150.

4.4 Kinetics of Shape Change in Gold Clusters

Current researches on the dynamics of metal clusters are limited to the calculation of vibrational frequencies by utilizing fast Fourier Transform(FFT). The direct structural changes a small metal cluster may undergo have not been studied. On the other hand, the advanced microscopes enable experimentalists to observe single atomic motion(Ajayan and Marks, 1988,1989). In this section, an effort is made here to narrow the gap between theory and experiment through investigating the shape change kinetics from a non-equilibrium state to an equilibrium state.

Simply, a system in non-equilibrium means that the system deviates from an equilibrium state, which possesses the lowest possible energy. In reality, a system could have many states with energies very close to the ground state. Those states usually have extremely large energy barriers between them. At finite temperature, the free energy F can be roughly considered as a function of configurations. F has numerous minima and each of them represents a meta-stable state. Large energy barriers separate those states and makes it difficult to transfer from one to another. The higher the

temperature is, the more likely it is for the transition from a metastable state to another to occur.

We study small clusters(N≈50) first. The initial configurations of clusters are set to be of an elongated shape. The goal of our calculations is to observe the shape change of the cluster. Initially, any portion of a cluster will have same temperature. It is realizable when the temperature is small because the typical number of time steps necessary for a system to complete heat exchange is much smaller than the time entailed to alter its shape significantly(as will be seen below). We concentrate on cluster N=41, which initially is approximately a 4 by 1 cubic rod(Figure 4.11). We adopted the steep quenching method(Stillinger and Weber, 1982) to freeze the positions of the active corner and edge atoms in order to maintain the initial elongated shape. In the quenching process, we reset the velocities of all atoms to be zero after a short period of simulation. Consequently, the cluster quickly reaches a very low energy state and keeps its elongated shape. The shape parameter is defined by the radius of gyration r_g, written as:

$$r_g^2 = \frac{1}{N}\sum_i [\mathbf{r}_i(t) - \mathbf{r}_c]^2 \qquad (4.26)$$

where $\mathbf{r}_c$ is the center of mass (c.o.m) of the system that is stationary because of zero total momentum; $\mathbf{r}_i(t)$ is the position of atom i. Geometrically, r_g measures the position

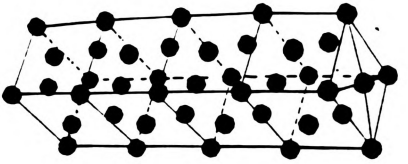

N=41, r_g=1.43

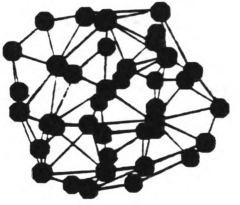

Figure 4.11: Typical initial and final configurations of cluster N=41 in studying the kinetics of non-equilibrium shape change. The upper figure shows an elongated structure which has a value of r_g=1.65; the lower figure is the configuration after reaching equilibrium with r_g=1.43.

distribution of atoms with respect to c.o.m, therefore an elongated cluster has a larger value of r_g than a round and compact one. With the restriction of constant volume, it also measures effective surface area. A configuration of large r_g is unstable and tends to decay to states of smaller r_g values. Our MD simulation is to look at the time dependence of r_g. Figure 4.12 presents the time change of r_g for a cluster N=41 at temperatures T=300K and T=360K. To interpret the phenomena explicitly, two time scales t_c and t_q are defined as indicated in the figure. t_c called the completion time,is the time step at which r_g is approximately at middle of the initial and final value. t_q, the decaying time characterizes the time step needed to finish the transition of r_g from high to low. In Figure 4.12, t_q is of order of tens of thousands of time steps while t_c is roughly one million time steps. t_c is strongly dependent on the temperature. At very low temperature, an elongated configuration in a metastable state may not alter its shape for such a long time that a time scale 100ns has no impact on the overall profile of the cluster. I did simulations on an N=41 cluster at about half of its melting temperature(240K), and the simulation was extended to 10^7 time steps. No big change in r_g occured. It is found that t_c also has a dependence on its initial configuration. We fix temperature and change the initial condition for the cluster

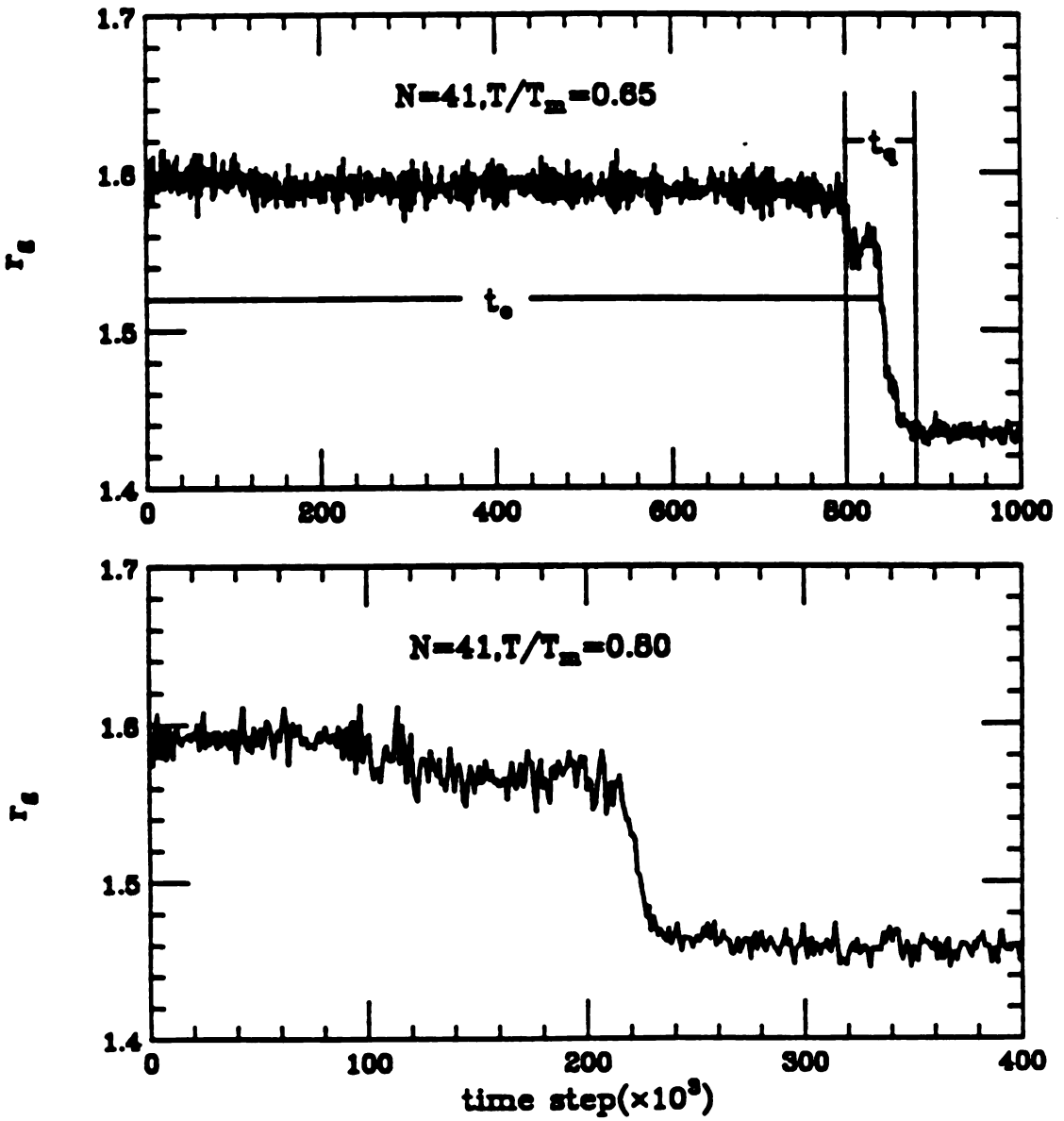

Figure 4.12: Radius of gyration $r_g(t)$ as a function of time at T=300K and T=340K for N=41. In these two figures, $r_g(t)$ has no significant change until a large time scale t_c as defined in the upper figure; but completes compactification within a very short period t_q.

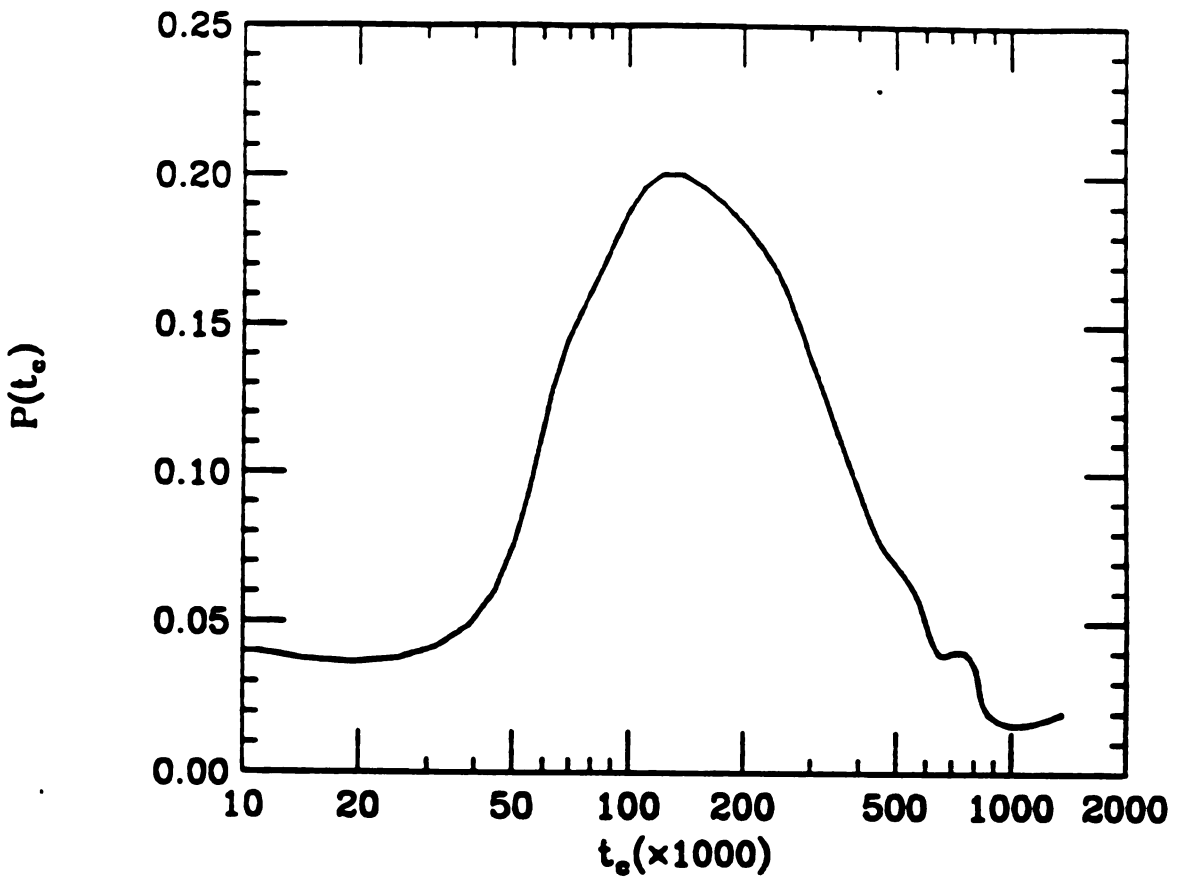

Figure 4.13: The distribution of t_c for N=32 clusters. We change the initial configurations and fixed the temperature. The statistics is done on 100 configurations. t_c has a very broad distribution; the figure shows a linear-log plot which yields a reasonable statistics.

N=32 and find that t_c has a distribution so broad that a simple statistical analysis failed. Figure 4.13 shows a log-linear plot of distribution of t_c, indicating that only $\log t_c$ has reasonable statistics. As to the system size effect, we fixed temperature and chose clusters N=59 and 67 for comparison with the cluster N=41. We did observe that t_c increases as N increases. Nevertheless, the melting temperature is also increasing with N, so the temperature difference from melting point is also increasing with N.

In large clusters, it is more difficult to observe substantial alteration in r_g at low temperature, therefore we restrict our calculations to temperatures close to melting. The clusters chosen are N=711, 613, 515, 417, 319 and 213. First we estimate the melting temperatures of these clusters and find that T_m=0.0242, 0.0238, 0.023, 0.022, 0.021, 0.019 respectively. Again, the starting profiles of clusters are set to be elongated and the radius of gyration is calculated as a function of temperature. We run the simulation up to 3,000,000 time steps. Our calculation results are presented in Figure 4.14, which shows how r_g behaves at different temperatures and system sizes. For cluster N=613, the temperatures are chosen to be T/T_m=0.96, 0.92, 0.86. At $T=0.96T_m$, r_g has the abrupt decay as described in the previous paragraph. But at $T=0.92T_m$ and $0.86T_m$, r_g decays rather smoothly and gradually. It is also

noticed that the decay at $0.86T_m$ is significantly slower than at $T=0.90T_m$. For the cluster N=515, the temperature chosen are $T/T_m=0.90,0.85$ and 0.78. At $T=0.90T_m$, r_g has arrupt decaying behavior while at $T=0.85T_m$ and $0.78T_m$, the decay is gradual. For the cluster N=711, at temperatures $T/T_m=0.92,0.88,0.82$, the decay of r_g is always gradual, but we expect as the temperature is close enough to the melting temperature the abrupt decay behavior will eventually show up. For the cluster N=213, we did not observe the slow decay behavior. If temperature is close to melting, the abrupt decay is observed and if temperature is low, the overall shape is hardly changed. Accordingly, two distinct phases can be categorized. Let Phase I label the gradual decay of r_g, and Phase II stand for the abrupt decay. Then we observed that at temperatures very close to melting, the cluster is in Phase I and crosses over to Phase II as temperatures decreases. Because the slow and gradual decay behavior of r_g exists only in large size clusters, it implies that the decay mechanism is surface diffusion below T_m, which is absent in the small clusters.

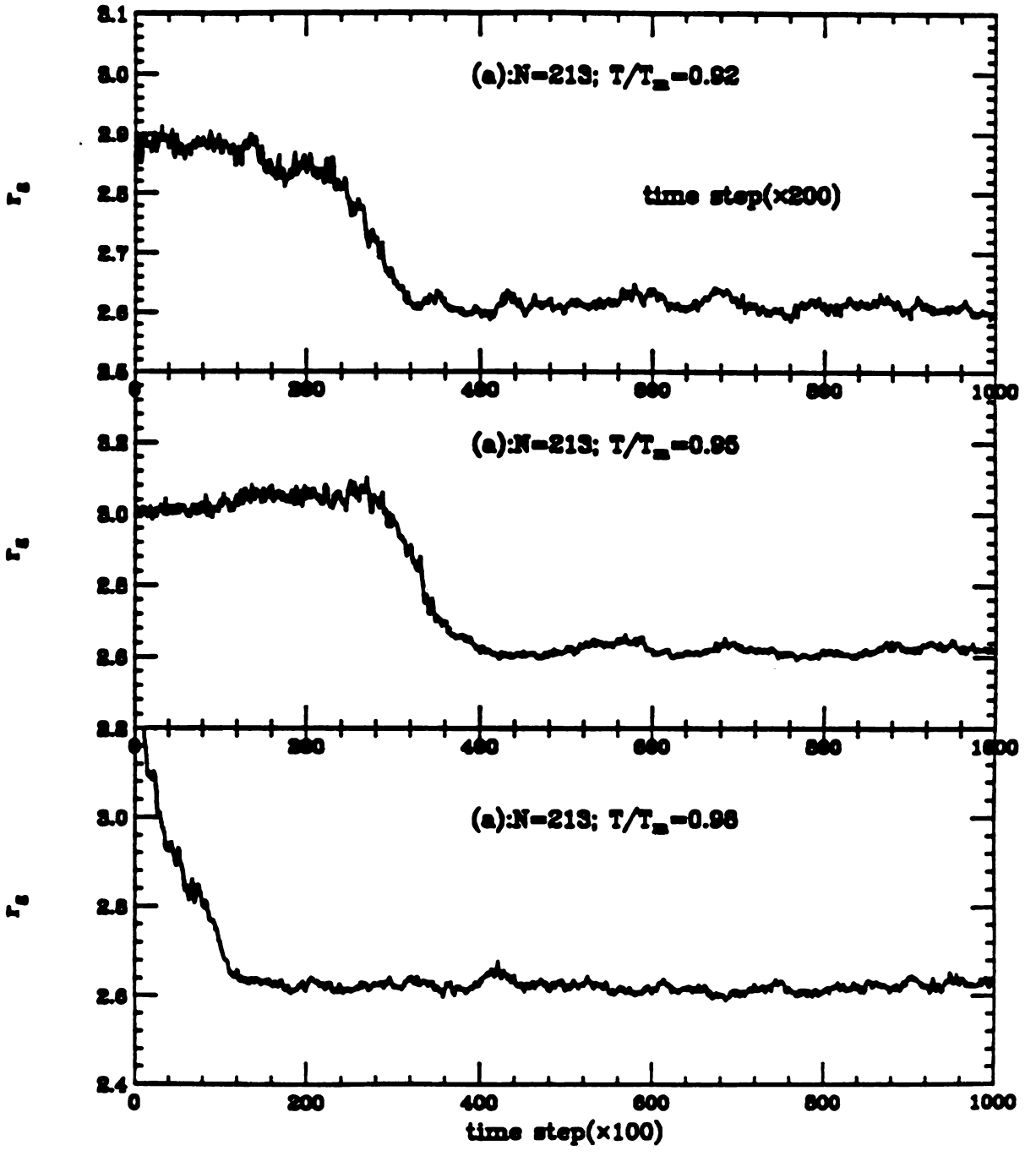
(a):N=213; T/T_m=0.92
time step(×200)
(a):N=213; T/T_m=0.95
(a):N=213; T/T_m=0.98
time step(×100)

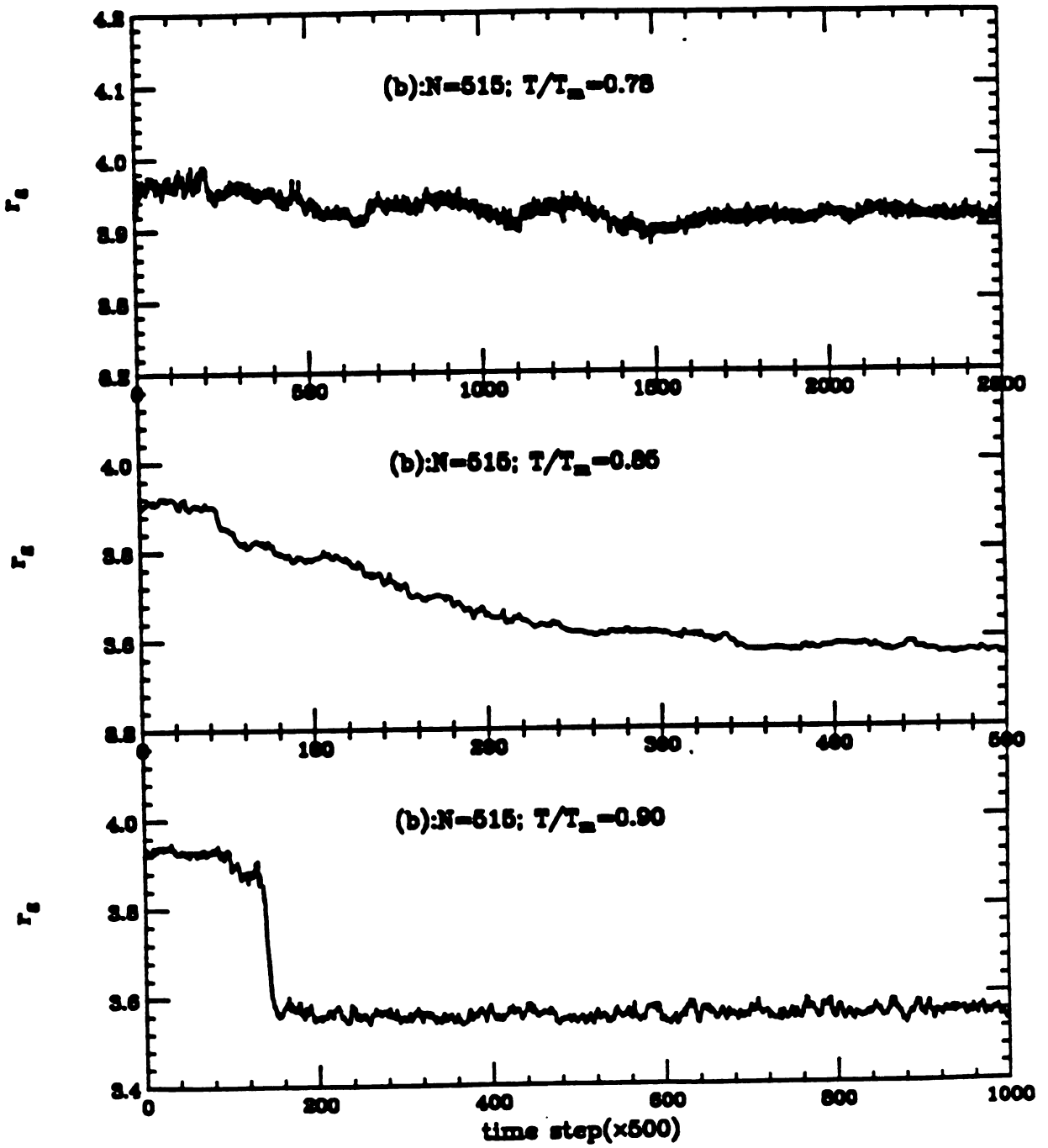
(b):N=515; T/T_m=0.78
(b):N=515; T/T_m=0.85
(b):N=515; T/T_m=0.90
r_a
time step(x500)

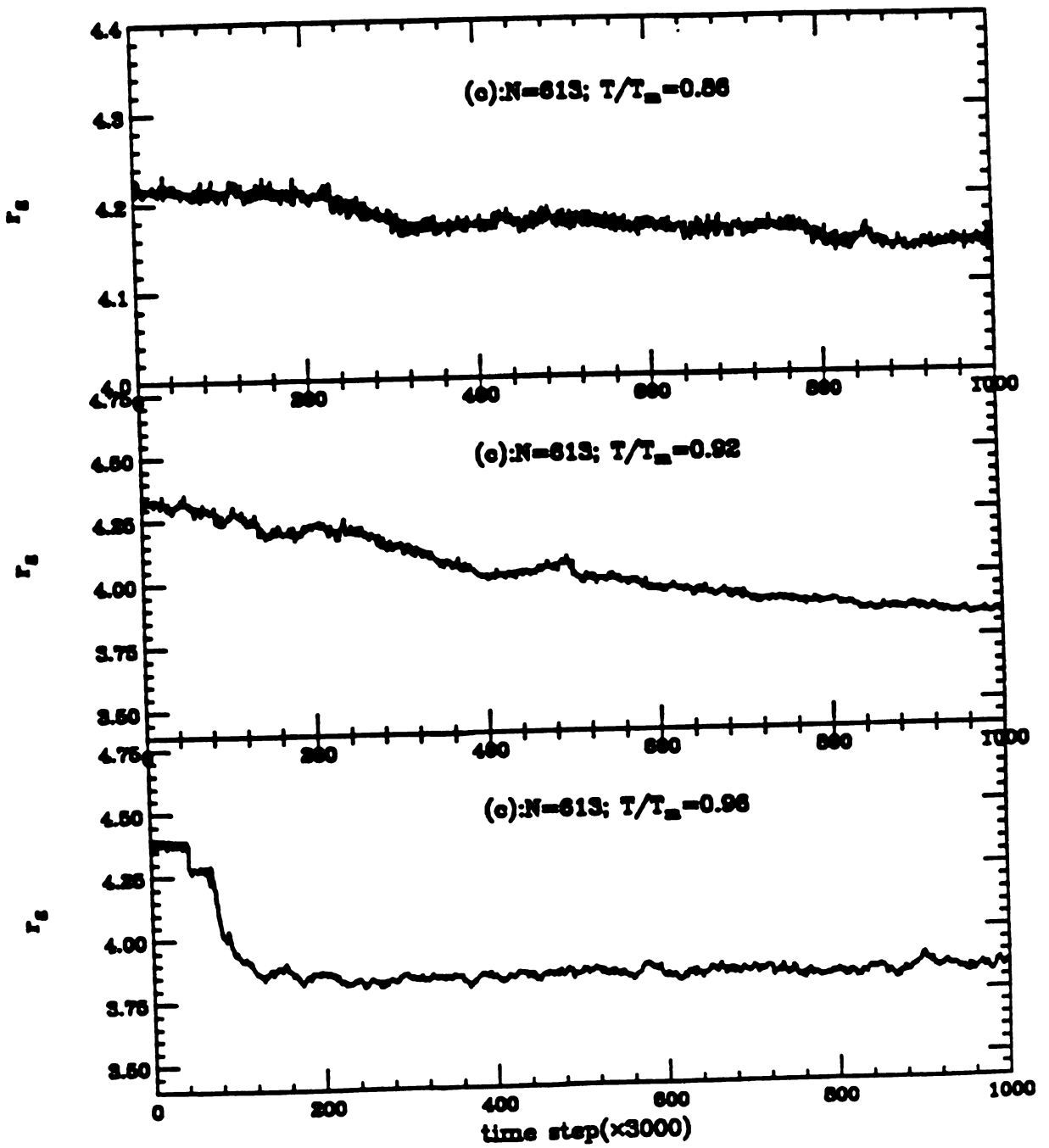
(c):N=613; T/T_m=0.86
(c):N=613; T/T_m=0.92
(c):N=613; T/T_m=0.96
r_s
time step(×3000)

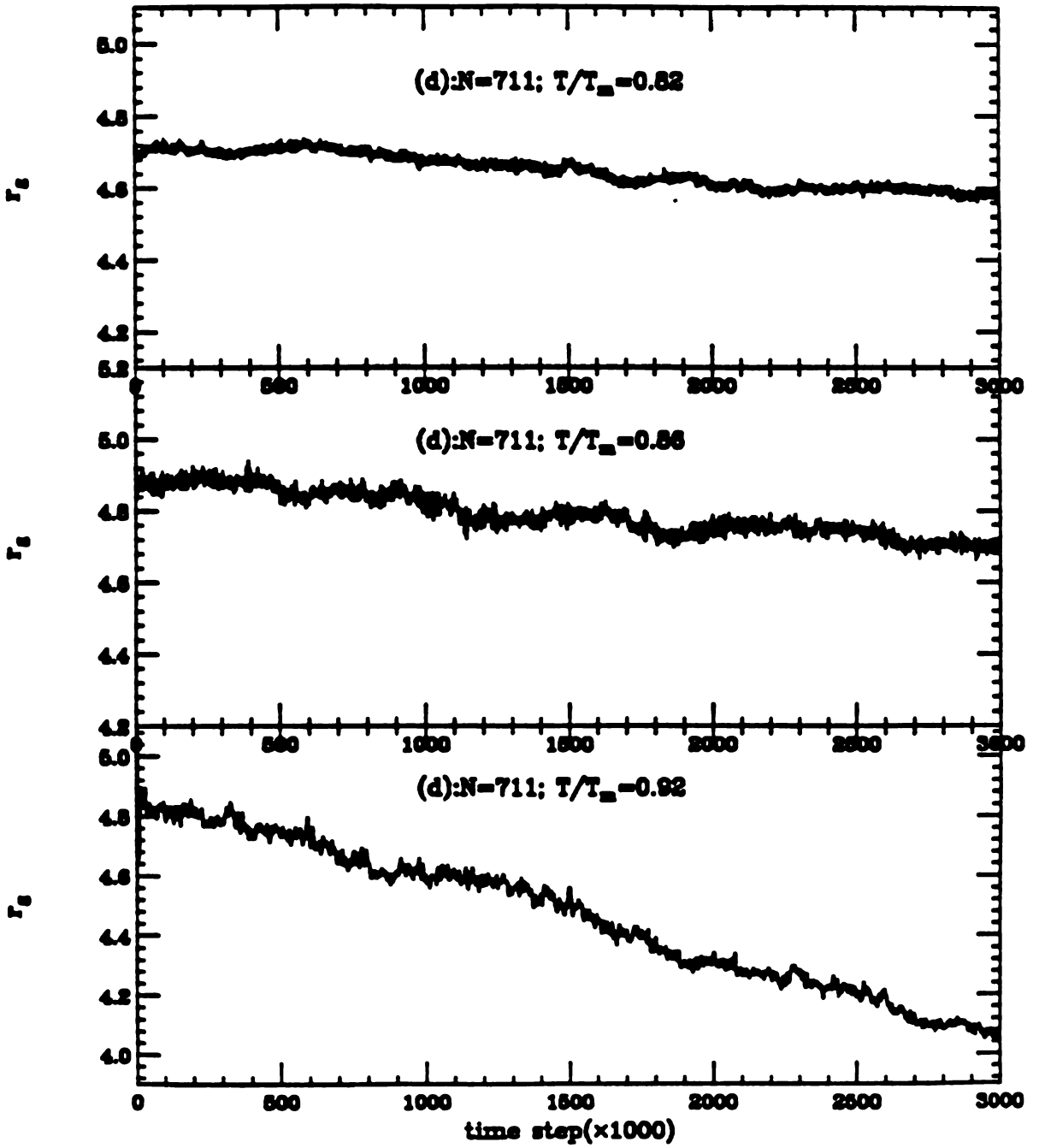

Figure 4.14: $r_g(t)$ at different temperatures $T<T_m$ for the large clusters N=213, 515, 613 and 711: the temperatures are normalized to their melting temperatures. $r_g(t)$ decays distinctly at T close to melting and at T a little away from it. When T is very close to T_m, $r_g(t)$ decays abruptly compared with a slow and gradual decay at lower temperature.

So far, only clusters of solid-like phase have been considered. When the temperature is raised to surpass the melting temperature, atoms in the cluster start to diffuse and therefore, the transition from a non-equilibrium state to equilibrium becomes much quicker than that in a solid phase. Since the time scale of the transition is compatible to that of thermal equilibration, the term isothermal shape change is inadequate here to describe the prompt equilibrating process. However, it is still feasible to utilize r_g as the parameter to look into the shape change because the shape alteration of clusters will certainly not change the phase of the cluster, in other words, the cluster will remain in the liquid phase. A single configuration of r_g as a function of simulation time for a liquid cluster has large fluctuations as seen in Figure 4.15a. But it is clear that the statistical average yields a rather smooth curve which has a well defined behavior(Figure 4.15b), showing roughly exponentially decay(Figure 4.15c). From the averaged decay curve, we measured the decay constant τ. We measured τ as a function of temperature for three different sizes of clusters(N=41, N=213, and N=613). The results are plotted in Figure 4.16, from which two conclusions can be drawn: (1) τ decreases as temperature increases, and it reaches a stable value at high temperature. (2) The stabilized value of τ is

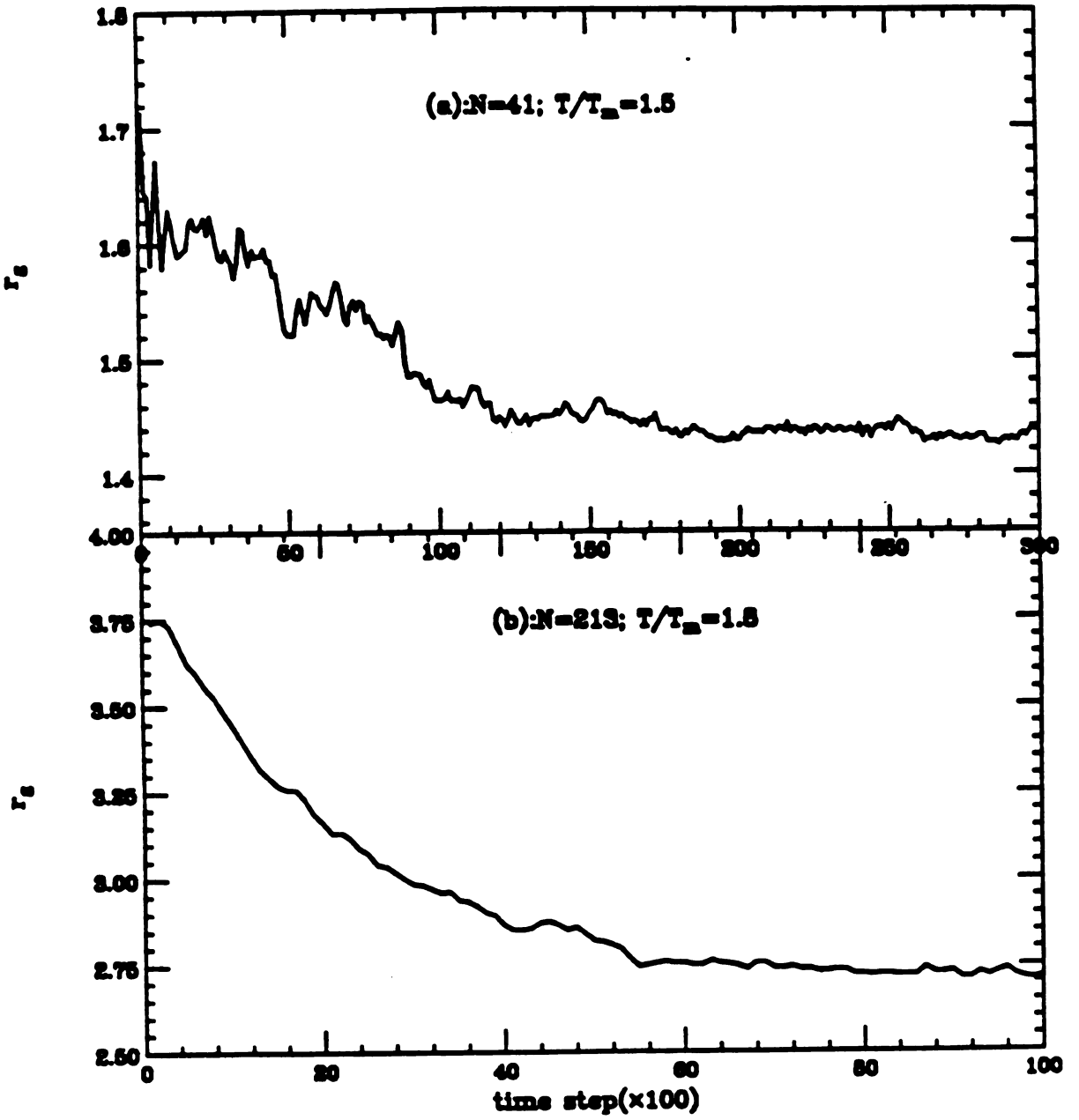
(a):N=41; T/T_m=1.5
(b):N=213; T/T_m=1.5
r_s
r_s
time step(×100)

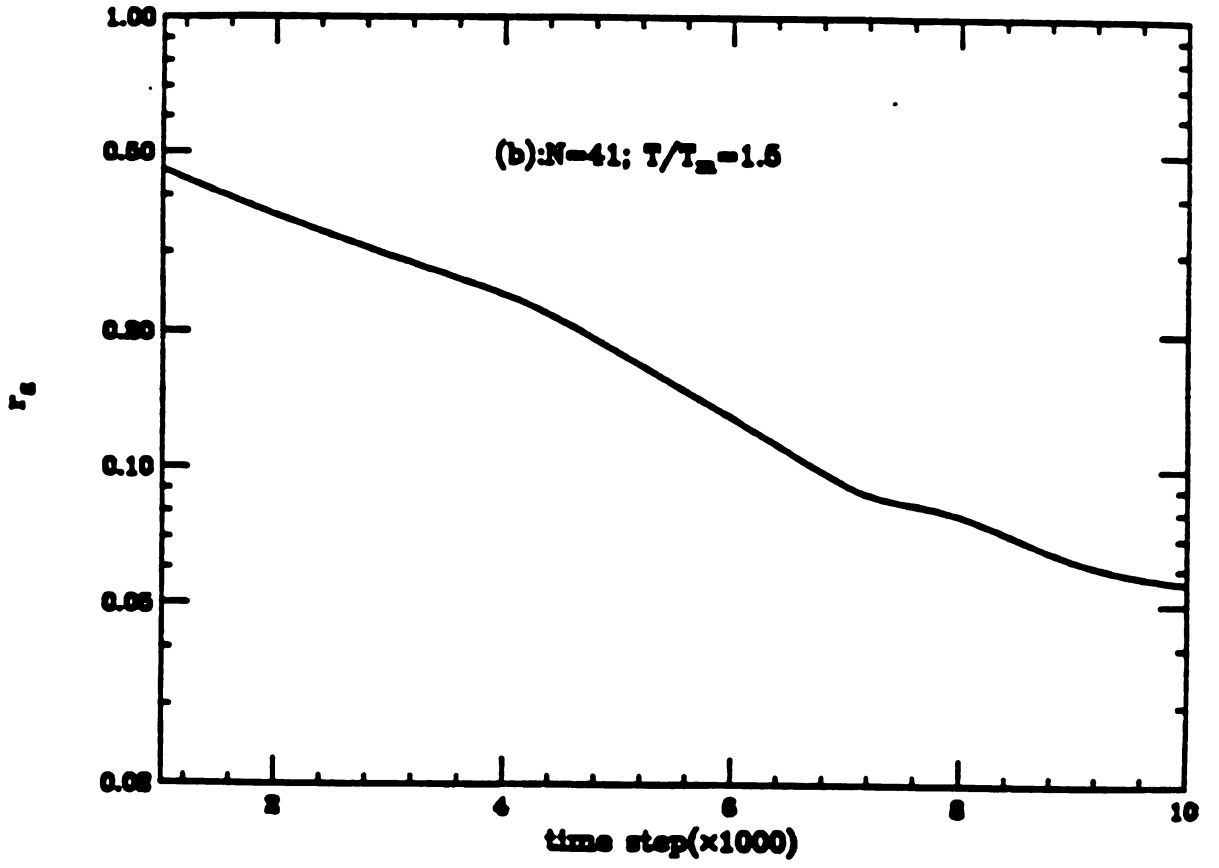

Figure 4.15: $r_g(t)$ at $T>T_m$ for the clusters N=41,213, $r_g(t)$ decays approximately exponentially but with big fluctuations. The average behavior of $r_g(t)$ has a well defined decay time constant τ which is defined as the slope of the log-linear curve above.

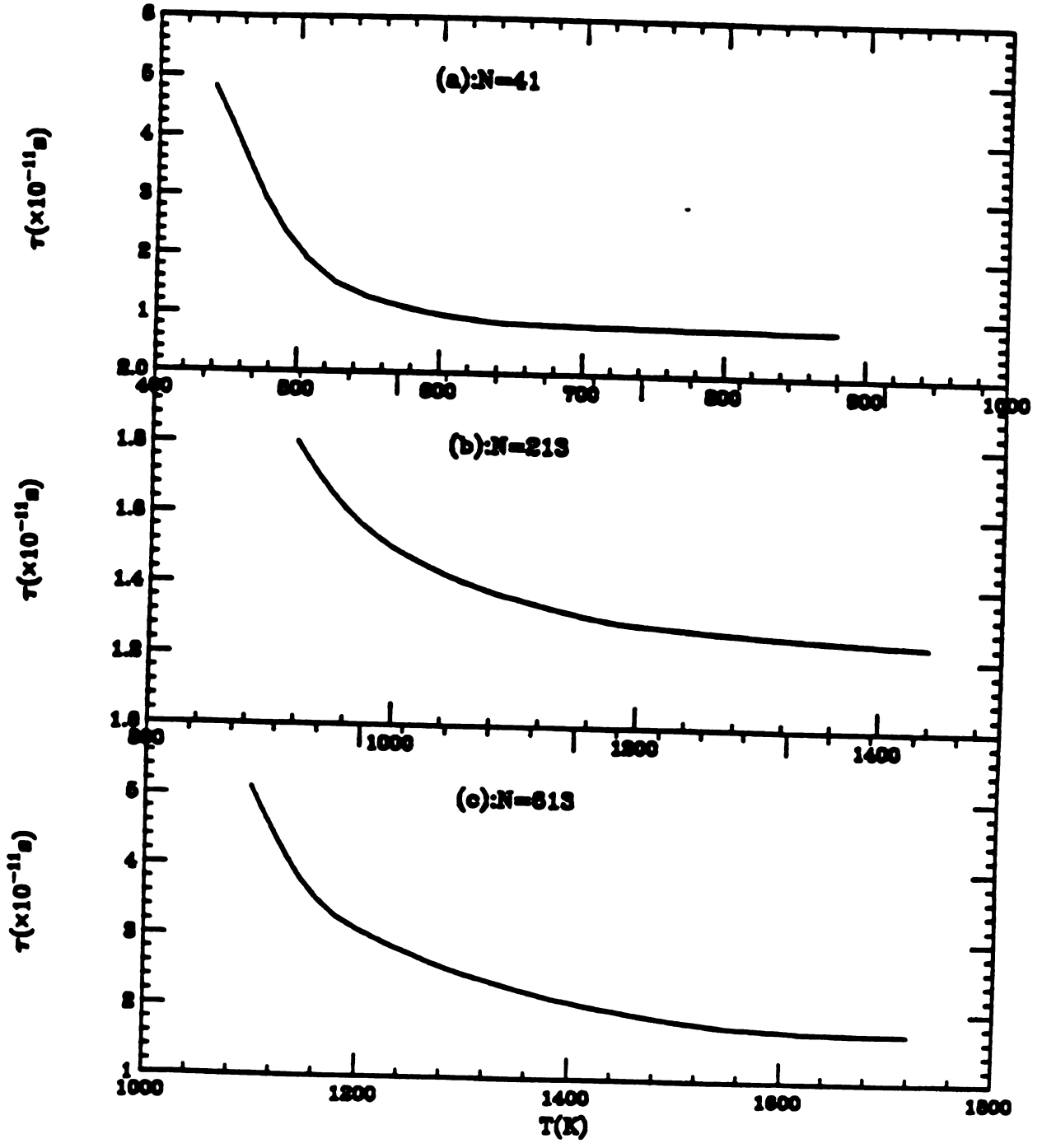

Figure 4.16: τ measurements for the clusters N=41, 213, 613. τ decreases with T; it stablizes at sufficiently high T. The stablized value is a weakly increasing function of system size.

a weakly increasing function of system size N. The conclusion (1) is consistent with the phenomena that the equilibration constant of a liquid droplet is weakly dependent on temperature.

In summary, the molecular dynamics simulation is carried out to study the kinetics of non-equilibrium shape change in clusters. We utilized the radius of gyration r_g as a shape parameter to monitor the equilibration process. It is found that r_g behaves distinctly in three temperature regions for large clusters. Above melting, r_g decays roughly exponentially. Near and below melting point, clusters undergoes rapid compactification at some characteristic time. In large clusters at low temperatures, r_g decays rather smoothly and algebraically slowly. In small clusters, r_g rapidly compactified at temperature below melting. Those decay behaviors of r_g are summerized in Figure 4.17 that shows how r_g decays at various temperatures and cluster sizes.

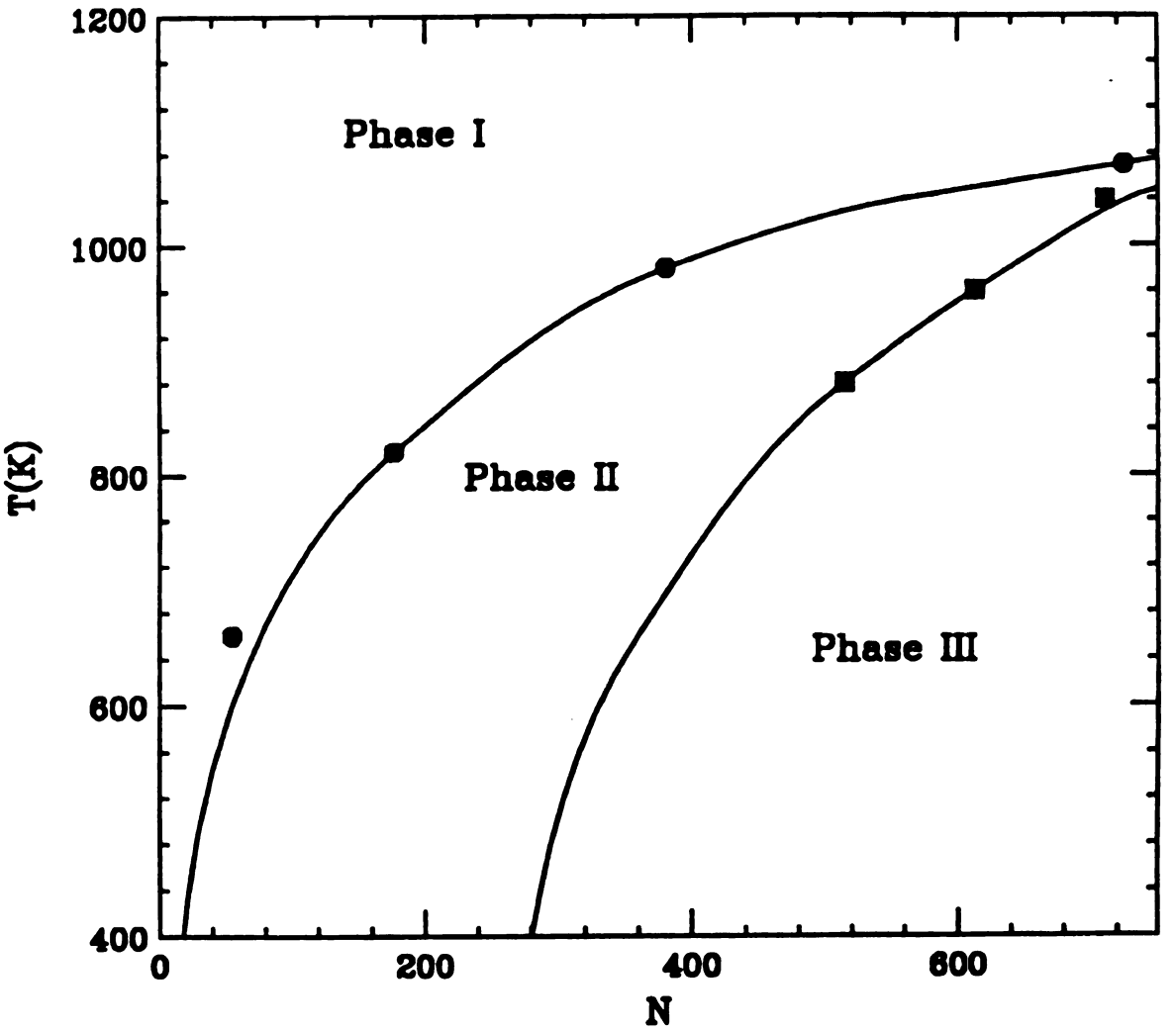

Figure 4.17: Dynamic behavior of gold clusters. In the figure, three distinct behaviors of decay of $r_g(t)$ are identified. In Phase I, it corresponds to the case of liquid coalescence; Phase II stands for the abrupt decay behavior and Phase III is slow decay due to surface diffusion.

CHAPTER FIVE

QUANTUM TRANSPORT ON 2D PERCOLATING MEDIA

5.1 Introduction:

5.1.1 Anderson localization

The electronic states in a perfect crystal material are extended with Block wavevector **k**. An incidental defect in the crystal can be viewed as a scattering problem of electrons on the defect. When there are many defects randomly located in the crystal, an extended electronic state may be altered profoundly in nature(Anderson, P.W., 1958) by the disorder and collective effect of defects.

Roughly speaking, there exist two broad distinct classes of disordered systems: i)systems with substantial, cellular or compositional disorder and ii)systems with positional, topological or structural disorder. The first class of disordered systems include the famous Anderson model (Anderson,P.W., 1958,1961) which uses the following Hamiltonian:

$$H = \sum_{m} \varepsilon_m a_m^{+} a_m + \sum_{m \neq m'} J_{mm'} (a_m^{+} a_{m'} + a_{m'}^{+} a_m) \qquad (5.1)$$

where ε_m is the energy level of site m, and $J_{mm'}$ is the overlap or hopping integral between site m and its nearest

neighbor m'. The disorder was introduced by making the site energy be uniformly distributed over a certain range, -W/2 to W/2. $J_{mm'}$ was assumed constant. Let V stand for the energy bandwidth in the absence of disorder, and the ratio W/V represents the magnitude of disorder. When W/V is sufficiently large, all electron states are localized, having the asymptotic form(Lee etc.,1985):

$$|\psi(\mathbf{r})| \sim \exp(-|\mathbf{r}-\mathbf{r}_0|/\xi) \qquad (5.2)$$

where ξ is the localization length. When W/V is small, the localized states show up only at the bottoms and tops of an energy band. In an energy band, there exist energies called mobility edges separating localized states and extended states. As energy approaches a mobility edge, ξ diverges:

$$\xi \sim |E - E_c|^{-\nu} \qquad (5.3)$$

where the index ν reveals the critical behavior of ξ and E_c is one of those mobility edges.

In terms of Hamiltonian (5.1), an alternative way of introducing the randomness is to let ε_m be constant, and $J_{mm'}$ random, which corresponds to the situation of off-diagonal disorder and the second class of disordered system. The simplest model with off-diagonal disorder is that of quantum percolation which takes p as the probability that a bond exists or 1-p as a bond is absent. The raised question is whether the localization caused from off-diagonal disorder falls in the same universality class as the well studied

site disordered case. To gain a quantitative understanding of the question, one obvious approach is to carry out detailed numerical calculations or simulations and compare the results with the theory. In this chapter, we performed a detailed calculation and analysis of conductance of two dimensional percolation systems. Two key issues are addressed in the chapter: (1)all electronic states are localized in 2-d percolation systems; (2)the wavefunctions of those states might be superlocalized near classical threshold. In the rest of the section, I will go over some fundamental concepts in percolation theory and localization theory. In Section 5.2, a description of two methods of calculating conductance will be outlined. Then in Section 5.3, the numerical calculation results are presented. Finally, conclusions and open questions are discussed.

5.1.2 Scaling of localization:

The nature of Anderson localization was unclear until the scaling theory of localization was discovered(Thouless, 1977). The divergence of the localization length ξ near E_c implies one could employ the renormalization group used in analyzing thermal phase transitions where the correlation length diverges as the temperature approaches the critical temperature. When applying the real-space renormalization-group method to localization problems, one divides the

infinite lattice into finite cells of b^d and thus the Hamiltonian is written as:

$$H = H_0 + H_1 \qquad (5.4)$$

where H_0 includes all site-diagonal terms and off-diagonal terms which connect sites m, m' within the same cell. The remaining off-diagonal terms are included in H_1. The eigenvalues E_α and normalized eigenfunctions $|\Phi_\alpha\rangle$ of H_0 can be found by exact diagonalization. The objective of renormalization is to find a mapping Hamiltonian characterized by E_α, the renormalized local energy and $J_{\alpha\alpha'}$, the renormalized nearest neighbor hopping constant, i.e. the relationship between $(E_\alpha, J_{\alpha\alpha'})$ and $(\varepsilon_m, J_{mm'})$. From each cell, one picks out one state which is included in the subspace D of Hilbert space that H_0 spans. Introducing the projection operator P_D of $|\Psi\rangle$ onto D, $|\Psi_D\rangle = P_D|\Psi\rangle$ Where P_D can be expressed as:

$$P_D = \sum_{\alpha \in D} |\Phi_\alpha\rangle\langle\Phi_\alpha| \qquad (5.5)$$

Defining the Green's Function

$$G = (E - H_0)^{-1}(1 - P_D) \qquad (5.6)$$

then

$$|\Psi\rangle = |\Psi_D\rangle + GH_1|\Psi\rangle \qquad (5.7)$$

Defining another operator Q by $|\Psi\rangle = Q|\Psi_D\rangle$, and then V_D by $V_D = H_1 Q$, one finds $Q = 1 + GH_1 Q$ and therefore

$$V_D = H_1 + H_1 G V_D \qquad (5.8)$$

Noticing $V_D|\Psi_D\rangle = H_1|\Psi\rangle$, it is found that

$$(H_0 + V_D)|\Psi_D\rangle = E|\Psi_D\rangle \tag{5.9}$$

One can obtain V_D by expansion in series of H_1. Keeping only the linear term i.e. $V_D=H_1$ and defining $H_D = H_0 + V_D$, we have

$$H = \sum_{\alpha} E_{\alpha} a_{\alpha}^{\dagger} a_{\alpha} + \sum_{\alpha \neq \alpha'} J_{\alpha\alpha'} (a_{\alpha}^{\dagger} a_{\alpha'} + a_{\alpha'}^{\dagger} a_{\alpha}) \tag{5.10}$$

where $\langle\alpha,\alpha'\rangle$ are nearest neighbor cell indices and $J_{\alpha\alpha'}=\langle\alpha|H_1|\alpha'\rangle$. Principally, one could find the recursive relationships between $(J_{\alpha\alpha'}, E_{\alpha})$ and $(J_{mm'}, \varepsilon_m)$. Consider the diagonal disorder situation, one could make the approximation that $J_{\alpha\alpha'} = J_{eff}$ are constant and E_{α} has a new distribution whose width or effective disorder is written as

$$W' = \left(\langle E_{\alpha}^2 \rangle - \langle E \rangle^2\right)^{1/2} / J_{eff} \tag{5.11}$$

and the energy E is changed to E':

$$E = (E - \langle E_{\alpha} \rangle) / J_{eff} \tag{5.12}$$

Then the scaling for localization length reads

$$\xi' = \xi(W', E') = b^{-1} \xi(W, E) \tag{5.13}$$

If one considers the case that the energy lies at the center of the band, according to the symmetry, E=E'=0. In other words, in the (W,E) plane the E=0 axis is invariant under RG transformation. Thus the recursive equations become W'=f(W) alone. The fixed points are given by solving the equation W=f(W). Obviously W=0 is a stable fixed point because the renormalization process should not introduce disorder in to a perfect system. The non-trivial solution

$W=W_c\neq 0$, if it exists, represents a critical degree of randomness above which all electron states are localized. In that case, $W = W_c$ is an unstable fixed point at which the localization length ξ diverges.

More quantitative analysis of scaling of localization is to consider the behavior of conductance Γ or reduced conductance g defined as $g = \Gamma/(e^2/h)$ as a function of system size L. When randomness is small, the electronic wave function is extended and is nearly plane wave-like. The conventional transport theory is valid and the ohm's law gives:

$$g(L) = \sigma L^{d-2}/(e^2/h) \qquad (5.14)$$

here σ is the conductivity viewed as a local quantity independent of system size L. Equation (5.14) is the ohmic limit of g(L). In the limit of strong localization, the conductance is due to hopping from one occupied state to an unoccupied state. The conductance is then proportional to the probability that an electron hops between two energetically close states which have a typical separation L. This probability is proportional to the overlap of two localized wavefunctions, thus in the strong disorder limit, g(L) has the scaling form:

$$g(L) = g_0 \exp(-L/\xi) \qquad (5.15)$$

g_0 is some microscopic conductance value that is of order one.

For a particular degree of disorder, g(L) evolves smoothly as L increases, crossing over to either an ohmic region or to a strong localization limit. Here we use the argument given by the gang of four(Abrahams,E., etc. 1979) that assumed the quantity

$$\beta = d\log g / d\log L \qquad (5.16)$$

is a function of g alone, not explicitly dependent on system size L. When g is very large, equation (5.14) is used, then β is easily computed: β(g)=d-2. Particularly for two dimensional systems β=0. If $g<<g_0$, using the strong localization limit(Equation (5.15)), $\beta=\ln(g/g_0)$, which still depends on g only. Perturbation theory in the large g limit proves that $\beta = d-2-a/g$(Bergmann,1984) where a is a positive constant. As it is presumed that β is a monotonically increasing function of g, β is always negative in one and two dimensional disordered systems. The non-positivity of β implies that any finite degree of disorder will cause non-conductivity in 1d or 2d macro-systems. However, the conclusion is still controversial(Azbel,1991; Soukoulis and Grest,1991; Stein and Krey,1987) in the situation of two dimensional disordered system where the localization length is very large at small disorder(Lee etc.,1985).

5.1.3 Scaling behavior of percolating systems:

The most important feature of the percolation model is the occurrence of an infinite cluster(Stauffer,1985) of sites(or bonds) for $p>p_c$, where p_c denotes the percolation threshold value. P(p) is an order parameter defined as the probability that an arbitrary site(bond) belongs to the infinite cluster. When $p<p_c$ no infinite cluster exists, thus P(p)=0. As p is reduced to approach p_c from above, P(p) has the scaling behavior:

$$P(p) \sim (p - p_c)^{\beta} \tag{5.17}$$

indicated by exponent β. The correlation length and classical resistivity both diverge at p_c.

$$\xi_p \sim (p - p_c)^{-\nu} \tag{5.18a}$$

$$\rho_c = 1/\sigma_c = (p - p_c)^{-\mu} \tag{5.18b}$$

Near p_c, the structure of the infinite cluster is fractal with dimension d_f. d_f can be obtained from a simple scaling argument. Consider a block of size L in the infinite cluster and L satisfies: $a<<L<<\xi_p$, where a is lattice constant. The weight(mass) of the block is proportional to $P(p)L^d = L^{d_f}$. Let $L = \xi_p$, in which case we have the following relationship:

$$(p - p_c)^{\beta} \sim \xi_p^{d-d_f} \sim (p - p_c)^{-\nu(d-d_f)} \tag{5.19}$$

and therefore $d_f = d - \beta/\nu$.

Diffusion on the infinite incipient cluster at p_c is anomalous and the mean square distance of a random walker from the origin after time t behaves as $\langle r^2 \rangle \sim t^{2/d_w}$ (when $d_w=2$, we get normal diffusion.) The diffusion constant on the

cluster is defined as $D = \frac{1}{2} d\langle r^2 \rangle / dt$ and D relates to the dc conductivity(Harris,1984) by

$$\sigma = e^2 n D / kT \qquad (5.20)$$

where n, the density of charged carriers, is proportional to P(p). Thus, the simple scaling argument yields $D \sim (p - p_c)^{\mu-\beta} \sim \xi_p^{\theta}$ with $\theta = (\mu - \beta)/\nu$. In general, for a scale L<ξ, D scales as $D \sim \xi_p^{\theta} f(L/\xi_p)$. When L is small, D should not depend on ξ_p, which implies the function $f(x) \sim x^{\theta}$ as $x \to 0$. Therefore $D \sim dr^2/dt \sim r^{-\theta}$ or

$$r^2(t) \sim t^{2/(2+\theta)} \qquad (5.21)$$

This expression is useful in discussing of super-localization(Levy and Souillard,1987; Brooks and Aharony, 1987) of electron states on a fractal lattice. The topic will be briefly discussed in last section of this chapter.

5.2 Calculations of Conductance

5.2.1 Linear response theory:

Many experiments in condensed matter physics measure the linear response to small external fields such as mechanical forces, magnetic fields, electric fields or optic fields on materials. In electrical conduction, a time dependent external electrical field

$$\mathbf{E} = \mathbf{E}_0 \exp(i\mathbf{q}\cdot\mathbf{r} - i\omega t) \qquad (5.22)$$

is applied and the induced current is measured. Linear response suggests that the induced current is proportional to the applied field:

$$\mathbf{J}(\mathbf{q},\omega) = \sigma(\mathbf{q},\omega)\cdot\mathbf{E}(\mathbf{q},\omega) \tag{5.23}$$

where σ is a second rank tensor and the expression can be viewed as the fundamental definition of the microscopic conductivity. The dc conductivity is obtained from taking the limits $q\rightarrow 0$ and $\omega\rightarrow 0$ in that order.

When a field is applied, the Hamiltonian consists of two parts: one is the unperturbed term H_0 and the interaction term H' is expressed as:

$$H' = -\frac{1}{c}\int d^3r\mathbf{j}(\mathbf{r})\cdot\mathbf{A}(\mathbf{r},t) \tag{5.24}$$

$$\frac{1}{c}\mathbf{A}(\mathbf{r},t) = -\frac{i}{\omega}\mathbf{E}(\mathbf{r},t) \tag{5.24a}$$

The current density relates to average velocities through $\mathbf{J}(\mathbf{r},t) = e\sum_i \langle \mathbf{v}_i \rangle$ and $\mathbf{v}_i = \frac{1}{m}[\mathbf{p}_i - \frac{e}{c}\mathbf{A}(\mathbf{r}_i)]$. Therefore, the current density is sum of two parts: $\mathbf{J}=\mathbf{J}_1+\mathbf{J}_2$, with $\mathbf{J}_1$ and $\mathbf{J}_2$ having the following expressions:

$$\mathbf{J}_2 = \langle \mathbf{j}(\mathbf{r},t)\rangle = \frac{e}{m}\sum_i \langle \mathbf{p}_i \rangle \tag{5.25}$$

$\mathbf{J}_1$ is the displacement current and proportional to $\mathbf{E}$

$$\mathbf{J}_1 = \frac{in_0e^2}{m\omega}\mathbf{E}(\mathbf{r},t) \tag{5.26a}$$

The expectation value of $\mathbf{j}(\mathbf{r},t)$ is expressed in the interaction representation

$$\mathbf{J}_2(\mathbf{r},t) = \langle \psi' | \mathbf{j}(\mathbf{r},t) | \psi' \rangle \tag{5.26b}$$

$|\psi'\rangle$ represents wavefunction of the system at time t and it evolves with time as:

$$|\psi'\rangle = S(-\infty, t)|\psi\rangle \tag{5.27}$$

$|\psi\rangle$ denotes the wavefunction of the system when no field is applied. For very small external fields, the S matrix is expanded to the linear term of H', yielding

$$S(-\infty, t) = \left[1 - i/\hbar \int_{-\infty}^{t} dt' H'(t')\right] + \cdots \tag{5.28}$$

Then the current $\mathbf{J_2}$ can be expressed as a commutator:

$$\mathbf{J}_2(r,t) = -i/\hbar \int_{-\infty}^{t} dt' \langle \psi | [\mathbf{j}(\mathbf{r},t), H'(t')] | \psi \rangle \tag{5.29}$$

Expressing H' in terms of the electrical field and the vector potential, one obtains

$$\mathbf{J}_2(r,t) = \frac{1}{\omega} \int_{-\infty}^{t} dt' e^{i\omega(t-t')} \langle \psi | [\mathbf{j}(\mathbf{r},t), \mathbf{j}(\mathbf{q},t)] | \psi \rangle \mathbf{E}(\mathbf{r},t) \exp(-i\mathbf{q}\cdot\mathbf{r}) \tag{5.30}$$

Now one has the expression for each conductivity component in terms of the current-current commutator

$$\sigma_{\alpha\beta}(\mathbf{q},\omega) = \frac{1}{\omega} \int_{-\infty}^{t} dt' e^{i\omega(t-t')} \left\langle \psi \middle| \left[\mathbf{j}_\alpha^+(\mathbf{q},t), \mathbf{j}_\beta(\mathbf{q},t') \right] \middle| \psi \right\rangle + \frac{n_0 e^2}{m\omega} i\delta_{\alpha\beta} \tag{5.31}$$

This equation is the Kubo formula for conductivity which is fundamental in calculating the conductivity or conductance.

It is desirable to have the expression for conductivity or conductance in terms of eigenvalues and eigenfunctions of the Hamiltonian which describes the disordered system(Fisher,D.S. and Lee, 1981). If the system is isotropic, $\sigma_{\alpha\beta} = \sigma\delta_{\alpha\beta}$ and the real part of conductivity can be written as:

$$\mathrm{Re}(\sigma)=\frac{1}{\omega}\int_0^\infty dt e^{i\omega t}\langle\psi|[j(q,t),j(q,0)]|\psi\rangle \qquad (5.32)$$

The expectation value of the current-current commutator is expressed in terms of eigenfunctions of H_0 at finite temperature T (T=0 is obtained by taking the limit $\beta=1/kT\to\infty$). The expectation of the commutator is

$$\frac{1}{Z}\sum_{m,n}\left(e^{-\beta E_m}-e^{-\beta E_n}\right)\left|\langle m|j(q)|n\rangle\right|^2 e^{-i(E_m-E_n)t/\hbar} \qquad (5.33)$$

where $|m\rangle$ and $|n\rangle$ are eigenfunctions of H_0 with eigenenergies E_m and E_n respectively. Z is partition function given by

$$Z=\sum_m e^{-\beta E_m} \qquad (5.34)$$

Integration over t in equation (5.32) gives

$$\mathrm{Re}(\sigma)=\frac{\pi}{\omega Z}\left(1-e^{-\beta\omega}\right)\sum_{m,n}e^{\beta E_m}\left|\langle m|j(q)|n\rangle\right|^2\delta(\omega-E_n+E_m) \qquad (5.35)$$

Now we consider the disorder system of size L with two ends attached to two perfect leads. The current flows along the z-direction

$$J(z)=\int d^{d-1}x j(x) \qquad (5.36)$$

j(p) is the Fourier component of j(x) thus as q→0

$$j(0)=\frac{1}{L^{d/2}}\int_0^L dz J(z) \qquad (5.37)$$

Finally one takes the limit of β→∞

$$\mathrm{Re}(\sigma)=\frac{\pi}{\omega L^d}\int dE'\sum_{m,n}\left|\int_0^L dz\langle m|J(z)|n\rangle\right|^2\delta(E'-E_m)\delta(E'+\omega-E_n) \qquad (5.38)$$

The dc conductivity is attained by taking the limit of ω=0. This expression directly relates the conductance to the

eigenvalues and eigenfunctions and is our starting point in doing numerical calculations in section 5.3.

5.2.2 Landauer's formula and transfer matrices:

The calculation of conductance in one dimension is greatly simplified by the formula which expresses the conductance of a system of random elastic scatterers in terms of scattering properties at a fixed energy. The formula is called Landauer's formula(Anderson,P.W. etc., 1980; Azbel,1980) written as:

$$\Gamma = \frac{e^2}{2\pi\hbar}\frac{T}{R} \tag{5.39}$$

where R and T are reflection and transmission coefficients respectively. Therefore if one knows the scattering matrix, the conductance can be easily computed. The formula can be derived rigorously in one dimension, however, the extension to higher dimensions seems unclear. For multiple-channel scattering, the generalized Landauer formula proposed by Anderson etc.(Anderson,P.W.etc.,1980; Buttiker,1986) takes the form

$$\Gamma = \frac{e^2}{2\pi\hbar}\frac{\sum_{ij}|t_{ij}|^2}{1-\sum_{j}|t_{ij}|^2} \tag{5.40}$$

When the channel number n is large, $t_{ij}\sim 1/n^2$, thus

$$\Gamma_{n\to\infty} = \frac{e^2}{2\pi\hbar}\mathrm{Tr}(tt^*) \tag{5.41}$$

This expression is accurate for strong scattering. Therefore, it may be advantageous to compute the transfer

matrix first and then conductance can be fairly easily obtained. As shown below, the transfer matrix can be calculated column by column so this algorithm scales as L while the matrix size of the Green's function method is L^2.

Now let's consider in more detail about the propagation of the wave function. We still consider the disordered region to be attached with two perfect leads of infinite length. Let ψ_i be the wavefunction at the i-th column of the disordered region. The tight binding model has the following recursion relation:

$$H_i\psi_i = V_i\psi_{i+1} + V_{i-1}\psi_{i-1} \tag{5.42}$$

where H_i is the diagonal matrix of column i and V_i is the connection matrix between column i and i-1. This is equivalent to:

$$\begin{pmatrix} \psi_{i+1} \\ \psi_i \end{pmatrix} = \begin{pmatrix} V_i^{-1}H_i & -V_i^{-1}V_{i-1} \\ I & 0 \end{pmatrix} \begin{pmatrix} \psi_i \\ \psi_{i-1} \end{pmatrix} \tag{5.43}$$

The above expression gives the relationship between two consecutive column wavefunctions. Then the transfer matrix T is simply expressed as:

$$T = \begin{pmatrix} V_i^{-1}H_i & -V_i^{-1}V_{i-1} \\ I & 0 \end{pmatrix} \tag{5.44}$$

In order to get conductance, the transfer matrix has to be converted into a scattering matrix S(Anderson,P.W.,1981). The conversion utilizes the relationship: $S = U^{-1}TU$ where U is a unitary matrix and is determined by the Fermi energy level.

5.3 Numerical Calculations:

In the section, I will use the Kubo's formula(Equation 5.38) for conductance to calculate the conductance of a 2-d diluted square lattice which is described by the Hamiltonian:

$$H = \sum_{j,k} V^x_{jk} a^+_{j+1,k} a_{j,k} + V^y_{jk} a^+_{j,k+1} a_{j,k} + c.c. + \sum_{j,k} E_{jk} a^+_{jk} a_{jk} \qquad (4.45)$$

where j and k are position indeces in the x and y directions respectively and E_{jk} are site energies. In the bond percolation model, V^x_{jk}, V^y_{jk} are hopping constants which are one when a bond exists and 0 otherwise and E_{jk} are constant. In site percolation case, E_{jk} are either infinite for absent sites and zero for present ones. For a finite system of scale L, the Hamiltonian is a $L^2 \times L^2$ matrix expressed as following:

$$H = \begin{pmatrix} H_{11} & H_{12} & \cdots & H_{1L} \\ H_{21} & H_{22} & \cdots & H_{2L} \\ \vdots & \vdots & \ddots & \vdots \\ H_{L1} & H_{L2} & \cdots & H_{LL} \end{pmatrix} \qquad (5.46)$$

where each H_{mn} is an L×L matrix with H_{mm}, $H_{m,m\pm1}$ being non-zero only if the nearest neighbor hopping is considered. We start with the expression for the conductance of an L×L lattice at frequency ω. Equation (5.38) becomes:

$$G(\omega) = \frac{\pi}{\omega L^2} \int dE' \sum_{\alpha,\beta} \left| \sum_j \langle \alpha | J(j) | \beta \rangle \right|^2 \delta(E' + \omega - E_\beta) \delta(E' - E_\alpha) \qquad (5.47)$$

where E_α, E_β are the eigenvalues of H with $E_\alpha < E < E_\beta$ where E is the Fermi energy and $|\alpha\rangle, |\beta\rangle$ are the corresponding eigenvectors. Following P.A.Lee etc. (Lee and Fisher,D., 1982), one introduces the Green's functions $G^{\pm} = (E - H \pm i\eta)^{-1}$ where η is a small positive number. The imaginary part of the Green's Function is $G = (G^{-} - G^{+})/2i$. E_α and $|\alpha\rangle$ are eigenvalues and eigenvectors of H respectively:

$$H|\alpha\rangle = E_\alpha|\alpha\rangle \tag{5.48}$$

and in terms of the Green's functions:

$$|\alpha\rangle = G^{\pm}(E - E_\alpha \pm i\eta)|\alpha\rangle \tag{5.49}$$

Taking the imaginary parts of both sides gives:

$$G|\alpha\rangle = \frac{\eta}{(E - E_\alpha)^2 + \eta^2}|\alpha\rangle \tag{5.50}$$

As $\omega \to 0$, the continuity of current requires $J(j)$ ought to be independent of j, thus summation over j is trivially done, yielding $L^2|\langle\alpha|J(j)|\beta\rangle|^2$. Noticing that

$$\lim_{\eta \to 0} \frac{\eta}{(E - E_\alpha)^2 + \eta^2} = \pi\delta(E - E_\alpha) \tag{5.51}$$

One employs the stepfunction f(x) to eliminate the restriction: $E_\alpha < E' < E_\beta$

$$\begin{aligned}\Gamma(\omega) &= \frac{1}{\pi}\int dE' \frac{f(E - E' + \omega) f(E' - E)}{\omega} \sum_{\alpha,\beta} \langle\alpha|JG|\beta\rangle\langle\beta|JG|\alpha\rangle \\ &= \sum_{\alpha} \langle\alpha|JGJG|\alpha\rangle \end{aligned} \tag{5.52}$$

The current operator $J(j)$ of jth column is expressed as:

$$J(j) = ie\sum_{k} V_{jk}(a^{+}_{j,k}a_{j-1,k} - c.c) \tag{5.53}$$

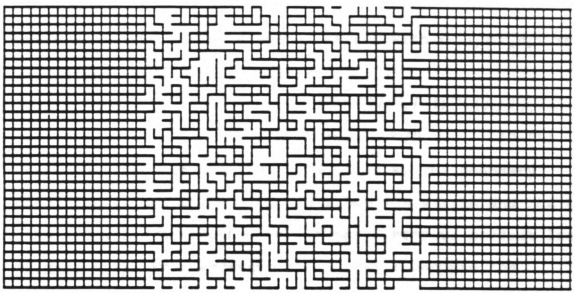

Figure 5.1: A 32×32 percolation square lattice embedded in a perfect square lattice belt of with 32 and infinite length with p=0.6 in the percolation structure. All the data in Chapter five are based on the model shown in the picture. The adjustable parameters are p and system size L.

one views the current operator to be a matrix of $2L \times 2L$(Lee and Fisher,1982):

$$J(j) = \begin{pmatrix} 0 & ieV_j^x \\ -ieV_j^x & 0 \end{pmatrix} \qquad (5.54)$$

where V_j^x is the vortex diagonal matrix with $(V_j^x)_{kl} = V_{jk}^x \delta_{lk}$. The conductance at ω=0 is simplified to:

$$\Gamma(0) = e^2 / \pi \mathrm{Tr}[G(j,j)V_j^x G(j-1,j-1)V_j^x + G(j-1,j-1)V_j^x G(j,j)V_j^x$$
$$-G(j,j-1)V_j^x G(j,j-1)V_j^x - G(j-1,j)V_j^x G(j-1,j)V_j^x] \qquad (5.55)$$

where the trace is over the site index k. The boundary condition is set to be periodic along the y-axis and the two ends x=0,x=L are attached to two semi-infinite perfect leads (Figure 5.1). From equation (5.55), to calculate the conductance, one only needs to know G(j,j), G(j-1,j-1) and G(j,j-1). To avoid a huge matrix representation the recursive method is utilized. We start with a perfect lattice with width L and semi-infinite length. We define the left Green's Function $G^l(j) \equiv G^l_{kk'}(j,j)$ with the columns of j'>j absent. $G^l(j)$ has the following matrix recursion relationship:

$$G^l(j)^{-1} = G^0(j)^{-1} - V_j^x G^l(j-1) V_j^x \qquad (5.56)$$

where $G^0(j)$ denotes the Green's function for the isolated jth column. Similarly, one could define the right Green's function $G^r(j)$ with all the columns of j'<j absent. The Green's function of the jth column which connects the $(j-1)$

th column from left and the (j+1)th column from the right is written as:

$$G(j,j)^{-1} = G^0(j)^{-1} - V^x_{j+1}G^r(j+1)V_{j+1} - V^x_{j-1}G^l(j-1)V^x_{j-1} \qquad (5.57)$$

and G(j-1,j) can be obtained from G(j-1,j-1) through:

$$G(j-1,j) = G(j-1,j-1)V^x_j G^r(j) \qquad (5.58)$$

First, $G^1(0)$, the left Green's function for a semi-infinite perfect lattice is computed. To find $G^1(0)$, one just needs to solve the matrix equation

$$G^l(0)^{-1} = G^0(0)^{-1} - G^l(0) \qquad (5.59)$$

because V^x_j turns out to be a unit matrix. Because $G^0(0)$ and $G^1(0)$ have the same matrix form, the transfer matrix T which leads to the diagnalization of $G^0(0)$ happens to diagonalize the matrix $G^1(0)$ also. The eigenvalues and corresponding eigenvectors for $G^0(0)$ are easily obtained and so that one has the eigenvalues of $G^1(0)$ from the simple second order equation.

$$\frac{1}{\lambda} = \frac{1}{\lambda^0_i} - \lambda \qquad (5.60)$$

where λ^0_i denotes the eigenvalues of $G^0(0)$. $G^1(0)$ is calculated from $G^l(0) = T^{-1}\Lambda T$, where Λ is the eigenvalue matrix of $G^1(0)$.

Once $G^1(0)$ has been calculated, one can build the disordered region onto the semi-infinite perfect lattice according to equation (5.56). After the L-th column has been attached, another semi-infinite perfect lattice is attached.

The Green's functions G(L,L), G(L-1,L-1) and G(L-1,L) are obtained through the recursion relationship described above.

5.3.1 Quantum percolation threshold:

The threshold for classical bond percolation is known to be p_c=0.5 for a two dimensional square lattice. The quantum threshold p_Q is defined as the p value below which all quantum states are localized. Obviously due to electronic back scattering, it is expected that $p_Q > p_c$. The scaling theory of localization predicts that any finite degree of disorder will result in all electronic states being localized, i.e. p_Q=1.

It is noticed that if we apply the expression (5.55) to calculate conductance, we always obtain finite values even for a perfect lattice. Our calculation shows that $g(1,L)=L$, the system width. Thus, p_Q is determined from calculating the conductance as a function of system size L at a fixed disorder quantified by p. We performed the calculation of g(p,L) as a function of L at fixed p values(see Figure 5.2). The results show that if p is very close to 1, g(p,L) increases with L for small system size and reaches a maximum at $L=L_M$, and starts to decrease monotonically with L for $L>L_M$. When p is not very close to 1(p=0.95 or less), g(p,L) is simply monotonically decreasing with the system size that we chose. In other words, L_M decreases as p increases. The point is that even for a very small disorder(p=0.98),

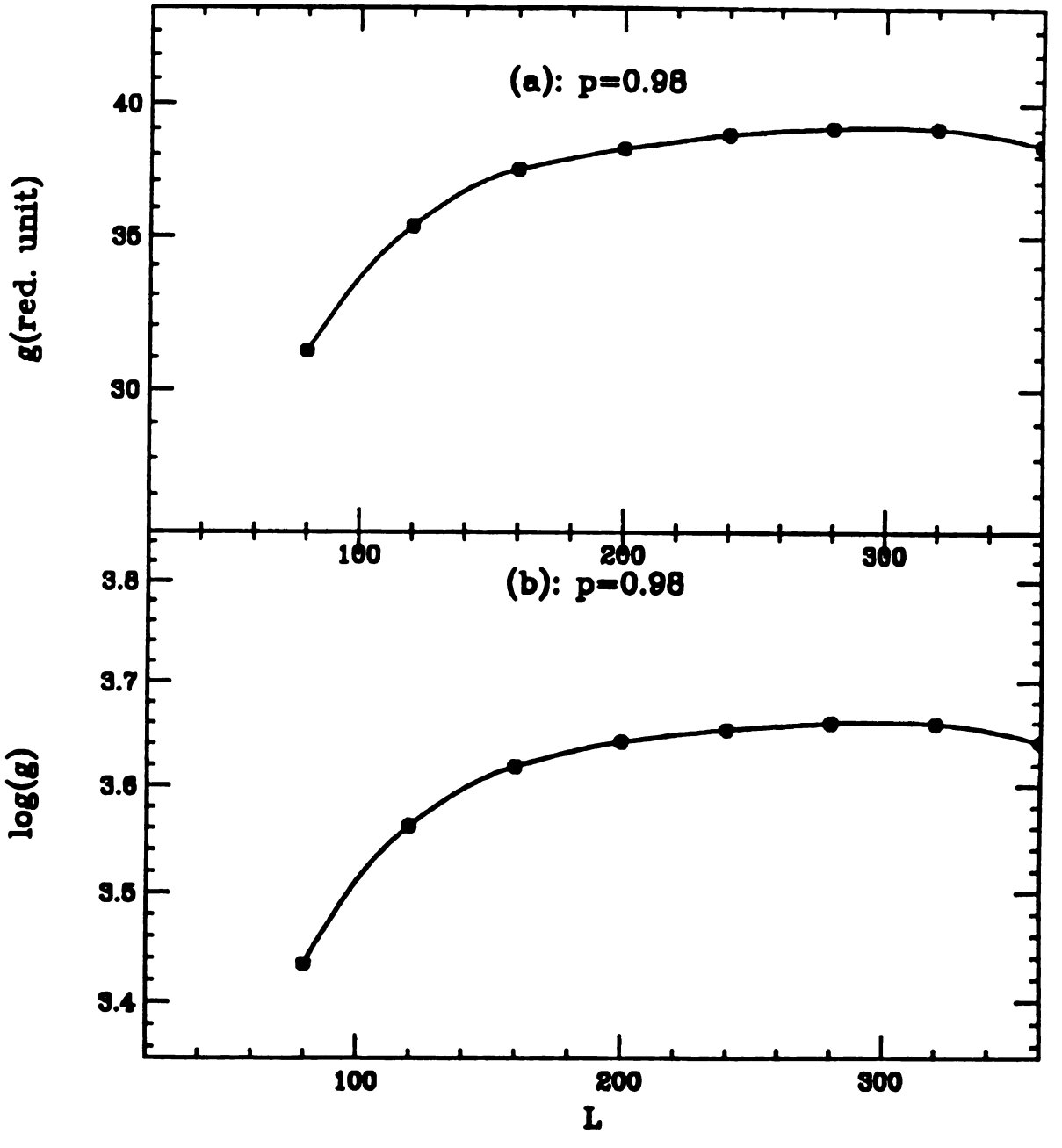

Figure 5.2: The reduced conductance g as a function of system size. 8 different sizes are considered. p is fixed at 0.98. Each point is an average over 200 configurations. The conductance g increases with L first and reaches a maximal value at L=280, then starts to decrease. It corresponds to the crossover from a "scattering" region to the weak localization region.

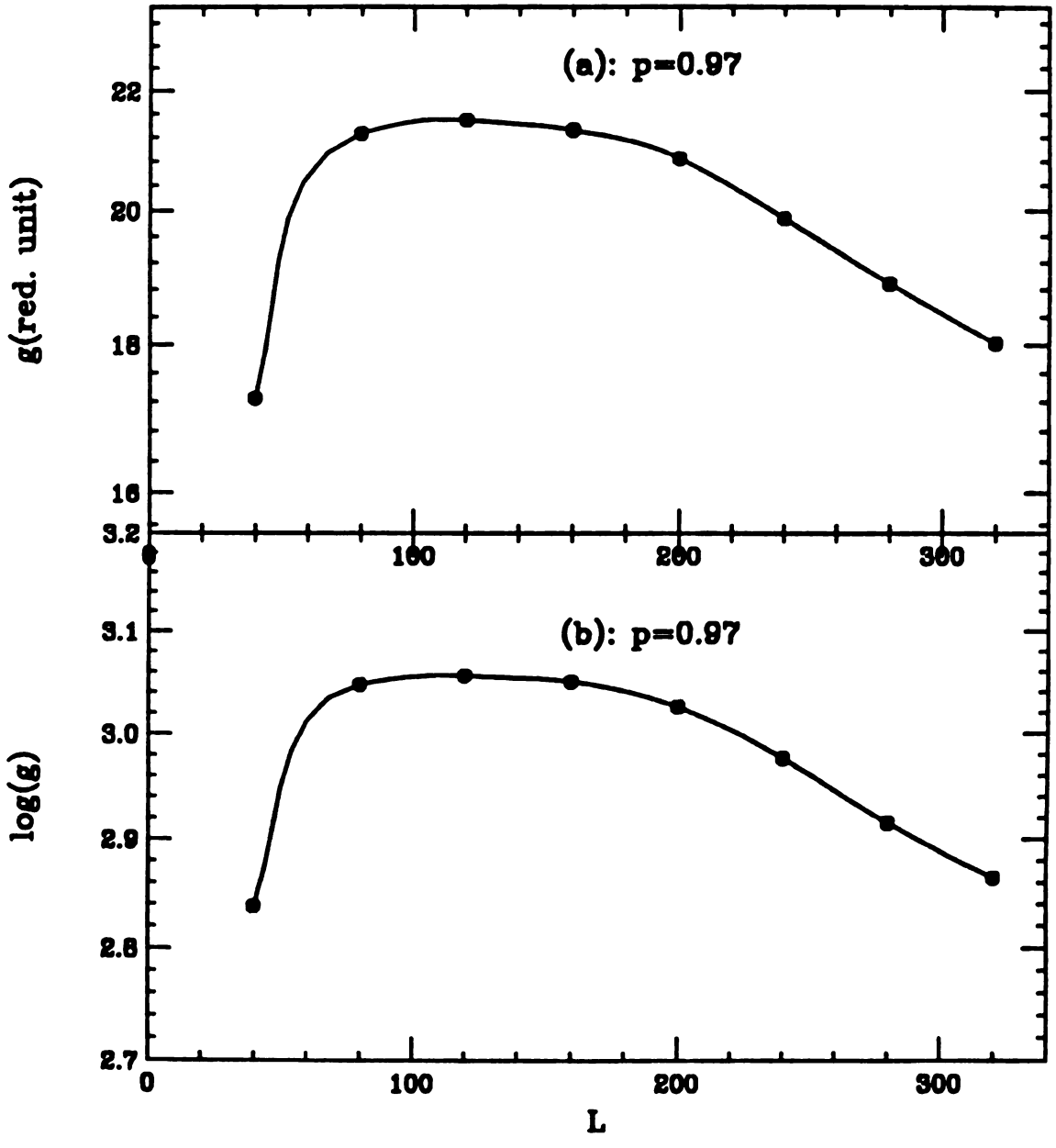

Figure 5.3: A similar plot to Figure 5.2 except that the calculation is done for site percolation. The p value is fixed at 0.97 and again each point is obtained from taking an average over 200 samples. g increases with L first but it reaches a maximum at L=120 and starts to decrease.

g(p,L) will eventually decreases with L monotonically. Figure 5.2 shows the numerical results of g(p,L) of a bond percolating lattice. Each point in the plot is an average over 200 configurations. A similar behavior is seen in Figure 5.3 which is the result from calculations carried out on a site percolating square lattice. As will be shown in the next subsection, g(p,L) decreases exponentially with L when the system size is sufficiently large, for finite p. Therefore, it is clear that the quantum threshold for a 2-dimensional square lattice is 1; any finite disorder(site or bond) will result in the localization of electronic states.

5.3.2 Scaling of conductance:

The heart of the scaling theory of localization is the one-parameter assumption that the scaling function depends on g only. In this subsection, our objective is to perform a detailed calculation of g(p,L) and the β function and to analyze their behaviors in several distinct regions.

Figure 5.4 shows a log-linear plot of g(p,L) as a function of p. g(p,L) monotonically decreases with decreasing p, it is not difficult to divide the figure into three regions. In region (I): $\ln g(p,L)$ decreases rapidly, a very small decrement in p results in a big change in g. We call this the scattering region because when (1-p) is small the defects are very sparse and the mean free path exceeds the system size L. In region (II): g(p,L) starts to degrade

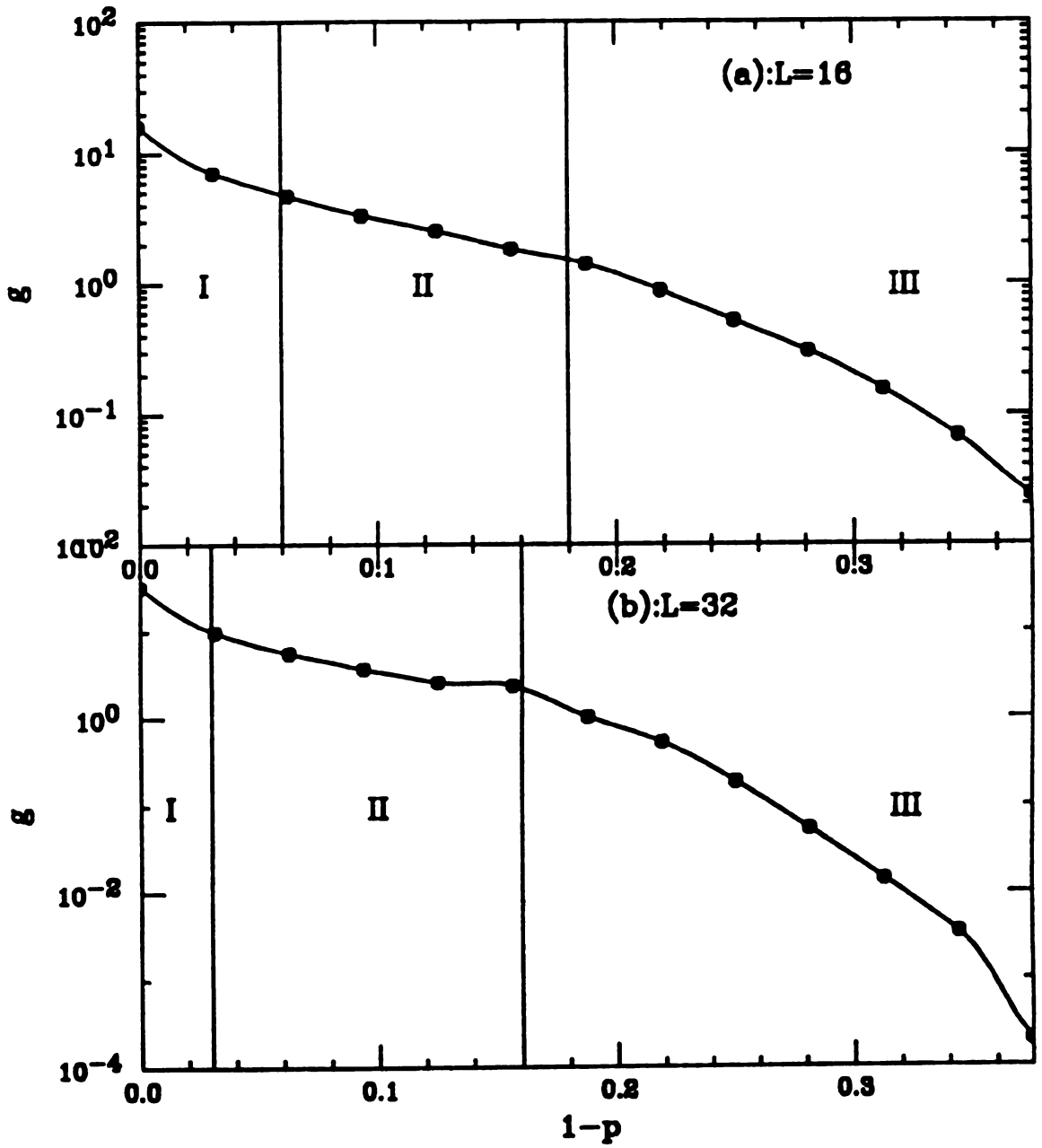

Figure 5.4: A log-linear plot of g as a function of p at fixed system size. Three distinct regions are classified: region (I) is very narrow in which g decays very fast, it crosses over to region (II) at p=0.05. Region(II) is the weak localization region in which g decays relatively slowly and g decreases as L increases. As more bonds are removed, g enters the strong localization region, region (III) in which g decays much faster than in region (II).

slowly and it is called the weak localization region. Finally in region (III): g(p,L) decreases very rapidly once again. This corresponds to the strong localization region. Our analysis is based upon the calculations of g(p,L)(or $\ln g(p,L)$) in those regions. Let p_{c1} and p_{c2} be the points separating those regions. In general, p_{c1} and p_{c2} depend on system size. A more precise definition of p_{c1} and p_{c2} is as follow.

For a particular L, p_{c1} is defined as

$$\frac{\partial g(L,p_{c1})}{\partial L}=0 \qquad (5.61)$$

When the impurity concentration is very small, the mean free path of electron scattering is much larger than the system size L. It has been shown that a single defect will cause a decrement in conductance by order of unity in that limit. By noting that the conductance g is proportional to the system size L when p=1, we have the following scaling form:

$$g(p,L)\sim L-a(1-p)L^2 \qquad (5.62)$$

with parameter a being of order of one. Therefore p_{c1} can be roughly obtained as a function of L:

$$1-p_{c1}\sim 1/L \qquad (5.63)$$

as $L\to\infty$, $p_{c1}\to 1$. In the region $p>p_{c1}$, g increases as L increases, so β is positive, which contradicts the scaling theory of localization, which predicts non-positivity of β in 2-dimensional disorder systems. It should be pointed here that the scattering region is not physically reasonable as

it fails to yield an infinite conductance for a perfect system.

In the weak localization region, g is monotonically decreasing with L, and the β function is negative. We varied the p values and calculated the conductance g as a function of system size. An attempt has been made to fit the data to the equation $g(L) = g_0 - c\ln(L/L_0)$ and the data fits the curve reasonably well as shown in Figure 5.5. It implies that the β-function scales as

$$\beta = -a/g \qquad (5.64)$$

Where the parameter a is equal to the slope of the line in Figure 5.5. The result is perfectly consistent with perturbation theory.

In region (III), g(L) crosses over to a strong localization region. Care must be taken when calculating the conductance as g becomes extremely small when p approaches p_c, so that the η factor in the Green's function(Equation (5.49)) starts to play a significant role in the numerical calculations. Generally, small g requires small η. Figure 5.6 presents the results on conductance for relatively large disorder. The logarithmic function of g(p,L) was plotted against system size L, showing the linear dependence between them. The slope of the line is dependent on disorder alone.

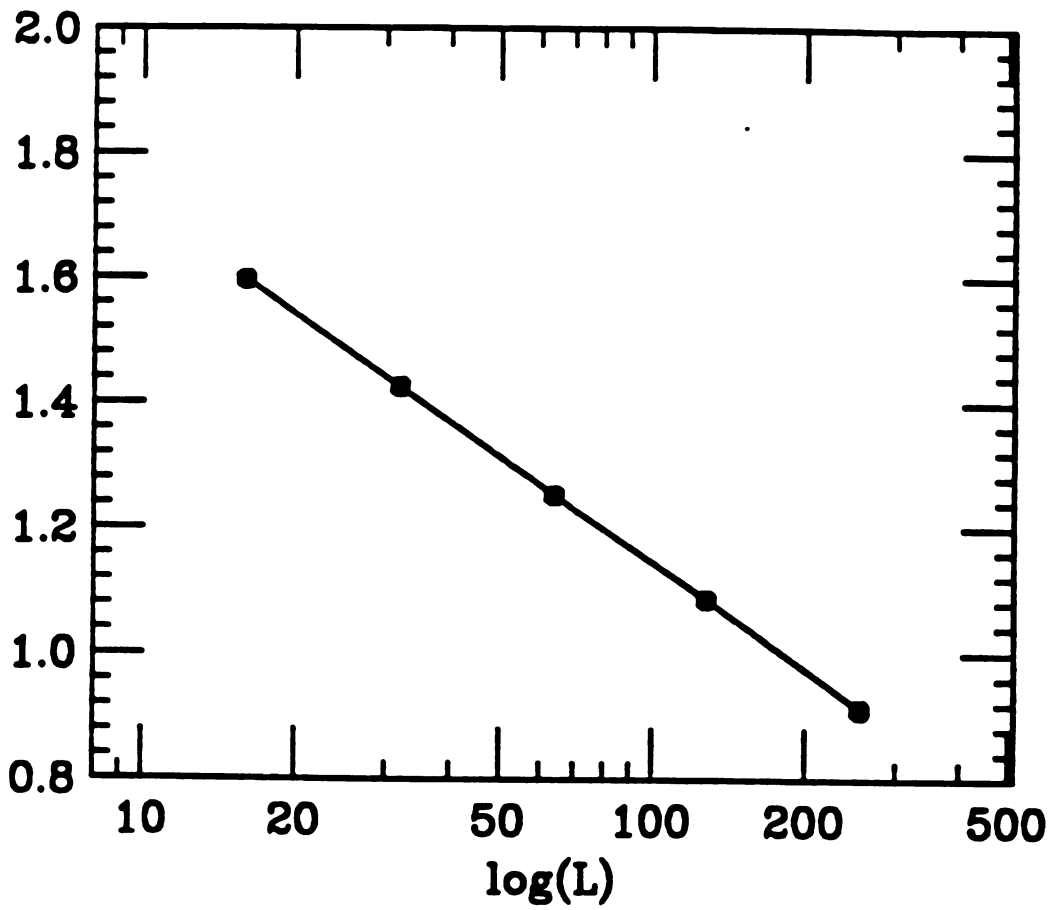

Figure 5.5: Linear-log plot of g as a function of system size L, showing the behavior of g in the weak localization region. In the graph I have taken p=0.075 and the system sizes are chosen: L=16, 32, 64, 128, 256. The data for L=256 is from 100 configurations and the rest of data are from a 200 sample average. It shows nearly a perfect linear relationship.

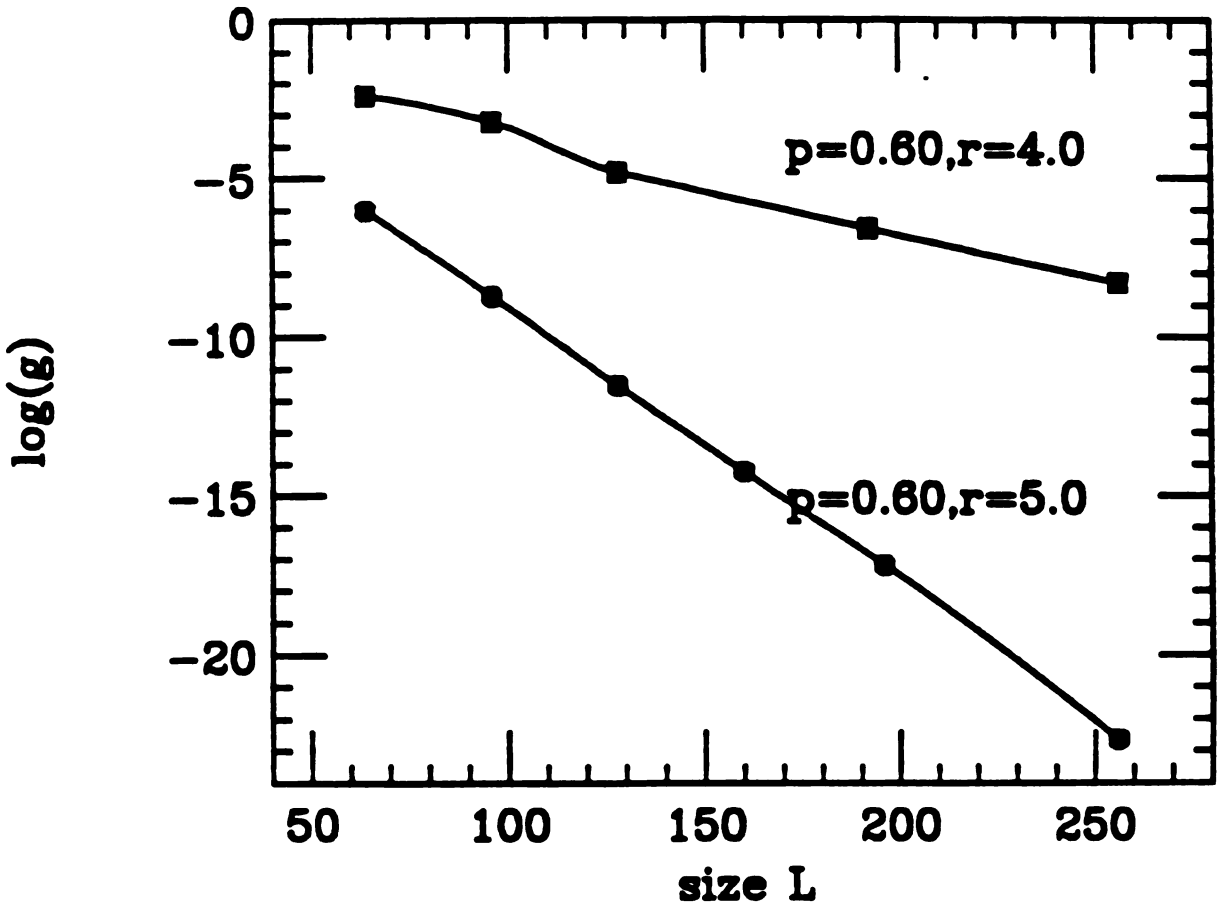

Figure 5.6: A log-linear plot of g as a function of L. It corresponding to the strong localization region. The calculation was done for the site percolation case where p is taken as 0.60. r stands for the energy level for an absent site while r=0 for any present site. The upper curve has a little deviation from linear dependence while the lower curve shows a nice straight line as predicted from strong localization.

5.3.3 Conductance distribution:

The distribution of conductance has been investigated first by B. Sharpiro(Sharpiro, 1986,1987) and coworkers based on the concept that two quantum resistors ρ_1 and ρ_2 in series have the total resistance:

$$\rho = \rho_1 + \rho_2 + 2[\rho_1\rho_2(1+\rho_1)(1+\rho_2)]^{1/2}\cos\theta = u(\rho_1,\rho_2,\theta) \qquad (5.65)$$

where θ is the phase angle between ρ_1 and ρ_2. Suppose the distributions of ρ_1 and ρ_2 are known and denoted by P(ρ) and P(ρ), the distribution of ρ under condition $\rho = u(\rho_1,\rho_2,\theta)$ is given by:

$$P(\rho) = \frac{1}{\pi}\int d\rho_1 d\rho_2 d\theta P_1(\rho_1)P_2(\rho_2)\delta(\rho - u) \qquad (5.66)$$

Assume that ρ_1 and ρ_2 have linear scales ΔL and L respectively with ΔL being small and thus small ρ_1, one expands the above expression up to linear terms of ρ_1, yielding:

$$P_{L+\Delta L}(\rho) = P_L(\rho) + \langle\rho_1\rangle\left[\frac{\partial}{\partial\rho}(\rho+\rho^2)\frac{\partial P_L(\rho)}{\partial\rho}\right] \qquad (5.67)$$

where $\langle\rho_1\rangle$ is the average value of ρ_1 and has been assumed to be linearly dependent on ΔL as it is small. Let $\alpha = \langle\rho_1\rangle/\Delta L$, one obtains a diffusion like equation:

$$\frac{\partial P_L(\rho)}{\partial L} = \alpha\left[\frac{\partial}{\partial\rho}(\rho+\rho^2)\frac{\partial P_L(\rho)}{\partial\rho}\right] \qquad (5.68)$$

$P_L(\rho)$ can be easily solved for two limits of $\rho\to 0$ and $\rho\to\infty$. The former limit implies that the ρ^2 term can be neglected and thus the solution is written as:

$$P_L(\rho) = \frac{1}{\alpha L}\exp(-\rho/\alpha L) \qquad (5.69)$$

The average of ρ yields <ρ>=αL, recovering Ohm's law. When ρ >>1, $\rho^2+\rho\cong\rho^2$, (5.68) turns into a diffusion equation and the solution reads:

$$P_L(\rho)=\frac{1}{\sqrt{4\pi\alpha L}}\exp[-(\ln\rho-\alpha L)^2/4\alpha L] \qquad (5.70)$$

In this case, the average of lnρ depends linearly on L. Both distributions support the single-parameter scaling theory assumption.

The conductance distribution in two dimensions is difficult to find because of the traverse scattering. Many techniques such as the "fan transformation"(P.W.Anderson, 1980) and a Kadanoff type scaling transformation are employed to generalize the one dimensional result. Here we directly calculated the distribution of conductance and found the distribution is log-normal when g is very small as expected. Figure 5.7 shows a typical distribution for a strongly disordered system and the curve fits a gaussian distribution well. But for medium disorder, the distribution is anomalous and of bimodal structure. Figure 5.8 is the distribution for a 16×16 square lattice with p=0.75. The statistics was done for some 4000 samples. Clearly, the graph shows that P(g) has two maxima: one is located near g=1 and the other is close to g=0. When disorder is small, the peak near g=0 is not seen. The peak near g=1 decreases as disorder increases and will eventually disappear,

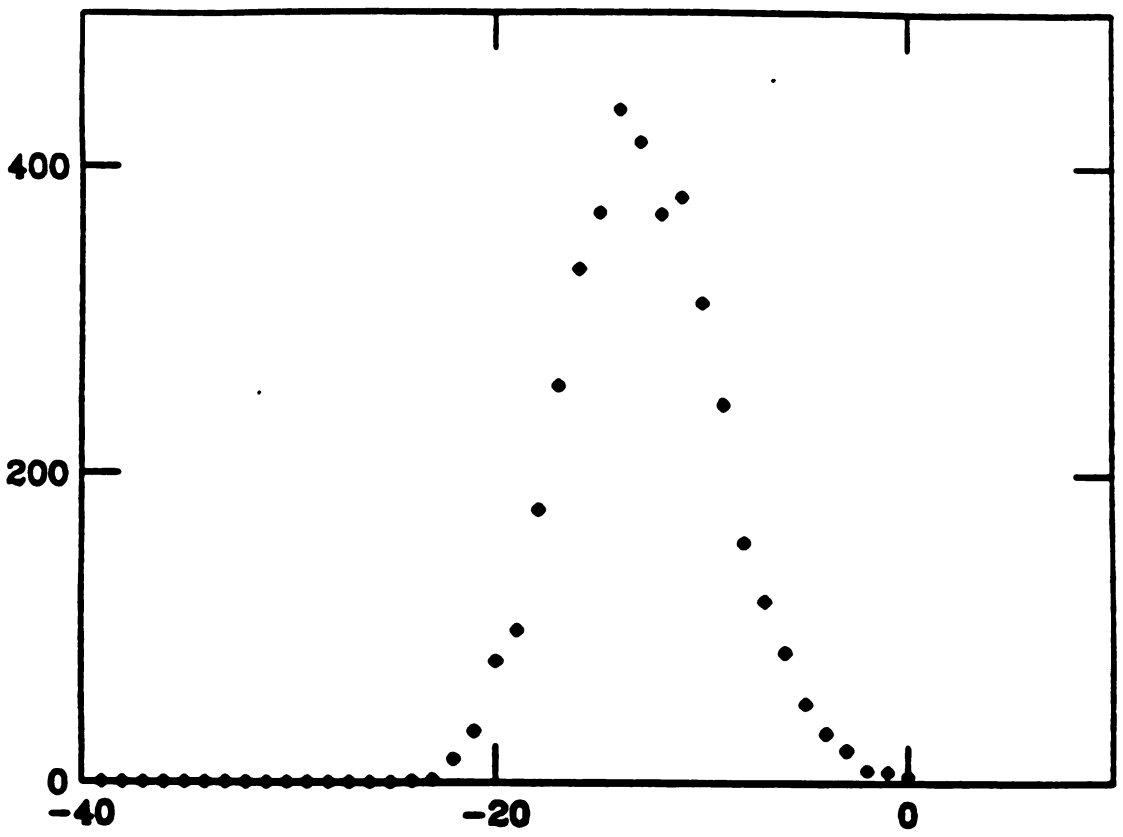

Figure 5.7: Distribution of g: strong localization limit. The statistics was for 4000 configurations. L is fixed at 32, and p is fixed at 0.40. The x-axis is log(g) and y coordinate represents the number. The peak is located near log(g)=-15. The overall shape can be fitted closely to a gaussian curve.

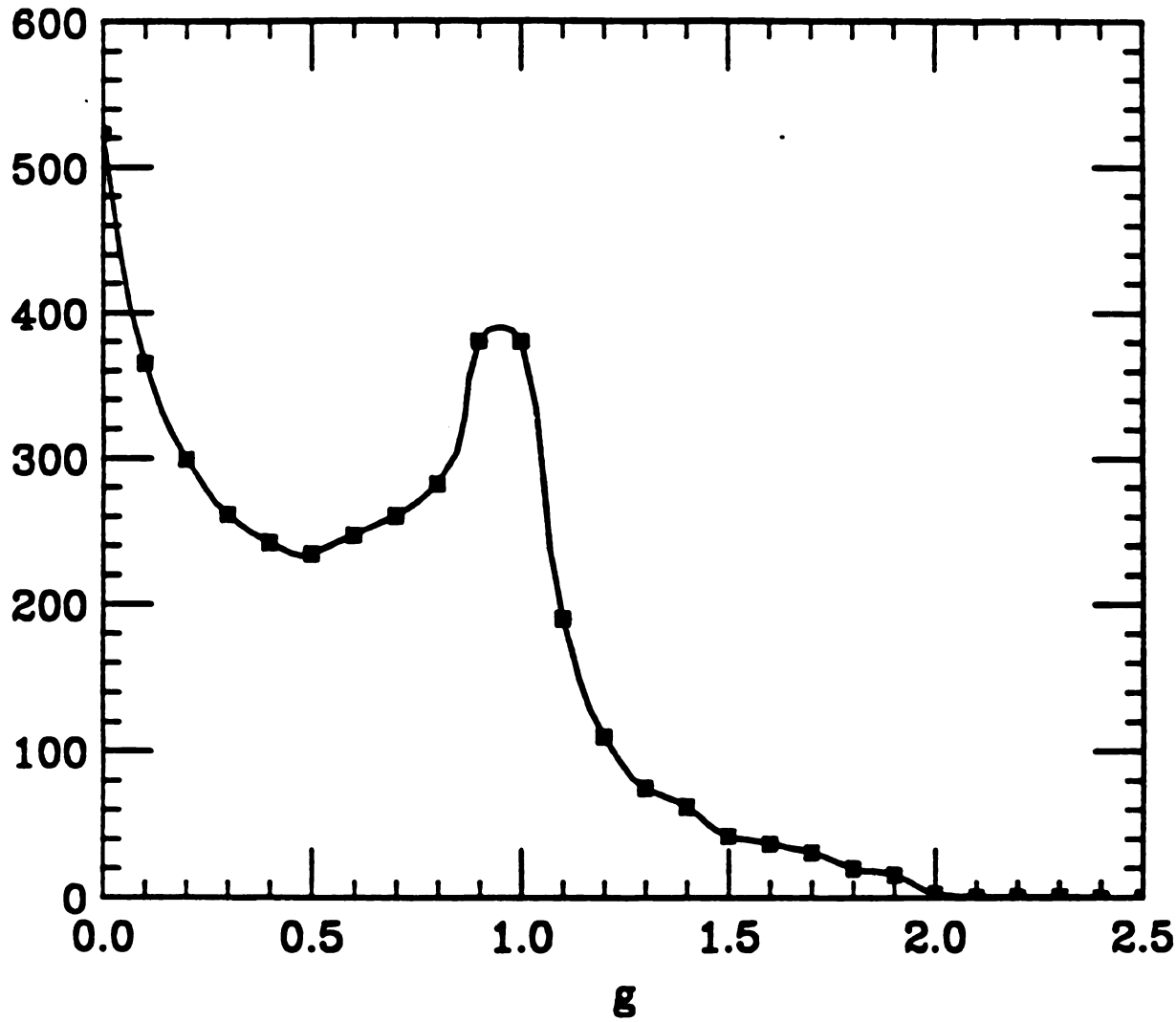

Figure 5.8: Distribution of g: medium degree of disorder. Here the sample number is 4000 again, system size L=16. p=0.25. I have taken a finite hopping constant x=0.1 instead of 0 for an absent bond to avoid floating number underflow. It is clear that two maxima show up: one is near 0, the other is near g=1.0. The bimodal feature leads to a difficulty in taking averages. If log(g) is averaged, the contribution from g near 0 dominates; if g is averaged, the contribution from g=1 dominates.

merging into the strong localization case. So far, we do not have physical explanation for this bi-modal structure.

5.5 Discussions and Open Questions:

It is interesting to study the scaling behavior of conductance of a lattice near its classical percolation threshold p_c, where the backbone of the lattice structure is fractal. It has been discovered that diffusion on a fractal structure exhibits abnormal behavior and the diffusion constant D algebraically decays with distance r as discussed in section 5.1.2. About half a decade ago, several authors(Shapir and Aharony,1982;Levy and Souillard,1987; Lambert and Hughes,1991) studied quantum diffusion on a fractal structure using scaling arguments and introduced the concept of super-localization in contrast to the localization behavior discussed earlier. Super-localization claims that the electronic wavefunction on a fractal structure decays faster than exponential against distance and typically satisfies the following scaling form:

$$\psi(r) \sim \psi(0)\exp[-(r/\xi)^a] \qquad (5.71)$$

with a>1. This implies that the conductance g of a fractal structure has a similar scaling with its size L. Because the conductance is directly related to the electronic wavefunctions, it is very desirable to carry out a systematic numerical calculation of conductance to verify

this relationship. It is noticed that near the percolation point, the conductance is extremely small due to fewer connected points, so in order to obtain reliable calculation results, the hopping elements in the Hamiltonian are set to be either 1 or a small finite number. This procedure will certainly effect the consequences of calculations but it does not effect the scaling behavior as no structural change has been made. The two dimensional lattice sizes are selected to be L=16, 32, 48, 64, 80, 96,112, 128, 144,160. The conductance log(g) as a function of L is plotted in Figure 5.9, showing a linear dependence as predicted from strong localization. It should be pointed out that because of the introduction of a small hopping constant, the result shows a normal localization behavior. More detailed calculation needs to take the small hopping constant as small as possible. Unfortunately, our method cannot handle the situation well due to computer rounding error. One appealing method is to utilize the transfer matrix approach discussed in section 5.2. It remains a prospective project in the near future.

To conclude, we have calculated the conductance of a 2d percolation lattice as a function of system size and p value. Our calculation results strongly support the scaling theory of localization.

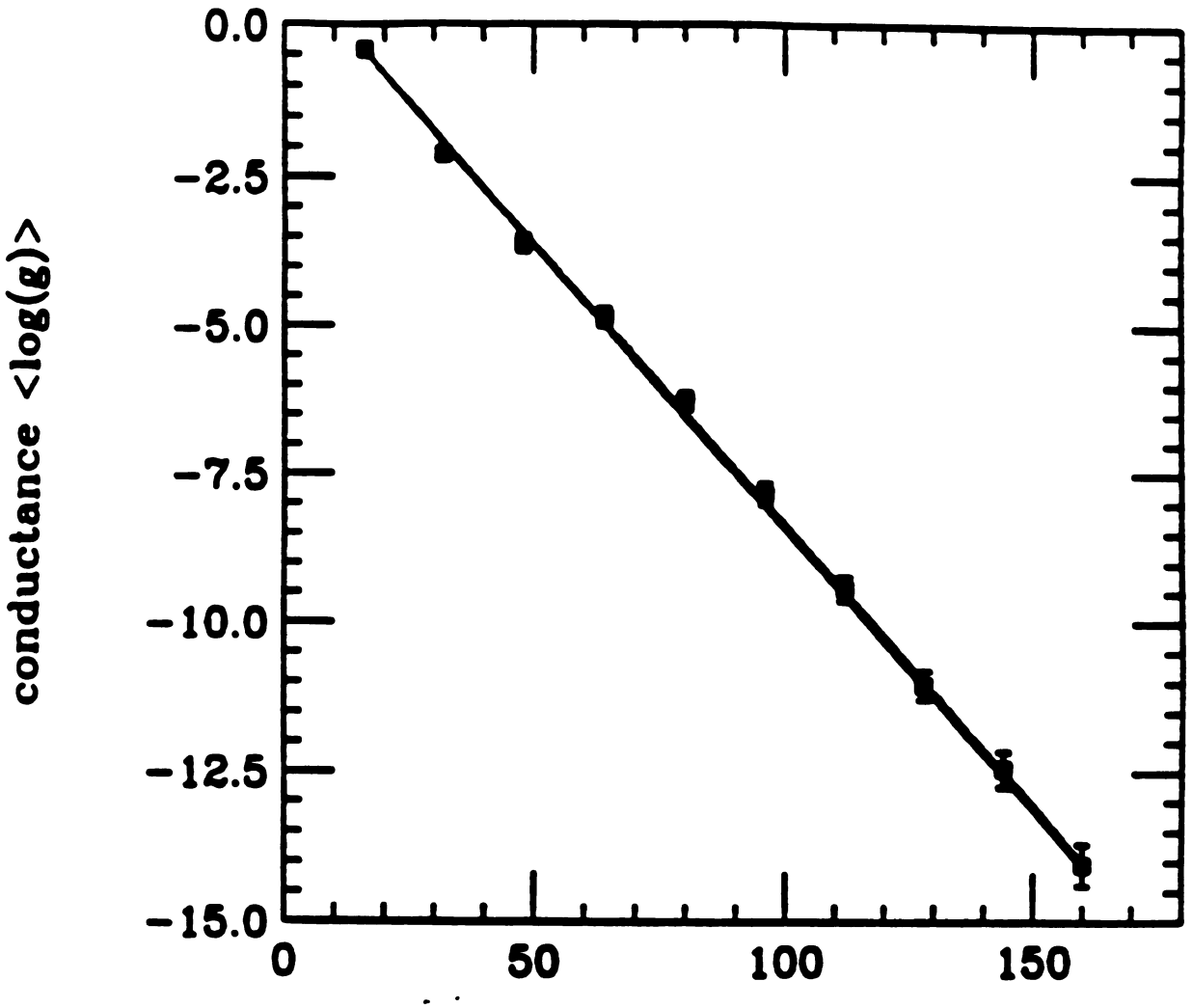

Figure 5.9: Log-linear plot of g as function of L at percolation point p=0.5. To avoid singularities, the hopping constant for an absent bond has been taken to be 0.1. Each point in the figure is an average of 400 configurations. We wish to see a super-localization behavior equation (5.71). Instead, it shows clearly a linear dependence, as predicted from strong localization.

Final Remarks: In the final section, I will provide a limited discussions on three problems related to the work in the thesis.

(a) Modification to the ICM model:

In the interrupted coalescence model(ICM), two unrealistic assumptions have been made: (i) it is assumed the surface tension of the droplets is isotropic so that the equilibrium shape is a spherical cap. (ii) no dynamic process has applied to the two large touched droplets whose coalescing process has presumably been interrupted. The touched area is unphysical as there exist singular points. Both of those assumptions contribute to the deviation of the simulation figures from the experimental results(Figure 3.1). Careful examination of Figure 3.1 shows that the droplet shape is not spherical, instead several well developed facets are seen even in the early stage where complete coalescence takes place. The complete coalescence time in an anisotropic model has a stronger dependence on system size than that in an isotropic model, which implies the size effect may play an important role in the interruption mechanism. The touched area of two large droplets has to be smoothened out. A rather rigorous method of doing this is to introduce the surface diffusion process as discussed in section 2.2. However it becomes impractical as the number of those droplets is large. The calculation in

Chapter Two shows that the healing process in the neck area is so speedy that only a small fraction of the total coalescence time is needed to reach the neck elimination stage. Therefore, as an approximation, the smoothening procedure may directly incorperate the neck elimination stage. The simulated figure would then be much closer to the SEM photograph.

(b) Dynamic phase in Au clusters:

A solid phase has different dynamic behavior from a liquid phase and whether a cluster is in a solid phase or in a liquid phase depends not only on the temperature but also on the cluster size. Our simulation results show that a solid cluster may exhibit distinct dynamic behaviors(Figure 4.17) at various sizes and temperatures. The physical basis for the existence of those different dynamics is not very clear. Our tentative explanation is that diffusion which occurs in large solid clusters but is absent in small solid clusters.

It has been pointed out that the strong existence of surface diffusion in solid gold clusters is due to the many body interaction which suggests a stronger coordination dependence than pairwise interaction(Ercolessi etc.,1988). An obvious choice is to test a Lennard-Jones(LJ) system and observe if the system has a similar behavior to gold clusters. Many MD calculations show that the system of LJ

interaction exhibits a solid-liquid phase transition. The surface atoms in any solid cluster have less binding energy than their bulk counterparts and therefore may also have similar dynamic behavior as observed in gold clusters. A detailed MD simulation on LJ systems will answer part of the question.

(c) Super-localization problem:

Scaling arguments reveal that due to the fractal dimensionality of the incipient infinite cluster of a percolation structure near its threshold, the diffusion on such a structure is anomalous. Both theoretical arguments and numerical simulations showed that the phonon's amplitude decays faster than exponential as stated in equation(5.71) on fractal structures. It is very desirable to perform a detailed numerical calculation of conductance of a system with fractal dimension. As pointed out in Chapter 5, the conductance near threshold is so small that a finite hopping constant(ideally zero) for an absent bond has to be used to obtain reliable calculation results. The introduction of this small number may profoundly alter the nature of its wavefunction, so one has to make the value as small as possible. The transfer matrix method described in section 5.2 provides an alternate and perhaps more efficient way to calculate conductance. Along with the calculation, two problems have to be addressed: (i) the relationship between

the scattering matrix and conductance, i.e. the extension of Landauer's formula; (ii) the conversion from the transfer matrix to the scattering matrix.

As a closing statement, I quote the words from Einstein "The nature is as complex as it needs to be, no more". Although the nature is asymmetrical and dynamic(it is often called beauty and mystery), life would be much easier if it is understood in its least complex form, which may be the ultimate goal for physicists.

APPENDIX A

```
C++++++++++++++++++++++++++++++++++++++++++++++++++++++++++++++++++++++++
C       The program is created to study properties
C       of Au-cluster via constant temperature MD
C++++++++++++++++++++++++++++++++++++++++++++++++++++++++++++++++++++++++

C ++++++++++++++++++++++++++++++++++++++++++++++++++++++++++++++++++++++
C       Subroutines 1.readin
C                   2.force
C                   3.kinet
C                   4.predic
C                   5.correc
C                   6.listn
C                   7.writin
C                   8.energy
C ++++++++++++++++++++++++++++++++++++++++++++++++++++++++++++++++++++++

      parameter (n=613)

      common/circles/ rx(800),ry(800),rz(800)
     &               ,vx(800),vy(800),vz(800)
     &               ,ax(800),ay(800),az(800)
     &               ,bx(800),by(800),bz(800)
     &               ,cx(800),cy(800),cz(800)
     &               ,fx(800),fy(800),fz(800)

      common/circles/ s,sv,sa,sb,sc,sf

      common/circles/ vexp(20000), vexq(20000)

      common/circles/ nei(90000), lpoint(800)

      integer free

      p = 10.15
      q = 4.13
      aa = 0.118438
      dt = 0.02
      ne = 1e4
      qq = 2.*q

c     open (unit=29, file='rg.out', status='new')
```

```
      open (unit=28, file='[yuxinhua.md]en.out', status='new')

      nstep = 2e5
      ivt = 1e2
c     tmp = 1.0e-3
      rcut2 = 3.0
      qh = 40.
      free = 3

      call readin ( n,dt )

      do 100 ie = 1,2*ne
      vexp(ie) = exp((1.-real(ie-0.5)/real(ne))*p)
      vexq(ie) = exp((1.-real(ie-0.5)/real(ne))*qq)
100   continue

      nfree = n*free

      do itmp = 1,6
      tmp = 5.0e-3 - (4.0e-4) * float(itmp)

      ten = 0.
      atm = 0.

      do 1000 istep = 1,nstep

      int = mod(istep-1,20)

      if ( int.eq.0) call listn ( n, rcut2)

      call predic (n, dt)

      call force ( n, dt, aa, p, q, ne)

      call kinet ( n, en_k )

      sf = (2.0  * en_k- real (nfree + 1) * tmp ) / (s*qh)

      call correc (n, dt )

      rxc = 0.0
      ryc = 0.0
      rzc = 0.0
```

```
      do 1001 i = 1,n
      rxc =rxc + rx(i)
      ryc = ryc + ry(i)
      rzc = rzc + rz(i)
1001  continue

      rxc = rxc/real(n)
      ryc = ryc/real(n)
      rzc = rzc/real(n)

      rg = 0.0
      do 1010 i = 1,n
      rg = rg + (rx(i) - rxc)**2 + (ry(i) - ryc)**2 + (rz(i)-rzc)**2
1010  continue
      rg = sqrt(rg/real(n))

      arg=arg+rg
      if (istep.le.1e5) goto 1000

      md=mod(istep,ivt)

      if (md.ne.0) goto 1000

      itime = (istep-1e5)/ivt

      call energy ( n,en,temp )

      write ( 28,* ) tmp,temp,en

      ten=ten+en
      atm=atm+temp
c     arg=arg/real(ivt)

c     write ( 29,*) itime,arg

c     arg=0.

1000  continue

      ten=ten/100.
      atm=atm/100.
      write ( 28,* ) tmp,ten,atm
```

```
      end do

      call writin ( n )

      close ( unit=28 )
c     close ( unit=29 )

      stop
      end

C +++++++++++++++++  end of main program ++++++++++++++++++++++

C++++++++++++++++++++++++++++++++++++++++++++++++++++++++++++++++++++++
C     begin subroutine readin
C++++++++++++++++++++++++++++++++++++++++++++++++++++++++++++++++++++++

      subroutine readin (n,dt)

      common/circles/ rx(800),ry(800),rz(800),
     &                vx(800),vy(800),vz(800),
     &                ax(800),ay(800),az(800),
     &                bx(800),by(800),bz(800),
     &                cx(800),cy(800),cz(800),
     &                fx(800),fy(800),fz(800)

      common/circles/ s,sv,sa,sb,sc,sf

      open ( unit=21, file='[yuxinhua.md]xyz.in', status='old' )
      open ( unit=22, file='[yuxinhua.md]vcc.in', status='old' )
      open ( unit=23, file='[yuxinhua.md]acc.in', status='old' )
      open ( unit=24, file='[yuxinhua.md]bcc.in', status='old' )
      open ( unit=25, file='[yuxinhua.md]ccc.in', status='old' )
      open ( unit=26, file='[yuxinhua.md]scc.in', status='old' )

      do 100 i=1,n
      read (21,* ) a,b,c
      rx(i)=a
      ry(i)=b
      rz(i)=c
100   continue

      do 200 i=1,n
      read (22,*) a,b,c
```

```
      vx(i)=a
      vy(i)=b
      vz(i)=c
200   continue

      do 300 i=1,n
      read (23,*) a,b,c
      ax(i)=a
      ay(i)=b
      az(i)=c
300   continue

      do 400 i=1,n
      read (24,*) a,b,c
      bx(i)=a
      by(i)=b
      bz(i)=c
400   continue

      do 500 i=1,n
      read (25,*) a,b,c
      cx(i)=a
      cy(i)=b
      cz(i)=c
500   continue

      read (26,*) s,sv,sa,sb,sc,sf

      close ( unit=21 )
      close ( unit=22 )
      close ( unit=23 )
      close ( unit=24 )
      close ( unit=25 )
      close ( unit=26 )

      return
      end

C++++++++++  end of readin ++++++++++++++++++++++++++++++++++++++

C++++++++++++  beginning of subroutine force  +++++++++++++++++++
```

```
      subroutine force ( n,dt,aa,p,q,ne )

      common/circles/ rx(800),ry(800),rz(800),
     &                vx(800),vy(800),vz(800),
     &                ax(800),ay(800),az(800),
     &                bx(800),by(800),bz(800),
     &                cx(800),cy(800),cz(800),
     &                fx(800),fy(800),fz(800)

      common/circles/ s,sv,sa,sb,sc,sf

      common/circles/ vexp(20000),vexq(20000)

      common/circles/ nei(90000),lpoint(800)

      qq=2.*q
      rc2=2.25

      do 200 i=1,n

      rxi=rx(i)
      ryi=ry(i)
      rzi=rz(i)
      fxi=0.
      fyi=0.
      fzi=0.

      nlow=lpoint(i)
      nup=lpoint(i+1)-1

      rxp=0.
      do 10 list=nlow,nup

      j=nei(list)
      rxij=rxi-rx(j)
      ryij=ryi-ry(j)
      rzij=rzi-rz(j)

      rij2=rxij*rxij+ryij*ryij+rzij*rzij

      if(rij2.gt.rc2) goto 10

      rij=sqrt(rij2)
```

```
      ie=rij*ne

      rxp=rxp+vexq(ie)
10    continue

      rxx=sqrt(rxp)

      do 190 list=nlow,nup

      sxp=0.

      j=nei(list)

      do 180 ljst=lpoint(j),lpoint(j+1)-1

      k=nei(ljst)
      rxjk=rx(j)-rx(k)
      ryjk=ry(j)-ry(k)
      rzjk=rz(j)-rz(k)

      rjk2=rxjk**2+ryjk**2+rzjk**2

      if(rjk2.gt.rc2) goto 180

      rjk=sqrt(rjk2)
      ie=ne*rjk
      sxp=sxp+vexq(ie)

180   continue

      sxx=sqrt(sxp)

      rxij=rxi-rx(nei(list))
      ryij=ryi-ry(nei(list))
      rzij=rzi-rz(nei(list))

      rij2=rxij**2+ryij**2+rzij**2

      if(rij2.gt.rc2) goto 190

      rij=sqrt(rij2)
      ie=ne*rij
```

```
      f1=aa*p*vexp(ie)
      f2=q*vexq(ie)/rxx
      f3=q*vexq(ie)/sxx

      f12=f1-0.5*(f2+f3)

      fxi=fxi+(rxij/rij)*f12
      fyi=fyi+(ryij/rij)*f12
      fzi=fzi+(rzij/rij)*f12

190   continue

      fx(i)=fxi
      fy(i)=fyi
      fz(i)=fzi

200   continue

      return
      end

C+++++++++++++++ end of subroutine force ++++++++++++++++++++++++++

C+++++++++++++++ beginning of subroutine kinet ++++++++++++++++++

      subroutine kinet (n,en_k)

      common/circles/ rx(800),ry(800),rz(800),
     &                vx(800),vy(800),vz(800),
     &                ax(800),ay(800),az(800),
     &                bx(800),by(800),bz(800),
     &                cx(800),cy(800),cz(800),
     &                fx(800),fy(800),fz(800)

      common/circles/ s,sv,sa,sb,sc,sf

      en_k=0.
      do 100 i=1,n
      en_k=en_k+vx(i)**2+vy(i)**2+vz(i)**2
100   continue

      en_k=(0.5*en_k)*(s*s)
```

```
      return
      end

C+++++++++++++++ end of subroutine kinet ++++++++++++++++++++++++++

C+++++++++++++++ beginning og predictor ++++++++++++++++++++++++++++

      subroutine predic ( n,dt )

      common/circles/ rx(800),ry(800),rz(800),
     &                vx(800),vy(800),vz(800),
     &                ax(800),ay(800),az(800),
     &                bx(800),by(800),bz(800),
     &                cx(800),cy(800),cz(800),
     &                fx(800),fy(800),fz(800)

      common/circles/ s,sv,sa,sb,sc,sf

      c1=dt
      c2=c1*dt/2.0
      c3=c2*dt/3.0
      c4=c3*dt/4.0

      do 100 i=1,n

      rx(i)=rx(i)+c1*vx(i)+c2*ax(i)+c3*bx(i)+c4*cx(i)
      ry(i)=ry(i)+c1*vy(i)+c2*ay(i)+c3*by(i)+c4*cy(i)
      rz(i)=rz(i)+c1*vz(i)+c2*az(i)+c3*bz(i)+c4*cz(i)

      vx(i)=vx(i)+c1*ax(i)+c2*bx(i)+c3*cx(i)
      vy(i)=vy(i)+c1*ay(i)+c2*by(i)+c3*cy(i)
      vz(i)=vz(i)+c1*az(i)+c2*bz(i)+c3*cz(i)

      ax(i)=ax(i)+c1*bx(i)+c2*cx(i)
      ay(i)=ay(i)+c1*by(i)+c2*cy(i)
      az(i)=az(i)+c1*bz(i)+c2*cz(i)

      bx(i)=bx(i)+c1*cx(i)
      by(i)=by(i)+c1*cy(i)
      bz(i)=bz(i)+c1*cz(i)
```

```
100     continue

        s = s+c1*sv+c2*sa+c3*sb+c4*sc
        sv=sv+c1*sa+c2*sb+c3*sc
        sa=sa+c1*sb+c2*sc
        sb=sb+c1*sc

        return
        end

C++++++++++++++++++++  end of subroutine predictor ++++++++++++++++++++


C++++++++++++++++++++  beginning of subroutine corrector ++++++++++++++

        subroutine correc (n,dt)

        common/circles/ rx(800),ry(800),rz(800),
     &                  vx(800),vy(800),vz(800),
     &                  ax(800),ay(800),az(800),
     &                  bx(800),by(800),bz(800),
     &                  cx(800),cy(800),cz(800),
     &                  fx(800),fy(800),fz(800)

        common/circles/ s,sv,sa,sb,sc,sf

        parameter ( g0=19.0/90.0, g1=3.0/4.0,g3=1.0/2.0,g4=1.0/12.0 )
        c1=dt
        c2=c1*dt/2.0
        c3=c2*dt/3.0
        c4=c3*dt/4.0

        cr=g0*c2
        cv=g1*c2/c1
        cb=g3*c2/c3
        cc=g4*c2/c4

        do 100 i=1,n

        axi=fx(i)/(s*s)-2.0*sv*vx(i)/s
        ayi=fy(i)/(s*s)-2.0*sv*vy(i)/s
        azi=fz(i)/(s*s)-2.0*sv*vz(i)/s
```

```
      corx=axi-ax(i)
      cory=ayi-ay(i)
      corz=azi-az(i)

      rx(i)=rx(i)+cr*corx
      ry(i)=ry(i)+cr*cory
      rz(i)=rz(i)+cr*corz

      vx(i)=vx(i)+cv*corx
      vy(i)=vy(i)+cv*cory
      vz(i)=vz(i)+cv*corz

      ax(i)=axi
      ay(i)=ayi
      az(i)=azi

      bx(i)=bx(i)+cb*corx
      by(i)=by(i)+cb*cory
      bz(i)=bz(i)+cb*corz

      cx(i)=cx(i)+cc*corx
      cy(i)=cy(i)+cc*cory
      cz(i)=cz(i)+cc*corz

100   continue

      cors=sf-sa
      s =s +cr*cors
      sv=sv+cv*cors
      sa=sf
      sb=sb+cb*cors
      sc=sc+cc*cors

      return
      end

C ++++++++++++   end of subroutine correc ++++++++++++++++++++++

C++++++++++++ beginning of subroutine listn ++++++++++++++++++++++

      subroutine listn (n,rcut2)
```

```
      common/circles/ rx(800),ry(800),rz(800),
     &                vx(800),vy(800),vz(800),
     &                ax(800),ay(800),az(800),
     &                bx(800),by(800),bz(800),
     &                cx(800),cy(800),cz(800),
     &                fx(800),fy(800),fz(800)

      common/circles/ s,sv,sa,sb,sc,sf

      common/circles/ vexp(20000),vexq(20000)

      common/circles/ nei(90000),lpoint(800)

      integer list

      list=0

      do 100 i=1,n
      rxi=rx(i)
      ryi=ry(i)
      rzi=rz(i)

      lpoint(i)=list+1

      do 199 j=1,n

      if(i.eq.j) goto 199

      rxij=rxi-rx(j)
      ryij=ryi-ry(j)
      rzij=rzi-rz(j)
      rij2=rxij**2+ryij**2+rzij**2

      if(rij2.le.rcut2) then

      list=list+1
      nei(list)=j
      endif

199   continue
100   continue
      lpoint(n+1)=list+1
```

```
      return
      end

C++++++++++++++++ end of subroutine listn ++++++++++++++++++++++++++++

C++++++++++++++++ beginning of subroutine writin ++++++++++++++++++++

      subroutine writin (n)

      common/circles/ rx(800),ry(800),rz(800),
     &                vx(800),vy(800),vz(800),
     &                ax(800),ay(800),az(800),
     &                bx(800),by(800),bz(800),
     &                cx(800),cy(800),cz(800),
     &                fx(800),fy(800),fz(800)

      common/circles/ s,sv,sa,sb,sc,sf

      open (unit=21,file='[yuxinhua.md]xyz.in',status='old')
      open (unit=22,file='[yuxinhua.md]vcc.in',status='old')
      open (unit=23,file='[yuxinhua.md]acc.in',status='old')
      open (unit=24,file='[yuxinhua.md]bcc.in',status='old')
      open (unit=25,file='[yuxinhua.md]ccc.in',status='old')
      open (unit=26,file='[yuxinhua.md]scc.in',status='old')

      do 100 i=1,n

      write (21,*) rx(i),ry(i),rz(i)
      write (22,*) vx(i),vy(i),vz(i)
      write (23,*) ax(i),ay(i),az(i)
      write (24,*) bx(i),by(i),bz(i)
      write (25,*) cx(i),cy(i),cz(i)

100   continue

      write (26,*) s,sv,sa,sb,sc,sf

      close (unit=21)
      close (unit=22)
      close (unit=23)
      close (unit=24)
      close (unit=25)
```

```
      close (unit=26)

      return
      end

C +++++++++++++++++ end of subroutine writin ++++++++++++++++++++++++++

C+++++++++++++++++ beginnig of subroutine energy ++++++++++++++++++++
      subroutine energy (n,en,temp)

      common/circles/ rx(800),ry(800),rz(800),
     &                vx(800),vy(800),vz(800),
     &                ax(800),ay(800),az(800),
     &                bx(800),by(800),bz(800),
     &                cx(800),cy(800),cz(800),
     &                fx(800),fy(800),fz(800)

      common/circles/ s,sv,sa,sb,sc,sf

      common/circles/ vexp(20000),vexq(20000)
      common/circles/ nei(90000),lpoint(800)

      temp = 0.0
      do 100 i = 1,n
      temp = temp + (vx(i)**2 + vy(i)**2 + vz(i)**2)
100   continue
      temp=0.5*(s*s)*temp

      p = 10.15
      q = 4.13
      aa = 0.118438
      qq  = 2.*q

      vn = 0.0
      do 200 i=1,n
      vn1=0.
      vn2=0.
      rxi=rx(i)
      ryi=ry(i)
      rzi=rz(i)
```

```
      do 190 j=1,n
      if (j.eq.i) goto 190
      rxij=rxi-rx(j)
      ryij=ryi-ry(j)
      rzij=rzi-rz(j)

      rij2=rxij**2+ryij**2+rzij**2
      rij=sqrt(rij2)

      vn1=vn1+exp(-qq*(rij-1))
      vn2=vn2+exp(-p*(rij-1))

190   continue

      vn1=sqrt(vn1)
      vn=vn+0.5*(aa*vn2-vn1)
200   continue
      en=temp+vn

      en=en/real(n)
      temp=2.*temp/real(3*n)

      return
      end
C++++++++++++++++++++ end of energy ++++++++++++++++++++++++++++
```

References:

1. Abrahams, E., Anderson, P. W., Licciardello, D. C. and Ramakrishnan, T. V., *Physical Review Letters* 42, 673 (1979).
2. Abraham, F. F., *Advances in Physics* 35, 1 (1986).
3. Ajayan, P. M. and Marks, L. D., *Physical Review Letters* 60, 585 (1988).
4. Ajayan, P. M. and Marks, L. D., *Physical Review Letters* 63, 279 (1989).
5. Andersen, H. C., *J. Chem. Phys.* 72, 2384 (1980).
6. Anderson, P. W., *Physical Review* 109, 1492 (1958).
7. Anderson, P. W., *Physical Review* 124, 41 (1961).
8. Anderson, P. W., *Physical Review B* 23, 4828 (1981).
9. Andersen, P. W., Thouless, D. J., Abrahams, E. and Fisher, D. S., *Physical Review B* 22, 3519 (1980).
10. Avron, J. E., Taylor, J. E. and Zia, R. K. P., *Journal of Statistical Physics* 33, 493 (1983).
11. Azbel, M. Y., *J. Phys. C* 13, L797 (1980).
12. Azbel, M. Y., *Physics Letters* 78A, 410 (1980).
13. Azbel, M. Y., *Physical review Letters* 67, 1787 (1991).
14. Bergmann, G., *Physics Reports* 107, 1 (1984).
15. Berry, R.S., in *Few-body systems and Multiparticle Dynamics* edited by D. Micha (1987).
16. Bonzel, H. P., Preuss, E. and Steffen, B., *Appl. Phys. A* 35, 1 (1984).
17. Bonzel, H. P., Preuss, E. and Steffen, B., *Surface Science* 145, 20 (1984).
18. Borel, J.P, *Surf. Sci.* 106 , 1 (1981)
19. Brailsford, A. D. and Gjostein, N. A., *Journal of Applied Physics* 46, 2390 (1975).
20. Briant, C. L. and Burton, J. J., *J. Chem. Phys.* 63, 2045 (1975)

21. Briscoe, B. J. and Galvin, K. P., *J. Phys. D* 23, 1265 (1990).

22. Brooks, A. and Aharony, A., *Europhys.Lett.* 4, 1355 (1987).

23. Buffat, Ph., Borel, J.P., *Phys. Rev A* 13 2287 (1976)

24. Bulgac, A. and Kusnezov, D., *Physical Review Letters* 68, 1335 (1992).

25. Buttiker, M., *Physical Review Letters* 57, 1761 (1986).

26. Car, R. and Parrinello, M., *Physical Review Letters* 22, 2471 (1985).

27. Castellani, C., Kotliar, G. and Lee, P. A., *Physical Review Letters* 59, 323 (1987).

28. Chui, S. T. and Weeks, J. D., *Physical Review B* 14, 4987 (1976).

29. Cleveland, C. L., *J. Chem. Phys.* 89, 4987 (1988).

30. Clogston, A. M., *Physical Review* 125, 439 (1962).

31. Cohen, A., Roth, Y. and Shapiro, B., *Physical Review B* 38, 12125 (1988-I).

32. Cowley, R. A., in "*Equilibrium Structure and Properties of Surfaces and Interfaces*" edited by Gonis and Stocks, Plenum, New York(1992).

33. Derrida, B., Godreche, C. and Yekutieli, I., *Europhys. Lett.* 12, 385 (1990).

34. Dubson, M. A. and Jeffers, G., *Phys. Rev. B* (in Press)(1994)

35. Dundurs, J., Marks, L. D. and Ajayan, P. M., *Philosophical Magazine A* 57, 605 (1988).

36. Duxbury, P. M., Dubson, M., Yu, X. and Jeffers, G., *Europhys. Lett.* 26, 601 (1994).

37. Economou, E. N. and Soukoulis, C. M., *Physical Review Letters* 46, 618 (1981).

38. Ercolessi, F., Andreoni, W. and Tosatti, E., *Phys. Rev. Lett.* 66, 911 (1991).

39. Ercolessi, F., Parrinello, M. and Tosatti, E., *Phil. Mag. A* 58, 213 (1988).

40. Family, F. and Meakin, P., *Phys. Rev. Lett.* 61 , 428(1988).

41. Family, F. and Meakin P., *Phys. Rev. A* 40, 3836 (1989).

42. Fisher, D. S. and Lee, P. A., *Physical Review B* 23, 6851 (1981).

43. Fisher, M.E., in *Statistical Mechanics of Membrants and Surfaces* edited by D. Nelson, T. Piran and S. Weinberg(1988)

44. Friedel, J., in *The Physics of Metals* edited by Ziman (1969).

45. Garzon, I. L. and Jellinek, J., *Z. Phys. D* 20, 235 (1991).

46. Grilli, M. and Tosatti, E., *Physical Review Letters* 62, 2889 (1989).

47. Gruber, E. E. and Mullins, W. W., *J. Phys.* 28, 875 (1967).

48. Gupta, R. P., *Phys. Rev. B* 23, 6265 (1981).

49. Harris, A. B., *Physical Review B* 29, 2519 (1984).

50. Herring, C., *Phys. Rev.*, 82 , 87 (1951).

51. Herring, C. in "*Structure and Properties of Surfaces*", edited by Gomer, R. and Smith, C.S. (University of Chicago Press, 1952).

52. Hoover, W. G., *Physical Review A* 31, 1695 (1985).

53. Iijima, S. and Ichihashi, T., *Physical Review Letters* 56, 616 (1986).

54. Jayaprakash, C., Saam, W. F. and Teitel, S., *Physical Review Letters* 50, 2017 (1983).

55. Jeffers, G., Dubson, M.A. and Duxbury, P. M., *J. Appl. Phys.* 75 5016(1994).

56. Jellinek, J., Beck, T. L. and Berry, R.S., *J. Chem. Phys.* 84, 2783(1986).

57. Jellinek, J. and Berry, R. S., *Physical Review A* 40, 2816 (1989).

58. Jellinek, J. and Garzon, I. L., *Z. Phys. D* 20, 239 (1991).

59. Jiang, Z. and Ebner, C., *Physical Review B* 40, 316 (1989).

60. Joanny, J. F. and Gennes, P. G., *J. Chem. Phys.* 81, 552 (1984).

61. Kellett, B. J. and Lange, F. F., *J. Am. Ceram. Soc.* 72, 725 (1989).

62. Kosterlitz, J. M., *J. Phys. C* 7, 1046 (1974).

63. Lambert, C. J. and Hughes, G. D., *Physical Review Letters* 66, 1074 (1991).

64. Lancon, F. and Villain, J., *Physical Review Letters* 64, 293 (1990).

65. Lancon, F. and Villain, in "*Kinetics of Ordering and Growth at Surfaces*" edited by Lagally, M.G., Plenum, New York(1990).

66. Landau, L. D. and Lifshitz, E. M., *Theory of Elasticity*, 3rd edt. (1986)

67. Landau, L. D. and Lifshitz, E. M., *Electrodynamics of Continuous Media*(1984)

68. Lange, F. F. and Kellett, B. J., *J. Am. Ceram. Soc.* 72, 735 (1989).

69. Langreth, D. C. and Abrahams, E., *Physical Review B* 24, 2978 (1981).

70. Lee, P. A. and Fisher, D. S., *Physical Review Letters* 47, 882 (1981).

71. Lee, P. A. and Ramakrishnan, T. V., *Reviews of Modern Physics* 57, 287 (1985).

72. Lee, P. A., Stone, A. D. and Fukuyama, H., *Physical Review B* 35, 1039 (1987-II).

73. Levy, Y. -E. and Souillard, B., *Europhys. Lett.* 4, 233 (1987).

74. Matsuoka, H., Hirokawa, T., Matsui, M. and Doyama, M., *Physical Review Letters* 69, 297 (1992).

75. Mazor, A., Srolovitz, D. J., Hagan, P. S. and Bukiet, B. G., *Physical Review Letters* 60, 424 (1988).

76. Meir, Y. and Wingree, N. S., *Physical Review Letters* 68, 2512 (1992).

77. Miller, K. T. and Lange, F. F., *Acta Metall* 37, 1343 (1989).

78. Mullins, W. W., *J. Appl. Phys.* 28, 333 (1957).

79. Mullins, W. W., *J. Appl. Phys.* 30, 77 (1959)

80. Nichols, F. A. and Mullins, W. W., *Journal of Applied Physics* 36, 1826 (1965).

81. Nose, S., *J. Chem. Phys.* 81, 511 (1984).

82. Nozieres, P. *J. Physique* 48, 1605 (1987).

83. Ozdemir, M. and Zangwill, A., *Physical Review B* 42, 5013 (1990-I).

84. Pandit, R., Schick, M. and Wortis, M., *Physical Review B* 26, 5112 (1982).

85. Pashley, D.W. *Adv. Phys.* 14 , 327(1965).

86. Pashley, D. W., Sowell, M. J., Jacobs, M. H. and Law, T. J., *Philos. Mag.* 10, 127 (1964).

87. Preuss, E., Freyer, N. and Bonzel, H. P., *Appl. Phys. A* 41, 137 (1986).

88. Raghavan, R. and Mattis, D. C., *Physical Review B* 23, 4791 (1981).

89. Robbins, M. O. and Joanny, J. F., *Europhys. Lett.* 3, 729 (1987).

90. Schommers, W. and von Blanckenhagen, P., "*Structure and Dynamics of Surfaces*" (1987)

91. Selke, W. and Duxbury, P. M., *Z. Phys. B* 94, 311-318 (1994).

92. Shapir, Y. and Aharony, A., *Physical Review Letters* 49, 486 (1982).

93. Shapiro, B., *Physical Review B* 34, 4394 (1986).

94. Shapiro, B., *Philosophical Magazine B* 56, 1031 (1987).

95. Soukoulis, C. M. and Grest, G. S., *Physical Review B* 44, 4685 (1991-I).

96. Spencer, M. S., *Review Article* 323, 685 (1986).

97. Srolovitz, D. J. and Safran, S. A., *J. Appl. Phys.* 60, 247 (1986).

98. Srolovitz, D. J. and Safran, S. A., *J. Appl. Phys.* 60, 255 (1986).

99. Stauffer, D. *Percolation Theory* (1985).

100. Stein, J. and Krey, U., *Z. Physik B* 34, 287 (1979).

101. Stein, J. and Krey, U., *Z. Physik B* 37, 13 (1980).

102. Stillinger, F. H. and Weber, T.A., *Phys. Rev. A* 25, 978(1982)

103. Tam, S. W. and Johnson, C. E., *J. Phys. A* 20, L471 (1987).

104. Thompson, P. A., Grest, G. S. and Robbins, M. O., *Physical Review Letters* 68, 3448 (1992).

105. Thouless, D. J., *Physical Review Letters* 39, 1167 (1977).

106. Thouless, D. J. and Kirkpatrick, S., *J. Phys. C* 14, 235 (1981).

107. Umbach, C. C., Keeffe, M. E. and Blakely, J. M., *J. Vac. Sci. Technol. A* 9, 1014 (1991).

108. Weeks, J. D., in *Ordering in Strongly Fluctuating Condensed Matter Systems*, edited by T. Riste (Plenum, New York, N. Y.) 1980.

109. Weeks, J. D., *Physical Review B* 26, 3998 (1982).

110. Wulff, G., Z. *Kristallogr. Mineral.*, 34 , 449 (1901).

111. Yoshino, S. and Okazaki, M., *Journal of The Physical Society of Japan* 43, 415 (1977).

112. Yu, X., Duxbury, P. M., Jeffers, G. and Dubson, M. A., *Phys. Rev. B* 44, 13163 (1991-I).

113. Zangwill, A., *Physics at Surfaces*, Cambridge Univ. Press (1988)